

A Thesis Submitted for the Degree of PhD at the University of Warwick

Permanent WRAP URL:

<http://wrap.warwick.ac.uk/158976>

Copyright and reuse:

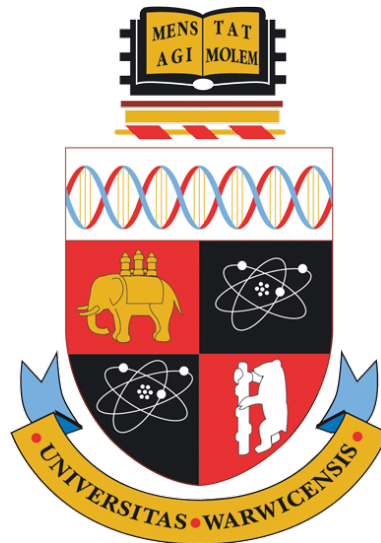
This thesis is made available online and is protected by original copyright.

Please scroll down to view the document itself.

Please refer to the repository record for this item for information to help you to cite it.

Our policy information is available from the repository home page.

For more information, please contact the WRAP Team at: wrap@warwick.ac.uk



Solid Particle Erosion Modelling using CFD techniques

by

Alok Sawant

Thesis

Submitted to the University of Warwick

in partial fulfilment of the requirements

for admission to the degree of

Doctor of Philosophy

School Of Engineering

Jan 2021

Contents

List of Tables	iv
List of Figures	vi
Acknowledgments	x
Declarations	xi
Abstract	xii
Nomenclature	xiv
Chapter 1 Introduction	1
1.1 Overview	1
1.2 Research Aim and Objectives	4
1.3 Thesis Structure	5
Chapter 2 Erosion Fundamentals and Literature Review	7
2.1 Erosion Mechanism	7
2.1.1 Erosion in Ductile Material	8
2.1.2 Erosion in Brittle Material	10
2.2 Major Factors Influencing Erosion	11
2.2.1 Particle Properties	11
2.2.2 Particle Impact Velocity	15
2.2.3 Particle Impact Angle	16
2.2.4 Target Material Properties	17
2.2.5 Fluid Flow Properties	19
2.3 Erosion Equations	21
2.3.1 Mechanistic Erosion Equations	21
2.3.2 Theoretical Erosion Equations	22
2.3.3 Empirical Erosion Equations	26
2.4 CFD based Erosion Modelling	28
2.5 Summary	29

Chapter 3 Erosion Solver	31
3.1 Multiphase flows	32
3.2 Modelling techniques for dispersed flows	33
3.2.1 Modelling dispersed flows	34
3.3 Governing equations	37
3.3.1 Carrier phase equations	37
3.3.2 Dispersed phase equations	38
3.3.3 Coupling between carrier and dispersed phase	39
3.4 Turbulent dispersed flow	41
3.4.1 Direct Numerical Simulation	43
3.4.2 Large Eddy Simulation	43
3.4.3 RANS models	44
3.5 Erosion Solver in OpenFOAM framework	47
3.5.1 Erosion Solver Outline	49
3.6 Summary	50
Chapter 4 Validation of Erosion Solver	51
4.1 Slurry Impact Test Case	51
4.1.1 Computational Domain	52
4.1.2 Mesh Independence Study	53
4.1.3 Solver Parameters	55
4.1.4 Results and Discussion	57
4.2 Air-Sand Impact Test Case	61
4.3 AISI-1018 Test Case	63
4.3.1 Computational Domain	64
4.3.2 Solver Parameters	66
4.3.3 Results and Discussion	67
4.4 Summary	74
Chapter 5 Erosion Model Development and Validation	75
5.1 Parametric Analysis of Data for Erosion Model Development . . .	77
5.1.1 Erosion rate vs impact angle vs impact velocity	78
5.2 Development of Erosion Model	83
5.2.1 Erosion at Normal Impact Angle	83
5.2.2 Impact Angle Function	90
5.3 Validation of Erosion Model	93
5.4 Summary	95
Chapter 6 Application of Developed Erosion Model and Solver	96
6.1 Parametric Study of dry impact case	97
6.2 Elbow Test Case	104
6.2.1 Geometry and Mesh	104

6.2.2	Simulation and Solver parameters	106
6.2.3	Parameters for Erosion Models	108
6.2.4	Mesh Independence Study	109
6.2.5	Effects of Turbulence Models on Erosion Rate	111
6.2.6	Particle Rebound Model	112
6.2.7	Particle Size Distribution	113
6.2.8	Particle Impact Velocity	114
6.2.9	Particle Feed Rate	119
6.2.10	Particle Size	120
6.2.11	Elbow Orientation	121
6.3	Summary	122
Chapter 7 Conclusion and Future Work		123
7.1	Summary	123
7.2	Conclusion	124
7.3	Future Work and Recommendations	127
Bibliography		129

List of Tables

2.1	Factors influencing erosion mechanism	11
2.2	Values of Constants (DNV Model) reported by Veritas [34]	27
2.3	Values of Constants (E/CRC Erosion Model) reported by Zhang et al. [17]	28
4.1	Mesh Size	53
4.2	Parameters used for CFD analysis	65
4.3	List of Erosion Model constants and parameters used for test case of AISI 1018	66
4.4	Modified constants for Oka's erosion model evaluated for AISI 1018 test case	70
5.1	Properties of the target materials used in experiments reported by Islam et al. [24]	76
5.2	Properties of the erodent particle used in experiments reported by Islam et al. [24]	76
5.3	Mean absolute percentage error between erosion rate predicted (using Oka's and new developed erosion model) and experimental data for different particle velocities.	95
5.4	Overall mean absolute percentage error between erosion rate pre- dicted (using Oka's and new developed erosion model) and experi- mental data	95
6.1	Erosion model parameters used in developed erosion model for SS316 steel (marked with ★ parameters are estimated from experi- mental data with the guideline explained in section 6.1)	100
6.2	Modified constants and exponents for Oka's erosion model evaluated form the experimental data reported by Vieira et al. [112] for SS316 target material	102
6.3	Erosion Model constants and parameters used for AISI 1018 test case	108
6.4	Maximum erosion rate predicted by the developed erosion model and CFD based erosion solver at inlet velocity of 11m/s for meshes with different cell count	110

6.5	Maximum erosion rate predicted by the developed erosion model for different particle velocities and feed rates	115
6.6	Maximum erosion rate predicted by the developed erosion model for different particle feed rates using particle of 300 μm size	119
6.7	Maximum erosion rate predicted by the developed erosion model for different particle size	120

List of Figures

1.1	Erosion damage in standard elbow [7]	2
1.2	Erosion damage in flow control part [8]	2
2.1	Erosion mechanisms [27] a) Erosion on ductile materials, b) Erosion on brittle materials	8
2.2	Erosion in ductile and brittle material vs particle impact angle [65]	17
3.1	Classification of multiphase flows [121]	32
3.2	a) Dispersed entities in control volume V_c , b) Concept of entity spacing [122]	36
3.3	Quantification of momentum coupling approach in terms of particle volume fraction and Stokes number reported by Nakhaei et al. [129]	41
3.4	Effect of particle size on turbulence intensity reported by Gore and Crowe [82]	42
3.5	Effect of Stokes number and particle volume fraction on turbulence modulation reported by Elghobashi [127]	43
3.6	Subdivision of the near-wall region [137]	45
3.7	Near-wall modelling approach [137]	46
3.8	Schematics representation showing erosion calculated at the cell face on the target surface.	48
3.9	Flow Chart of the CFD based erosion solver in OpenFOAM frame- work (One-way coupled)	50
4.1	Cut section of Computational Domain	52
4.2	Computational mesh showing grid refinement at the core and near the wall	52
4.3	Velocity contour plot at an inlet velocity of 8.15 m/s	53
4.4	Turbulence Kinetic energy contour plot at an inlet velocity of 8.15 m/s	54
4.5	Turbulence dissipation rate contour plot at an inlet velocity of 8.15 m/s	54

4.6	a) axial velocity along the centre-line of the jet, b) Axial velocity at height of 0.006 m of the jet centre-line, c) Turbulence dissipation rate along the centre-line of the jet and d) Turbulence Kinetic Energy along the centre-line of the jet	55
4.7	Rosin-Rammler fit function for the particle size data reported by Mansouri et al. [140]	57
4.8	Average particle information predicted on the target surface (35 mm diameter) at inlet velocity of 8.15m/s. a) Average particle impact velocity magnitude, b) Average impact angle of particles .	58
4.9	Average particle information predicted on the target surface at inlet velocity of 8.15m/s. a) Particle axial velocity on the target surface, b) Particle radial velocity on the target surface, experimental data reported by Mansouri et al. [140, 141]	59
4.10	Average particle impact angle predicted on the target surface at inlet velocity of 8.15m/s. a) Using Rosin-Rammler size distribution function, b) Using constant particle size (300 μ m), experimental data reported by Mansouri et al. [140, 141].	60
4.11	Average particle impact angle predicted using different turbulence models, experimental data reported by Mansouri et al. [140, 141]. .	61
4.12	Average particle information predicted on the target surface at inlet velocity of 8.15m/s. a) Average particle impact velocity magnitude, b) Average impact angle of particles	62
4.13	Average particle information predicted on the target surface at inlet velocity of 8.15m/s. a) Particle axial impact velocity magnitude, b) Particles impact angle	62
4.14	Schematic of experimental setup for dry impact test reported by Islam and Farhat [10]	64
4.15	Computational domain used for CFD analysis	64
4.16	Close View of Mesh Refinement	65
4.17	Erosion rate vs Impact Angle (AISI 1018) at particle velocity of 36m/s, a) Standard constants for erosion model, b) modified constant for Oka's angle function (n_1 & n_2), experimental data reported by Islam et al. [22]	68
4.18	Erosion rate vs Impact Angle (AISI 1018), a) at particle velocity of 36m/s, b) at particle velocity of 47m/s, c) at particle velocity of 63m/s, d) at particle velocity of 81m/s, experimental data reported by Islam et al. [22]	69
4.19	Erosion rate vs particle velocity at 90° impact angle for AISI 1018 test case, a) standard constant reported by Oka et al. [19], Oka and Yoshida [20], b) modified constants for Oka's erosion model evaluated from the experimental data reported by Islam et al. [22]	70

4.20	Predicted erosion rate vs impact angle (AISI 1018), experimental data reported by Islam et al. [22]	71
4.21	Predicted erosion rate vs impact angle (API -X70), experimental data reported by Islam et al. [24]	73
4.22	Predicted erosion rate vs impact angle (API-X100), experimental data reported by Islam et al. [23]	73
5.1	Erosion rate plotted as a function of time and velocity for API X42 target material (experimental data reported by Islam and Farhat [10])	77
5.2	Erosion Rate as a function of Impact Angle and Velocity for a) AISI 1018 steel [22] b) AISI 1080 steel [22] c) API X70 steel [24] and d) API X100 steel [23]	79
5.3	Erosion rate as function of hardness, ductility (elongation) and velocity at impact angle 30°, 45°, 60° and 90°	81
5.4	Erosion rate as function of hardness, ductility (elongation) and impact angle at 36m/s, 47m/s, 63m/s and 81m/s	82
5.5	Erosion (kg) vs Kinetic Energy (AISI 1018) using experimental data reported by Arabnejad et al. [43], Okonkwo et al. [157] and Islam and Farhat [10]	88
5.6	Erosion rate predicted by the developed erosion model at 90° impact angle for different particle velocities for AISI 1018 target material compared with experimental data reported by Arabnejad et al. [43], Okonkwo et al. [157] and Islam et al. [22]	89
5.7	Oka's Erosion Model	93
5.8	New Erosion Model	93
5.9	Oka's Erosion Model	94
5.10	New Erosion Model	94
5.11	Oka's Erosion Model	94
5.12	New Erosion Model	94
6.1	Variation of wear energy with particle velocity fitted with function 6.1 for (SS316 Steel)	97
6.2	Predicted Erosion rate vs Velocity at 90° impact angle (SS316 Steel)	98
6.3	Variation of constant b with particle velocity fitted with function 6.2 for (SS316 Steel)	99
6.4	Variation of constant n_2 with particle velocity fitted with function 6.3 for (SS316 Steel)	100
6.5	Erosion rate predicted by the proposed erosion model vs impact angle (SS316 Steel)	101

6.6	Erosion rate predicted by the other erosion models implemented in the CFD based erosion solver vs Angle (SS316 Steel) (Using constants and exponents for Oka's erosion model reported by Oka and Yoshida [20])	102
6.7	Erosion rate predicted by the other erosion models implemented in the CFD based erosion solver vs Angle (SS316 Steel) (Using modified constant and exponents for Oka's erosion model)	103
6.8	Schematic of 90°elbow geometry used for analysis [112]	105
6.9	Mesh generated for 90°elbow Geometry	105
6.10	Mesh refinement near the wall region of 90°elbow geometry	106
6.11	Maximum erosion rate predicted by the developed erosion model and the CFD based erosion solver at inlet velocity of 11m/s for different mesh sizes	110
6.12	Predicted erosion rate by the developed erosion model along the centerline on the extrados of the elbow as a function of angle (θ) while using different turbulence models at inlet velocity of 11m/s.	112
6.13	Erosion rate predicted by the CFD based erosion solver in 90° elbow at inlet velocity of 15m/s, a) using Grant and Tabakoff [160] rebound model, b) using the standard rebound model	113
6.14	Erosion rate predicted by the CFD based erosion solver in 90° elbow at inlet velocity of 15m/s, a) using constant particle size, b) using Rosin-Rammeler particle size distribution	114
6.15	Maximum erosion rate predicted by the erosion models at different inlet velocities compared with experimental data reported by Vieira et al. [112]	116
6.16	Percentage error between predicted erosion and experimental data	117
6.17	Particle information predicted by the CFD based erosion solver in 90° elbow at inlet velocity of 15m/s, a) average particle impact velocity, b) average particle impact angle	117
6.18	Erosion rate predicted vs particle impact angle, a) at particle inlet velocity of 25.22m/s, b) at particle inlet velocity of 32.56m/s	118
6.19	Erosion rate predicted by the CFD based erosion solver in 90° elbow at inlet velocity of 15m/s, a) using feed rate of 192 kg/day, b) using feed rate of 452 kg/day	119
6.20	Erosion rate predicted by the CFD based erosion solver in 90° elbow at inlet velocity of 15m/s, a) using particle size of 300 μm , b) using particle size of 150 μm	120
6.21	Erosion rate predicted by the CFD based erosion solver in 90° elbow at inlet velocity of 15m/s, a) using V-H configuration of elbow, b) using H-H configuration of elbow	122

Acknowledgments

I would like to offer my sincerest thanks to all those whose help and support have made this thesis possible. Firstly, I would like to thank my supervisor, Prof. Jennifer Wen, for her guidance and advice over the course of my PhD. Also, I extend my thanks to all the colleagues at the Warwick FIRE group, past and present, with whom I have shared discussions. My thanks go, in particular, to Dr. Vendra C. Madhav Rao and Dr. Ashish Shelke for their patience and kindness throughout my time studying.

I would like to thank all my friends for their constant support during my time of studying. Special thanks to Diwakar Singh and Harsha who were always available and willing to discuss, suggest or advise any difficulties I faced throughout my studies. I would like to thank Ruth, who has been so kind, supportive and has always cheered me up on days when the things were not going well. I would like to thank particularly, Dinesh, Rohit, Chinmay and Ananya for their patience and support throughout my time of studies. Also, I will like to acknowledge the School of Engineering, Warwick, for their belief in me and supporting me whenever I needed the most.

Lastly and most importantly, the completion of this project would not have come about if it were not for the encouragement of my parents and my brother Ashish. Thank you for your love, support and belief in me.

Declarations

This thesis is submitted to the University of Warwick in support of my application for the degree of Doctor of Philosophy. I declare that the work presented in this thesis is my own except where stated otherwise, and was carried out at the University of Warwick under the supervision of Prof. Jennifer Wen. The work has not been submitted in this or any other academic institution for admission to a higher degree.

Abstract

The wear of material due to chemical process is called corrosion and the wear of material due to the physical process is called erosion. The surface degradation of the material due to repeated solid particle impacts carried by the fluid is commonly known as solid particle erosion. Solid particle erosion can affect the mechanical integrity of the process, the transport and the storage equipment and it is faced by many industries, including the Oil and gas industry. To avoid costly breakdown and to reduce the maintenance downtime of the equipment, it is essential to predict erosion accurately. Predicting accurate erosion allows identifying erosion susceptible regions in the system. It will help engineers and designers to optimise the design parameters and better time maintenance of the equipment.

To predict solid particle erosion, many researchers have proposed different erosion models few of which are theoretically derived and few are based on experimental correlations. To calculate erosion accurately using these erosion models, there is a need for accurate particle information (such as particle velocity and particle impact angle at the target surface). Hence, these erosion models are used along with CFD to predict erosion in the complex geometries. CFD based erosion modelling consists of two main steps, modelling of solid particle and fluid two-phase flows and predicting the erosion using erosion models. In the present study, a new CFD based erosion solver is constructed using a set of open-source C++ libraries called OpenFOAM. The constructed CFD based erosion solver is validated with experimental data from the literature for its capability to predict particle information accurately on the target wall with the slurry and dry impact test cases. Six widely used theoretically and empirically derived erosion models have been implemented in the constructed CFD based erosion solver to

predict erosion. These implemented erosion models are also validated with the experimental data from the literature and analysed for various dry impact test cases using the CFD based erosion solver. It was found that these implemented erosion models predicted erosion rate reasonably for a limited range of particle velocities and impacting angles.

A new erosion model is developed based on existing erosion models and the experimental data from the literature. The developed erosion model is validated with the experimental data from the literature for various dry impact test cases. It is found that the developed erosion model and the CFD based erosion solver significantly improved the erosion predictions for a wide range of particle impacting velocities, impacting angle and for different feed rates.

Further, the capability of the developed erosion model and the CFD based erosion solver is analysed using an application test case of 90° elbow (SS316). This test case is studied using the number of different configurations to explore the advantages and limitations of the developed erosion model and solver. This work should be of interest and beneficial to investigate erosion damage in the complicated geometries among the oil and gas industries.

Nomenclature

Acronyms

<i>AISI</i>	American Iron and Steel Institute	-
<i>APIRP</i>	American Petroleum Institute Recommended Practice	-
<i>API</i>	American Petroleum Institute	-
<i>BH</i>	Brinell hardness	-
CFD	Computational Fluid Dynamics	-
DEM	Discrete Element Method	-
DNS	Direct Numerical Simulation	-
DNV	DET NORSKE VERITAS	-
E/CRC	Erosion/Corrosion Research Center	-
H-H	Horizontal-horizontal configuration	-
KE	Kinetic energy	J
LES	Large Eddy Simulation	-
RANS	Reynolds Average Navier Stokes	-
SEM	Scanning electron microscope	-
V-H	Vertical-horizontal configuration	-

Greek Symbols

α	Particle impact angle	$^{\circ}$
α_c	Volume fraction of carrier phase	-
α_d	Volume fraction of dispersed entity	-
α_g	Gas volume fraction	-
α_{max}	Impact angle at which erosion is maximum	$^{\circ}$
α_{p0}	Particle impact angle when horizontal velocity component of particle becomes zero	$^{\circ}$
β	Particle mass loading	-
τ_c	Viscous stress tensor	N/m^2
χ	Cutting wear factor	kgf/m^2
δ	Wear energy factor	J/m^3
κ	Ratio of the vertical force to the horizontal force component of the particle	-
μ_f	Dynamic viscosity of fluid	Pas
ϕ	Deformation wear factor	kgf/m^2

ϕ_s	Spherical coefficient of the particle	—
ψ	Ratio of the length of contact to the depth of cut	-
ρ	Density of fluid	kg/m^3
ρ_d	Density of dispersed entity	kg/m^3
ρ_m	Density of fluid mixture	kg/m^3
ρ_p	Density of particle	kg/m^3
ρ_t	Density of target material	kg/m^3
σ	Cauchy stress tensor	N/m^2
σ_t	Reynolds stress tensor	N/m^2
τ_c	Response time of carrier phase	s
τ_d	Response time of dispersed entity	s
τ_f	Response time of fluid	s
τ_p	Aerodynamic response time of particle	s
p	Pressure	N/m^2
Roman Symbols		
g	Gravitational force	m/s^2
U_{dir}	Particle velocity unitary vector	m/s
U	Fluid velocity	m/s
$A_{1,2,3..}$	Angle function constants	-
b	Model constant	-
C	Constant	-
$C_{1,2,3..}$	Model constants	-
D	Diameter of pipe	m
e	Coefficient of restitution	-
f	Volume fraction	-
K	Threshold velocity	m/s
L	Characteristic length	m
n, m	Exponents	-
P	Plastic flow stress	N/m^2
q	Oka's model exponent	-
Re	Reynolds number	-
Re_d	Reynolds number of dispersed entity	-
s	Oka's model constant	-
St	Stokes number	-
U_d	Velocity of dispersed entity	m/s
y	Elastic load limit	Pa
Superscripts		
\dot{W}_p	Sand flow rate	g/min
$\overline{d_p}$	Mean diameter of particle	m
d'_p	Reference diameter of the particle	m
$u'_{i,j,k}$	Fluctuating components of fluid velocity	m/s

V'_p	Reference velocity of the particle	m/s
Subscripts		
\mathbf{F}_A	Added mass force	N
\mathbf{F}_D	Drag force	N
\mathbf{F}_g	Gravitational and buoyancy force	N
\mathbf{F}_p	Pressure gradient force	N
\mathbf{F}	Force acting on dispersed entities	N
\mathcal{E}_V	Erosion volume loss of material	m^3
\mathcal{E}_{90}	Erosion rate at normal impact angle	mm^3/kg
\mathcal{E}_{Rate}	Erosion rate	kg/kg
\mathcal{E}_{VC}	Erosion volume loss of material due to cutting	m^3
\mathcal{E}_{VD}	Erosion volume loss of material due to deformation	m^3
\mathcal{E}_{VR}	Erosion volume rate	mm^3/kg
A_{pipe}	Area of pipe	m^2
C_D	Coefficient of drag	-
d_p	Diameter of particle	μm
e_n	Normal component of coefficient of restitution	-
E_p	Young's modulus of particle	N/m^2
E_t	Young's modulus of wall	N/m^2
e_t	Tangential component of coefficient of restitution	-
F_e	Specific erosion factor	-
F_S	Shape factor	-
f_{rate}	Particle feed rate	g/min
f'_{rate}	Reference particle feed rate	g/min
H_L	Liquid hold up	-
H_V	Vickers hardness	Hv
H_p	Hardness of particle	N/mm^2
H_t	Hardness of target material	N/mm^2
K_p	Oka's model constant	-
$k_{1,2,3..}$	Model constants	-
KE_{ed}	Kinetic energy used for elastic deformation	J
KE_{pd}	Kinetic energy used for plastic deformation	J
$L_{plastic}$	Plastic zone size	m^3
m_p	Mass of the particle	kg
$m_{1,2,3..}$	Model exponents	-
$n_{1,2,3..}$	Model exponents	-
q_p	Poisson's ratio of particle	-
q_t	Poisson's ratio of wall	-
S_k	Salma's model constant	-

S_m	Salma's model constant	-
V_d	Volume of dispersed entity	m^3
V_e	Erosional velocity	m/s
V_f	Fluid velocity	m/s
V_p	Velocity of particle	m/s
V_{pi}	Initial velocity of particle	m/s
V_{pr}	Rebound velocity of particle	m/s
V_{SG}	Velocity of solid-gas	m/s
V_{SL}	Velocity of solid-liquid	m/s
x_d	Position of dispersed entity	m
X_p	Position of particle	m

Chapter 1

Introduction

1.1 Overview

Petrochemical and process industries due to the nature of the complexity in their operations are subjected to high-risk factors. Among such, maintenance of the mechanical integrity of a process, transport and storage equipment is one of the critical risk factors. In the oil and gas industry, oil and gas produced especially at the offshore well are transported to the refineries or process plants through pipelines, and it often contains sand particles. Fine metal screens or gravel packs are usually used to avoid entrance of such sand particles in the pipeline [1]. Particles smaller than the screen mesh size usually enter pipelines, and some may even get stuck in the mesh of the screen. Particles stuck in the screen mesh increases fluid flow velocity in the neighbouring meshes on the screen. Due to high velocity in the screen mesh and because of erosion, mesh size gets bigger and this allows bigger particles to enter the pipeline. Therefore, the entrance of sand particles in the pipelines of the oil and gas industry is unavoidable. The entered sand particle is transported with fluid and impacts pipe wall surface, causing material degradation, and it is often known as solid particle erosion.

A considerable amount of sand is produced at the oil and gas well [2], which makes pipelines, elbows, tee junctions, valves or any measurement devices in pipelines vulnerable to erosion damage. In oil and gas production and transportation it is often noted that the components or the equipment which are exposed to a sudden change in flow direction are the most vulnerable to erosion damage. For example, sudden expansion or contraction of flow in choke valves [3, 4] or sharp bend in elbows [5] or blind tees [6] are the most vulnerable to erosion damage. When flow changes its direction at a sharp bend in elbows or blind tees, particles due to its inertia crosses the fluid streamlines and impacts wall causing solid particle erosion [7]. Erosion damage caused due to sand particles in the standard elbow and in the choke valve is as shown in figure 1.1 and 1.2 respectively.

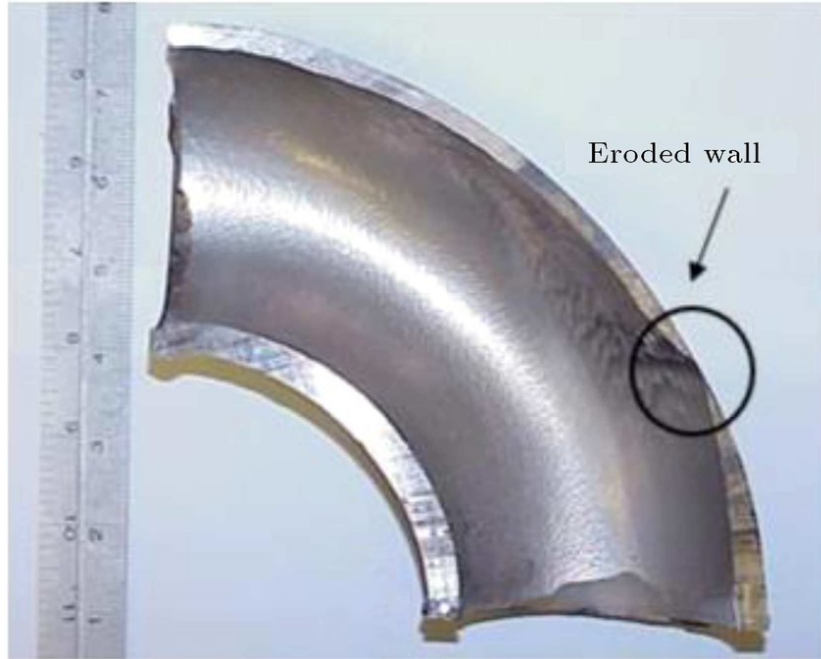


Figure 1.1: Erosion damage in standard elbow [7]



Figure 1.2: Erosion damage in flow control part [8]

Erosion due to sand particles can cause leakage in pipelines and reduces the component and equipment life and may cause the abrupt failure of the equipment. To avoid such abrupt failure, in the oil and gas industry, smart pigs are used to monitor the integrity of the pipelines [9]. Using smart pigs often increases the maintenance downtime of the pipelines, which costs economically to the oil and gas industry. Along with internal erosion, oil and gas pipelines are also vulnerable to external erosion. Especially in middle east countries, in dessert environment, oil and gas pipelines are exposed to high sand flux causing external pipeline erosion [10].

To avoid costly breakdown and to reduce maintenance downtime of the equipment, it is essential to predict erosion accurately. Predicting accurate erosion will

allow identifying erosion susceptible regions in a system. It will also avoid costly breakdown and to better time the maintenance of pipeline such as smart pig tests etc. which will avoid interrupting downtime in production. Most commonly used method to reduce erosion in the pipelines is by limiting flow velocity. Velocity below which erosion is limited is known as erosional velocity [11]. The method proposed by the American Petroleum Institute called API RP 14E API [12] for estimating erosion velocity is commonly used in industry for the last few decades[11]. Sani et al. [11] reviewed this method and its validity for estimating erosional velocity. Sani et al. [11] reported that the method recommended by API RP 14E for estimating erosional velocity is overly conservative. Companies unjustifiably loose production by using this erosional velocity for reducing erosional damage.

To ensure a safe working environment and operational conditions and to avoid problems in production, it is necessary to estimate erosion rate accurately. Predicting accurate erosion rate, erosion scar shape and erosion location will help engineers and designer to optimise the design of the equipment to reduce damage caused by erosion. To understand and predict erosion accurately, researcher and engineers have studied and investigated erosion mechanisms over the number of years and have proposed a number of erosion prediction equations. Some of these proposed erosion prediction equations are derived theoretically [13–16], and some of them are based on experimental correlations [17–20].

In complex geometries to predict erosion, these erosion prediction equations are often used along with CFD (Computational fluid dynamics) [1]. CFD based erosion modelling consists of two main steps, First, by using CFD, the solid particle and fluid two-phase flow is simulated. Further, the calculated particle information such as particle impact angle, impact velocity etc. is provided to the erosion prediction equations to calculate erosion.

In the present study, a CFD based erosion solver is constructed using a set of open-source C++ libraries called OpenFOAM. Few widely used theoretically and empirically derived erosion models have been implemented in the CFD based erosion solver to predict erosion. This includes the estimation of local erosion hot spot and thickness lost of the target wall due to the solid particle impacts. Estimation of local erosion hot spot and wall thickness lost will enable designers and engineers to optimise design parameters, and it will also allow to better time the maintenance of equipment. This work should be of interest and beneficial to analyse erosion damage in complicated geometries among the oil and gas industries.

1.2 Research Aim and Objectives

The primary aim of the research is to construct CFD based erosion solver in OpenFOAM framework to predict accurate erosion. Following is the set of objectives which needs to be fulfilled in order to achieve the aim of the study.

Review the literature of the state-of-the-art research on erosion wear, factors influencing erosion wear, erosion models and CFD based erosion modelling approach to find the literature gap and the scope of the work. Construct the CFD based erosion solver using OpenFOAM framework. Implement widely used erosion models in the CFD based erosion solver. Validate the CFD based erosion solver for its capability to predict accurate particle information near the target wall using experimental data from the literature. Validate the implemented erosion models in the CFD based erosion solver with the experimental data from the literature.

Analyse the capability and limitations of different erosion models implemented in the CFD based erosion solver. Along with erosion models, key factors influencing erosion will be analysed critically based on the parametric study.

Develop erosion model which will fulfil any gaps observed while predicting erosion using existing erosion models. A new erosion model will be developed based on experimental data from the literature and/or existing erosion models. Validate the proposed erosion model with the experimental data and analyse its behaviour compare to other erosion models implemented in the CFD based erosion solver.

Analyse the application test case using newly developed erosion model and the CFD based erosion solver. Investigate the advantages and limitations of the new proposed erosion model with various configurations of the application test case.

1.3 Thesis Structure

Chapter 1 gives a brief background and motivation for erosion modelling using computational fluid dynamics. Aim and objective, along with the scope of current work, is discussed in the latter part. Last part explains the structure of the thesis and gives an outline of each chapter in the thesis.

Chapter 2, is a literature review and starts with discussing the fundamentals of erosion, classification of erosion mechanism for different materials. Important parameters influencing erosion are discussed briefly in this section. Few widely used mathematical formulations to predict erosion proposed by the number of researchers are discussed in detail. A brief outline of CFD based erosion modelling used by the researchers in the past is given in the latter part. The chapter summarises with few key erosion influencing parameters that will be considered while developing the new erosion model and solver.

Chapter 3 explains the methodology and framework used to construct CFD based erosion solver in OpenFOAM framework. The chapter gives a brief overview of multiphase flows, classification of multiphase flows and the modelling approaches for multiphase flows. The governing equations to model dispersed two-phase flows using the Eulerian-Lagrangian approach is discussed here. Coupling between the fluid phase and the dispersed phase is discussed briefly. The turbulence modelling approach used to simulate the dispersed two-phase flow is discussed here. Last part explains the detailed framework and outline of a CFD based erosion solver.

In the first part of chapter 4, the slurry and dry impact case are simulated using the CFD based erosion solver. The CFD based erosion solver is then validated with the experimental data for its ability to track particles accurately. In the later part, in order to validate implemented erosion models in the CFd based erosion solver, dry impact test case on AISI 1018 target material is simulated. The predicted erosion rate by the implemented erosion models in the CFD based erosion solver is validated with the experimental data. Advantages and limitations of the erosion models implemented and the CFD based erosion solver are discussed critically.

In chapter 5, a new erosion model is proposed. Detailed parametric analysis of experimental data from literature is carried out to understand the influence of different material properties on erosion. Influence of particle velocity, target material properties and particle impact angle on erosion rate is analysed extensively. Based on limitations observed in erosion prediction equations in chapter 4 and parametric analysis of experimental data from the literature, the new form of erosion model is proposed. In order to validate the newly developed erosion model, dry impact test cases with different target material are simulated. The developed

erosion model and the CFD based erosion solver is validated by comparing the predicted erosion rate with the experimental data.

In chapter 6, developed erosion model and the CFD based erosion solver is analysed using an application test case (90° SS316 elbow). The first part of this chapter explains the detailed procedure to extract constants and exponents required for the developed erosion model from the experimental data. In later part, these extracted constants and exponents along with developed erosion model, are used to analyse the application test case. A number of different test cases are simulated for 90° elbow to analyse the effect of different particle sizes, feed rates, orientations, rebound models and size distribution models on the erosion rate. The erosion rate in 90° elbow is analysed for varying particle velocities, and the predicted erosion rate by the developed erosion model is validated with the experimental data and other implemented erosion models.

Chapter 7, summarises the number of conclusions observed while developing erosion model and solver. It highlights the list of objectives achieved to reach the main aim of the research. Also, the advantages and limitations of the developed erosion model and the CFD based erosion solver are discussed. Any recommendations required towards further improvement of the developed erosion model and the CFD based erosion solver in the future are discussed in the last part of the chapter.

Chapter 2

Erosion Fundamentals and Literature Review

When a solid particle strikes the surface, it scars the target surface and degrades the surface by taking material away from the surface. The process of degradation of the target surface due to solid particle impact is commonly known as solid particle erosion [21]. The shape, size, and type of scars formed due to particle impact depend on several factors such as solid particle's size, velocity, impact angle, target material properties, and the flow environment. Researchers [10, 13, 22–26] have studied these scars and the shape of scars to understand the mechanisms behind erosion. Erosion is a complex phenomenon as it involves many different mechanisms responsible for it, which may operate at the same time and can influence one another. Total erosion on the surface due to solid particles is usually a combination of different mechanisms acting at the same time [14–16]. In this chapter, to understand the underlying physics involved in erosion, a few vital erosion mechanisms proposed by researchers are discussed. A comprehensive review of a few major critical factors influencing erosion is given in this chapter. Later, few widely used erosion equations are discussed in detail along with a brief discussion on CFD based erosion modelling studies.

2.1 Erosion Mechanism

To get an insight of erosion process and to understand the underlying mechanism of erosion, researchers have studied different sizes and shapes of erosion scars, erosion rates, etc. on several materials and observed the difference in erosion mechanisms for ductile and brittle materials. In ductile materials, erosion occurs mainly because of micro-cutting, deformation and platelet formation on the target surface by the impacting particles [1]. While, in brittle materials, erosion occurs mainly due to crack formation on the target surface by the impacting particles [1].

Figure 2.1 shows schematics for erosion mechanism for ductile and brittle

material at normal and oblique particle impacting angle. Figure 2.1a illustrates erosion on ductile materials at the normal impact angle due to the deformation erosion mechanism and at the oblique impact angle due to the cutting mechanism. Similarly, Figure 2.1b shows erosion due to crack formation on the brittle surface at the normal and oblique particle impact angles. Based on these observed erosion mechanisms researchers have developed and proposed different theoretical and empirical erosion prediction equations and correlations to estimate the erosion rate of the target material.

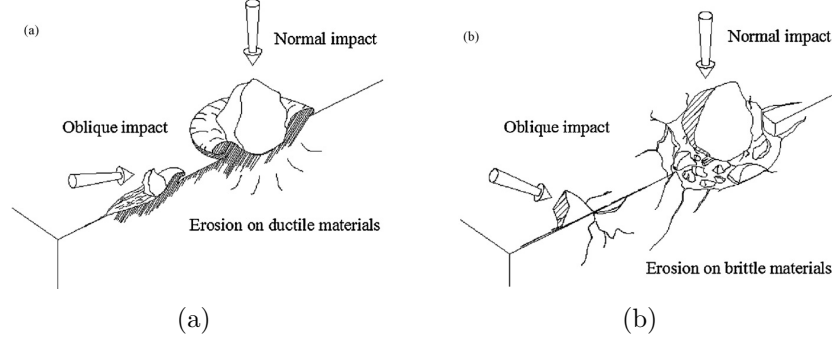


Figure 2.1: Erosion mechanisms [27] a) Erosion on ductile materials, b) Erosion on brittle materials

2.1.1 Erosion in Ductile Material

Erosion in ductile materials is studied widely by the researches on several different materials. Based on microscopic studies of eroded materials, many different erosion mechanisms happen to be responsible for erosion in ductile materials. Haller [28] was one of the earliest researchers who pointed out that erosion wear due to particle impact is different for large and small impacting angle. Later, Wellinger [29] investigated erosion in soft or ductile low carbon steel and hard or brittle high carbon steel at various particle impacting angles. He noticed that hard or brittle high carbon steel appears to be more erosive resistant at low impact angle than soft or ductile low carbon steel, and it is reverse for high impact angle. These observations of erosion in ductile materials showed that the erosion mechanism differs according to particle impact angle and the target material properties. To understand the difference in erosion in ductile materials, researchers have studied many different parameters such as solid particle properties, target material properties, the flow conditions, etc. and these properties were later used as a basis to develop erosion prediction equations.

Finnie [13] proposed one of the first famous theoretical erosion prediction equation based on micro-cutting of the target material. He suggested that as a particle hits the target surface at a low impact angle, it forms a crater on the surface by piling up material at the side of a crater and leaves the surface, piled up material is then removed by subsequent impact of the particles. For

oblique impact angles, particle penetrates in the target material by cutting the material and stays stuck on the target surface; this is also known as the cutting mechanism [30]. Finnie's proposed erosion model predicted good erosion results for low impact angle but could not predict erosion at normal impact angle, later Finnie [31] addressed this limitation. Bitter [14, 15] proposed erosion prediction equation based on the theory of cutting and deformation wear mechanisms. Bitter [14] explained about erosion at high impact angles using the deformation wear mechanism and at low impact angles by cutting wear mechanism. He emphasised that the total erosion on the target surface is usually a combination of both cutting and deformation wear mechanism.

Bellman and Levy [26] studied the mechanism of erosion in a ductile material microscopically. They proposed that the impacting solid particle creates craters and small platelets on the target surface. These platelets are later removed from the target surface by subsequent particle impacts. When these platelets are formed upon particle impact, adiabatic shear heating happens on the target surface, and work hardening occurs under the target surface area. The mechanism of platelet formation is responsible for higher erosion rate in steady-state condition than in initial condition. Tilly [32] proposed that erosion in ductile materials happens in two stages. In the first stage, impinging particles make indentation or chips of the target material. In the second stage particles break up, and fragments of particles propagate radially from the primary site, and secondary damage happens. Sundararajan and Shewmon [33] proposed analytical equation for erosion prediction based on the idea of localization. They suggested that upon particle impact, there is a strain called critical strain. The critical strain causes plastic deformation to localize and lead to lip formation, which subsequently removes material from the target surface.

By studying different sizes and shapes of scars and after microscopic analysis of eroded surface, many researchers have come up with a different theory for erosion mechanism based on which they proposed different erosion prediction models [13–15, 26]. Some of the proposed erosion models are based on experimental correlations [34, 35]. A brief discussion about such erosion prediction models is given in section 2.3. Most of the proposed erosion models are based on either of the following erosion theories:

- Deformation and Cutting

In Deformation and Cutting wear theory, particle strikes the target material at an acute angle where the vertical component of particle velocity is responsible for deformation wear and the horizontal component of particle velocity is responsible for cutting wear [14–16].

- Micro-machining

In micro-machining mechanism theory, striking particles removes material from the target material which is similar to the milling cutter [13].

- Platelet formation

In platelet formation theory, striking particles remove material from the target material due to micro-extrusion and forging [26].

Mainly four different erosion mechanisms are often found to be reported for ductile materials by many researchers based on their experimental studies. Nguyen et al. [25] in 2016 performed a wet-erosion test and also reported these four commonly observed erosion mechanism in erosion. These four commonly observed erosion mechanism are indenting, sliding, cutting and ploughing. When the particle strikes the target surface, it creates surface depression because of plastic deformation, this mechanism is known as indenting. Sliding is when impacting particles slides on the target surface and forms sliding crater. Ploughing happens when impacting particles indent deeply into the target surface and moves along the surface subsequently. Cutting usually happens at low impact angle, when impacting particle cuts the target surface as it strikes.

2.1.2 Erosion in Brittle Material

As discussed in section 2.1.1, researchers have proposed many different erosion mechanisms responsible for solid particle erosion in ductile materials. For brittle materials, the majority of researchers have agreed that the wear in brittle materials happens mainly because of crack formation [36]. As solid particle strikes brittle material, it creates lateral and radial cracks, while subsequent particle impacts grow these cracks. When these cracks intersect with each other, small pieces of the target material are removed.

2.2 Major Factors Influencing Erosion

As erosion is a complex phenomenon, numerous parameters are responsible for the erosion mechanism. Some of these critical erosion influencing factors are outlined in the table 2.1.

Table 2.1: Factors influencing erosion mechanism

Target	Flow Conditions	Particles	Fluid
Hardness	Particle Velocity	Size	Viscosity
Alloying conditions	Angle of Impact	Shape	Density
Toughness	Particle-particle Interaction	Density	Temperature
Elastic modulus	Boundary layer properties	Hardness	Lubricity
Micro-structure	Particle rebound	Toughness	-
Heat Treatment	Concentration	-	-

A brief discussion of a few of these critical influencing parameters are carried out in the next section.

2.2.1 Particle Properties

Particle properties play a significant role in erosion. Researchers have studied many different particle properties such as particle size, shape, concentration, material properties etc. and its effect on erosion. These erosion influencing particle properties are discussed briefly in this section.

Particle Size

Effect of particle size on erosion is strong and yet to be understood entirely. Nguyen et al. [25] carried detailed experimental and numerical erosion study to understand the effect of particle size on erosion and classified studies into different categories:

- Erosion Rate

Studies of the effect of particle size on erosion pointed out that an increase in particle size increases the erosion rate[32, 37]. This increase in erosion rate with particle size is because bigger particle will have larger kinetic energy, even if it travels with the same velocity as that of small particles. Tilly [32] observed an increase in erosion rate with an increase in particle size in his experimental erosion study. He noted that an increase in erosion rate with an increase in particle size

is valid up to some critical particle size and similar behaviour was also observed by Misra and Finnie [38]. Based on experimental studies Misra and Finnie [38] reported $100\text{ }\mu\text{m}$ as the critical particle size. They discussed the theory of the effect of particle size on erosion based on surface material properties. The first theory was proposed by Kramer and Demer [39] based on target surface layer's work hardening. This theory suggested that the target surface layer of up to $100\text{ }\mu\text{m}$ work-hardens more than the bulk of the material. When small particles abrade the target surface, they only influence the hard layer, and thus small particles encounter much harder material than larger particles do. Larger particles, along with hard layer deforms the surface below the hard layer and hence abrade more. Influence of the hard layer will be small after some critical particle size; hence there will be no increase in erosion rate further. The second theory was based on the dislocation of tangles near the target surface.

Nguyen et al. [25] carried experimental study to understand the effect of the particle size on the erosion rate. He used particle size ranging from $50\text{ }\mu\text{m}$ to $700\text{ }\mu\text{m}$ and confirmed that erosion rate increases with increase in particle size up to critical particle size. From his experimental work, he reported $150\text{ }\mu\text{m}$ as a critical particle size above which decay in erosion rate was observed. Abouel-Kasem [40] studied experimentally the effect of particle size on erosion rate for 5117 steel. He used six different sizes of particles in his study and reported that the transition in erosion rate is observed for particle size below $200\text{ }\mu\text{m}$. Another study performed by Desale et al. [41] noticed that there was no significant change in erosion rate with particle size when the impact angle was 90° .

- Erosion Pattern

Nguyen et al. [25] experimental studies showed that erosion pattern, i.e. erosion scars shape is influenced by particle size and flow conditions. Smaller particles can exchange their momentum with fluid quickly than that of larger particles; hence larger particles will have less deviation from the flow trajectory. Smaller particles can scatter along a larger area while approaching the target wall. Erosion profile is the shape of the scar on the target material. It is influenced by particle size, fluid flow, fluid viscosity etc. 'W' shaped erosion profile is often found on the wet-erosion test rig [7], while 'U' shaped profile is observed in dry or air erosion test rig [7]. Nguyen et al. [25] found 'W' shaped scar when the particle size was below $400\text{ }\mu\text{m}$, and 'U' shaped scar for the particle size above $400\text{ }\mu\text{m}$.

- Erosion Mechanism

Malkin et al. [42] explained particle size and their contribution towards sliding, ploughing and cutting wear mechanisms while studying abrasive and grinding wheels experimentally. They proposed that different wear mechanisms like cutting,

ploughing, chipping and sliding observed is related to different size of particles. They suggested that the small particles contribute towards ploughing of material from the target surface while larger particles contribute towards cutting of material. Later, Misra and Finnie [38], in their experimental studies, confirmed that particle size might contribute but plays a less significant role in different erosion mechanism, especially in ploughing and cutting.

Effect of particle size on erosion has been studied quantitatively by the researchers. To establish the relationship between particle size and erosion rate, some researchers have proposed a power-law relation between both [19, 20, 43]. Power-law relation between particle size and erosion rate is given as

$$\mathcal{E}_{rate} \propto (\overline{d_p})^n \quad (2.1)$$

Where $\overline{d_p}$ is mean diameter of particles and the value of exponent n usually varies between 0.3 to 2.0, depending on material properties, particle size distribution, velocity and flow conditions [25, 41, 44]. Oka's [19, 20] erosion model takes particle size into account explicitly, and he reported the value of exponent n to be around 0.19.

Particle Shape

To understand the effect of particle shape Brown et al. [45] conducted experiments on aluminium alloy at 90° impact angle with spherical and quartz shaped particles of 200 μm size. He reported that because of the sharpness in quartz particles material removed by cutting mechanism was more compared to spherical particles. Total erosion rate with the quartz particles was more than the spherical particles. Salik and Buckley [46] studied the effect of particle shape and various heat treatment on erosion in plain carbon steel. Salik and Buckley [46] used crushed glass and glass beads in erosion tests and reported that erosion rate using crushed glass (sharp, angular) was of an order of magnitude than the erosion rate obtained with glass beads. Similar results were reported by Levy and Chik [47], while they observed from experimental results that for the sharp angular particles, the magnitude of erosion was four times the magnitude of erosion for the spherical particles.

To accommodate the effect of particle size in erosion prediction equations, few researchers have introduced shape factor in their erosion prediction equations. Huang et al. [48] introduced shape factor in their phenomenological erosion prediction equation, where value for shape factor varies from 0.5 for line cutting to 1 for area cutting. Similarly Zhang et al. [17] erosion model has adopted particle shape factor in their erosion model. Oka and Yoshida [20] erosion model does not take shape factor into account explicitly, but they have attributed many of their model's constants and exponents related to the particle shape factor.

Particle Material Properties

To study the effect of particle composition on erosion rate Levy and Chik [47] performed erosion experiments on AISI 1020 carbon steel with particle velocity of 80 m/s and impact angles at 30° and 90°. Five different materials of angular particles were used. They found that erosion rate increases with a constant rate, with an increase in hardness (H_V) of particle up till $H_V < 700 \text{ kgf/mm}^2$. The particles with $H_V > 700 \text{ kgf/mm}^2$ does not necessarily increase the erosion rate. Levy and Chik [47] suggested that the softer particles upon impact shattered into small pieces with lower mass and kinetic energy, hence low erosion rate was found than the erosion rate with larger particles. When the particles were strong enough not to break up upon impact, the erosion rate became constant.

Wada and Watanabe [49] has suggested the correlation 2.2 to explain the relationship between particle hardness and the erosion rate.

$$\mathcal{E}_{rate} \propto \left(\frac{H_t}{H_p} \right)^n \quad (2.2)$$

Here H_t is the target material hardness and H_p is the hardness of the particle. Shipway and Hutchings [50] also studied the effect of particle properties on the erosion rate for many different materials with different hardness values. They observed and reported that the erosion rate increases rapidly with an increase in hardness ratio (equation 2.2) until unity. Similarly, the density of the particle plays a vital role in determining the erosion rate. Particles with higher density will possess higher kinetic energy which creates more impact force upon impact leading to higher erosion rate [44].

Particle Concentration

Particle concentration term is usually interpreted as percentage content of particle by weight or volume in fluid medium [51]. Particle concentration studies carried by Uuemöis and Kleis [51], Deng et al. [52], Andrews and Horsfield [53] and Macchini et al. [54] showed from the experimental results that increase in particle concentration in the fluid system decreases erosion rate. Mills and Mason [55] explained this decrease in erosion rate is because, due to the increase in particle concentration, the probability of inter-particle collision increases. This inter-particle collision decreases the average kinetic energy of impacting particles. Hence, increasing particle concentration in the flow system acts as a protective barrier for erosion near the target surface, and this phenomenon is called as a shielding effect [52].

Effect of particle concentration on erosion rate studied experimentally on slurry impact test case by Wang et al. [56] and Turenne et al. [57] reported a

power-law relationship between them written as,

$$\mathcal{E}_{rate} \propto \frac{C}{f^n} \quad (2.3)$$

Where C is constant, f is the volume fraction of particle and n is the exponent. Wang et al. [56] reported from their study the value of exponent n to be around 0.19.

From the numerically modelling point of view, particle concentration can be associated with particle mass loading and written as,

$$\beta = \frac{\text{particulate mass per unit volume}}{\text{fluid mass per unit volume}}$$

Lopez [58] suggested that if the value of mass loading is bigger than 0.2, two way coupling between particle and fluid is expected. If the value of mass loading is bigger than 0.6 four-way coupling is expected; hence particle-particle interaction cannot be neglected. Nguyen et al. [25] recently studied the effect of particle concentration experimentally and numerically and showed a reduction in the erosion rate with an increase in particle concentration.

2.2.2 Particle Impact Velocity

Particle impacting velocity plays a significant role in erosion modelling. Many researchers have reported from experimental studies that the erosion rate increases with an increase in particle velocity [10, 13, 19, 43]. This increase in erosion rate is because the particle with higher velocity will have higher kinetic energy which leads to higher localised force for erosion [10]. Based on experimental results, many researchers have proposed a power-law relation between particle velocity and erosion rate [13, 19, 43, 59], and it can be written as,

$$\mathcal{E}_{rate} \propto V_p^n \quad (2.4)$$

One of the earliest theoretical erosion equation proposed by Finnie [13] showed that the erosion rate is proportional to the square of particle velocity. Later, many researchers have shown that the value of n in the power-law relationship of velocity and erosion can go above 2. Laitone [59],[60] suggested from his experimental work on erosion in ductile material that the value of n can raise up to 4.

Tilly [32], from his study, suggested that bigger particle travelling at high velocity can break up into smaller particles upon impact. These smaller fragments of the particle, cause secondary damage around the primary site. He proposed a two-stage erosion prediction model based on particle velocity and particle fragmentation. Finnie [61] later explained that the theoretical value of exponent 2 could be bigger (up to 2.4 - 2.6). He explained that the reason for this increase in exponent n is due to rotations of the particle, which he did not consider in his

early model.

Many erosion models have a power-law relation between erosion rate and particle velocity; researchers, based on experimental results, have suggested different value for exponent n . [1]. Some researchers, such as Smeltzer et al. [62], Burnett et al. [63] based on their experimental studies have observed the value of the exponent n to vary between 0.3 to 4.5. Lindsley and Marder [64] studied the effect of particle velocity in erosion rate for alloys and reported that the value of velocity exponent n is independent of the target material properties and erosion mechanisms but is dependent on particle properties and erosion test conditions. In fact, Lindsley and Marder [64] have shown that the velocity exponent is not constant for the same erosion test conditions, and it changes over time due to a slight change in particle properties and/or test apparatus. Lindsley and Marder [64] even suggested measuring velocity exponent periodically in order to compare erosion results generated at different time. In recent studies Oka and Yoshida [20][19] have shown that the value of exponent n to vary between 1.4 to 2.4. However, Oka and Yoshida [20][19] mentioned that the value of n is not constants, but it depends on particle properties as well as target material properties such as hardness. Oka and Yoshida [20][19] has also reported from their studies that the velocity exponent n is independent of particle diameter.

Many researchers have divided the velocity of particle into horizontal and vertical components in their erosion models. Many suggested that horizontal particle velocity component is responsible for cutting, scratching, and ploughing erosion mechanisms while the vertical component of particle velocity dictates the indentation depth [14–16].

2.2.3 Particle Impact Angle

Particle impact angle is the angle between the direction of particle velocity and the target material. Effect of impact angle of particles on erosion rate is different in a ductile and brittle material. Figure 2.2 shows that in ductile material, maximum wear is observed for the intermediate impact angle, while in brittle material maximum erosion is observed at the normal impact angle. This difference in erosion rate is because in ductile materials, the cutting mechanism is dominant in erosion and it happens at a low angle of impact while in brittle materials erosion happens mostly because of crack formation at a normal impact angle. Many materials used in oil and gas industries exhibit both ductile and brittle materials characteristics. Hence many different versions of angle functions are proposed by a number of different researchers. Most of these proposed angle functions are derived empirically, for example, angle function proposed by Veritas [34] and Zhang et al. [17] erosion models, are given in a polynomial form. As these angle functions are derived empirically, the use of such angle function is valid for limited conditions.

Oka et al. [19] has given angle function for his model in trigonometric function form. Oka et al. [19] suggested that erosion at a particular particle impact angle is independent of particle velocity and size but is dependent on particle shape and material hardness. Later, Arabnejad et al. [43] in his experimental and numerical study showed that angle function is not independent of particle velocity.

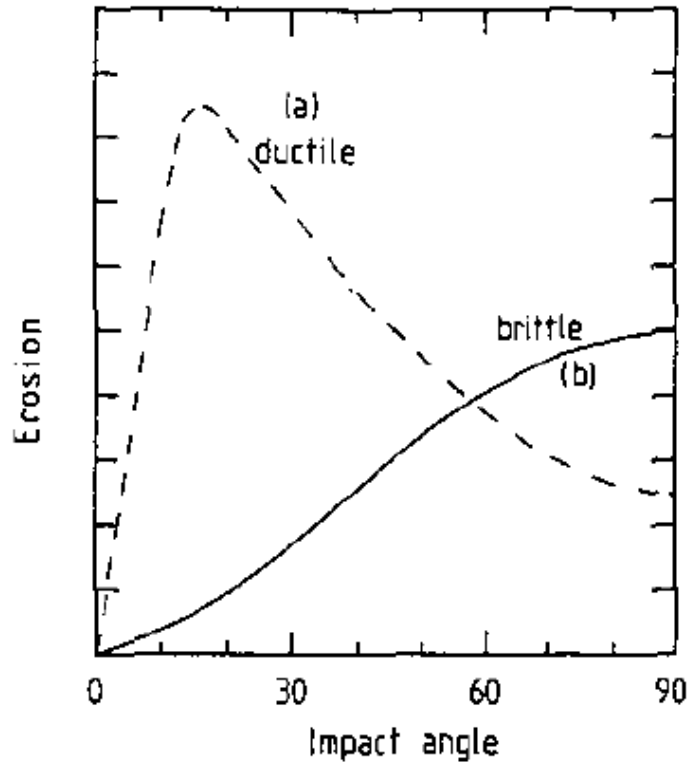


Figure 2.2: Erosion in ductile and brittle material vs particle impact angle [65]

2.2.4 Target Material Properties

Similar to impacting particles, target material properties are essential in determining the erosion rate. Researchers have studied a wide range of material properties of the target surface and its influence on erosion rate. The most common material properties studied in the literature are material toughness, hardness, thermal properties and ductility.

Finnie [31] in 1972 reported that for pure metal, the hardness of the material is inversely proportional to the erosion rate of the target material. He also observed no change in erosion rate for heat-treated carbon steel. Similarly, Sheldon and Kanhere [66] have presented a correlation between hardness and erosion rate in pure metals and copper alloys. They suggested that the hardness of a fully work-hardened surface of respective metals gives a better correlation with erosion rate. Oka et al. [67] in their studies of material properties and erosion damage showed that increase in Vickers hardness number results in a decrease in erosion indentation

size. Levy [68] studied the effect of microstructure of ductile steel on erosion. He reported that hardness of various microstructures had an inverse relation with erosion rate. Recently, Arabnejad et al. [43] studied erosion experimentally and reported that erosion rate due to cutting is inversely proportional to the annealing Vickers hardness of the target material.

Ambrosini and Bahadur [69] studied erosion in AISI 4140 steel under various heat treatment conditions. They studied the effect of various microstructure and mechanical properties of the material on the erosion rate. He reported that erosion rate increases with increasing hardness as well as with the ultimate strength of the materials while the erosion rate decreases with increasing ductility of the material. Foley and Levy [70] studied erosion in AISI 1020 plain carbon steel and AISI 4340 low alloy steel in various heat-treated conditions. They reported that ductility of the material has the most significant effect on erosion rate compared to material hardness, strength, fracture toughness. However, Levy and Hickey [71] performed erosion test on steel and found that erosion rate was lower on steel with lower hardness compared to other alloys with higher hardness. Levy and Hickey [71] reported that the hardness property of the material could reduce the ductility of material and erosion mechanism with crack formation can become dominant. Ductility of material can help to distribute particle kinetic energy on target surface by plastic deformation. Levy and Hickey [71] suggested that target material toughness can be a better indicator of erosion resistance than target material hardness. Brown and Edington [72] through SEM observations, found softening and melting of target materials. Hutchings [73], calculated the rise in temperature of the target material with plastic zone size assumptions and found unsatisfactory melting. His results indicated that due to the impact of the particle on the target surface, mechanical properties of the target surface such as material hardness might get modified. This results indicated that the work hardening might happen on the target surface. Many researchers have reported work hardening of the target material due to particle impact [20, 73, 74, 74].

Many different researchers have studied many different material properties and their effect on the erosion rate . Among such, the hardness is one of the typical target material property studied widely by the researchers [17, 19, 20, 74]. Few researchers have tried to correlate hardness with erosion resistance in their proposed erosion models [19, 20, 35, 43]. Some researchers have tried to correlate erosion resistance with material ductility [70], fatigue strength [75] and yield strength [13]. Many of these correlations showed reasonable erosion resistance for specific alloys. Few limited erosion models took work hardening into account even though work hardening of the material plays a vital role as it modifies mechanical properties of the target material[74, 76]. Oka and Yoshida [20] attempted to include work hardening in his famous erosion model but were not able to extract exponent number due to negative work hardening and nonlinear curves. Oka

and Yoshida [20] later opted to correlate load relaxation ratio to the erosion rate. As due to work hardening, the mechanical properties of the target material gets modified within the plastically deformed zone, taking work hardening into account with erosion model becomes complex. Levin et al. [77] has mentioned that the size of the plastically deformed zone might represent the amount of energy absorbed before a fracture happens during erosion. Few researchers have made attempts to measure the plastic zone size and correlate plastic zone size to crater size. However, due to other parameters not available readily in these erosion models, this makes it difficult to use these erosion models in practical application cases.

2.2.5 Fluid Flow Properties

Effect in fluid properties on particle behaviours is studied by many researchers [78–81]. Fluid flow transports solid particles to the target wall. Fluid properties may have the most significant influence on erosion rate as fluid flow properties dictate solid particles velocity, trajectory, and the impact angel, etc. [1]. Momentum transfer between the carrier phase and solid particle depends strongly on fluid properties such as density and viscosity and can be expressed in terms of Stokes number [7]. The ratio of the aerodynamics response time of particle (τ_p) to the characteristic response time of fluid (τ_f) is Stokes number [82] and written as,

$$St = \frac{\tau_p}{\tau_f} = \frac{\rho_p d_p^2 U}{18 \mu_f L} \quad (2.5)$$

Where St is Stokes number, ρ_p is the density of the particle, μ_f is the dynamic viscosity of the fluid, U is the characteristic fluid velocity, d_p is diameter of particle, and L is the characteristic length. For small Stokes number flow regime ($St \ll 1$), particle's inertial effects are small [58]. Compare to the time scale associate with the fluid flow, the time scale associated with the particle inertia is much smaller, which makes particles to respond quickly with fluid motion [83]. Hence, in low stokes number flow regime such as liquid-solid, the fluid flow has a dominant effect on particle trajectories, and particles usually follow fluid streamlines more closely. While in high stokes number regime ($St \gg 1$), particle motion is independent of fluid flow [83]. Hence, in high stokes number flow regime such as gas-solid flow, particle inertia dominates the flow [7], and it may cross the fluid streamlines.

Similar behaviour of particles was reported by Mansouri [7] in his experimental studies of sand-air and liquid-air impact test. Mansouri [7] showed from his experimental work of jet impact studies that the particles in gas-solid flow (low Stokes number) hits the target wall with same impact angle as it exits from the nozzle. While in slurry flow, particles hit the target surface with a wide range of impact angle.

Fluid flow properties such as viscosity and density can influence erosion pattern and magnitude as well. In direct impingement test fluid carries particle to the wall,

while travelling towards wall solid particle gain momentum from the surrounding fluid [1]. In straight pipe flow fluid and solid particle travels parallel to the pipe wall, here turbulent fluctuations are mainly responsible for carrying particle towards the pipe wall [83, 84].

Particle concentration can also get affected by fluid flow properties. Even though the overall particle concentration in the system is low, due to fluid flow properties, local particle concentration can become high, and it can affect erosion magnitude and pattern[1]. Fluid boundary layer can affect particle-wall interaction and hence can influence erosion rate. To accommodate effect of the liquid boundary layer on the particle velocity Clark and Burmeister [85] has proposed liquid squeeze film model.

2.3 Erosion Equations

One of the common problems faced by the process industry, the oil and gas industry is the surface degradation of materials due to solid particle impacts which causes erosion. Erosion due to solid particle impacts can increase maintenance downtime of equipment and can even lead to a costly breakdown. In oil and gas industries presence of sand in a pipeline is inevitable, and the presence of sand is the primary cause of erosion. One way to limit erosion in such equipment is to reduce the production rate, but it has got financial consequences. Hence, erosion modelling is of great importance in the industry to predict erosion accurately. Over a period of time, the number of researchers have come up with different mathematical formulations to predict erosion. Many researchers have developed erosion prediction models based on experimentally observed phenomena [17–20], some erosion models are developed empirically [86–88], and some are theoretically developed [13–16].

In this section, few widely used erosion models are discussed briefly; some of these erosion models are implemented in the CFD based erosion solver constructed in the present study and will be discussed in a later section.

2.3.1 Mechanistic Erosion Equations

To reduce erosion severity in oil and gas pipelines due to the solid particle, American Petroleum Institute Recommended Practice (API RP) suggested limiting production velocity called as erosional velocity [12]. API RP [12] in 1975 suggested that the erosional velocity can be estimated by,

$$V_e = \frac{C}{\sqrt{\rho_m}} \quad (2.6)$$

where, V_e is erosional velocity in ft/s , C is empirical constant, ρ_m is density of fluid mixture in lb/ft^3 . API [12] recommended the value for constant C as 100 for continuous service and 125 for intermediate service. Because equation 2.6 is simple, a number of researchers have investigated the applicability of the equation 2.6 and showed that the equation is too conservative and recommended different values for the constant C [88–93].

Salama et al. [88] developed erosion model for elbows based on experimental data of Rabinowicz [94] for the ductile materials as,

$$\mathcal{E}_{rate} = S_k \frac{\dot{W}_p V_f^2}{D^2} \quad (2.7)$$

where, \mathcal{E}_{rate} is erosion rate in $mm/year$, D is diameter of the pipe (inches), \dot{W}_p is sand flow rate in $bbl/month$, V_f is velocity of fluid and S_k is model constant and it depends on geometry. Salama et al. [88] suggested for short radius elbow the

value of S_k is 0.038 and for the tee joints the value of S_k is 0.019.

Bourgoyne Jr et al. [87] studied erosion rate experimentally in diverter for gas-solid, liquid-solid and mist-solid flows and proposed two erosion correlations,

$$\mathcal{E}_{rate} = F_e \frac{\rho_p}{\rho_t} \frac{\dot{W}_p}{A_{pipe}} \left(\frac{V_{SG}}{100\alpha_g} \right)^2 \quad (2.8)$$

$$\mathcal{E}_{rate} = F_e \frac{\rho_p}{\rho_t} \frac{\dot{W}_p}{A_{pipe}} \left(\frac{V_{SL}}{100H_L} \right)^2 \quad (2.9)$$

Equation 2.8 is for gas-solid or mist-solid flow and equation 2.9 for liquid-solid flow and both equations predict erosion rate (\mathcal{E}_{rate}) in terms of wall thickness loss in m/s . In equation 2.8 and 2.9 ρ_p and ρ_t are density of particle and the target surface in kg/m^3 respectively, \dot{W} is sand flow rate in m^3/s and V_{SG} and V_{SL} is superficial velocity of gas and liquid in m/s respectively. A_{pipe} is cross sectional area of pipe in m^2 and F_e is specific erosion factor which depends on geometry type, target material and flow conditions. α_g is gas volume fraction and H_L is liquid hold up. Bourgoyne Jr et al. [87] while developing erosion equations used experimental data which was for high flow rate.

Later in 1993 Svedeman et al. [95] investigated the applicability of Bourgoyne Jr et al. [87] erosion model and found that for the lower flow velocities, erosion model (equation 2.8 and 2.9) over predicted the erosion rate. Svedeman et al. [95] in their studies also postulated the value for constant S_k in Salama et al. [88] erosion model (equation 2.7) as $S_k = 0.017$ for the long radius elbow and $S_k = 6 \times 10^{-4}$ for the plugged tee joints.

In order to consider the effect of multi-phase flow, Salama [86] incorporated particle diameter and fluid mixture density in their earlier erosion model [88] and is given as,

$$\mathcal{E}_{rate} = \frac{1}{S_m} \frac{\dot{W}_p V_m^2 d_p}{D^2 \rho_m} \quad (2.10)$$

where, \mathcal{E}_{rate} is erosion rate in $mm/year$, D is diameter of pipe and \dot{W} mass flow rate in mm and kg/day respectively. S_m is constant, ρ_m is fluid mixture density in kg/m^3 , d_p is particle diameter in $microns$ and V_m is fluid mixture velocity.

2.3.2 Theoretical Erosion Equations

Finnie's Erosion Model

Finnie [13] proposed one of the earliest erosion model. He proposed erosion model based on particle motion and material properties. He classified materials in two categories, i) Ductile materials, where erosion happens because of micro-cutting mechanism and ii) Brittle materials, where erosion happens mainly because of crack formation. He made the following assumptions while proposing the erosion model.

- ratio of vertical force to horizontal force component on the target material is constant.
- length of contact of the particle on the surface is greater than the depth of cut.
- width of cutting face on the surface is constant.
- as soon as particle impacts the target surface constant plastic flow is reached.

Using theoretical analysis of erosion and considering these assumptions he proposed two equations to predict volume loss of target surface for low and high angle of impact of particles.

$$\mathcal{E}_V = \frac{m_p V_p^2}{P \psi \kappa} \left(\sin(2\alpha) - \frac{6}{\kappa} \sin^2(\alpha) \right) \text{ if } \tan \alpha \leq \frac{\kappa}{6} \quad (2.11)$$

$$\mathcal{E}_V = \frac{m_p V_p^2}{P \psi \kappa} \left(\frac{\kappa \cos^2 \alpha}{6} \right) \text{ if } \tan \alpha \geq \frac{\kappa}{6} \quad (2.12)$$

where, m_p is mass of the particle, V_p is velocity of the particle, κ is ratio of vertical force to horizontal force and ψ is ratio of the length of cut to the depth of cut. Finnie recommended value of constant κ and ψ as 2. P is plastic flow stress on the target material and α is particle impacting angle. Equation 2.11, predicts volume loss from target surface for low impact angle of the particle and equation 2.12 predicts the volume loss for high angle of impact. Finnie [96] validated proposed erosion model with the experimental test case on steel, copper and aluminium as the target material. He found that proposed erosion model predicts reasonably accurate erosion volume loss for the low angle of impact. However, it has got serious limitations while predicting erosion volume loss at normal impact angel.

Bitter's Erosion Model

Bitter [14, 15] proposed an erosion model by theoretically analysing erosion and using the concept of cutting and deformation wear mechanisms. In his first part of the study, he proposed erosion model where erosion occurs by the deformation mechanism and is based on elastic-plastic collision theory [14].

$$\mathcal{E}_{VD} = \frac{1}{2} \frac{m_p (V_p \sin \alpha - K)^2}{\phi} \quad (2.13)$$

where, K is Bitters model constant which represent threshold velocity i.e. velocity below which no erosion takes place. Bitters recommended equation 2.16 to calculate K . The deformation wear factor ϕ is defines as amount of energy required to remove unit volume of material from the target surface due to deformation wear. He compared models (equation 2.13) predicted results with experimental data

and reported that predicted results were in good agreement with the experimental data for brittle material for a various angle of impact.

In his second part of study [15] he proposed two equations for erosion due to cutting mechanism for two situations.

1. particle still having horizontal velocity after impacting the surface and leaving.
2. horizontal velocity component of particle becomes zero during the collision.

Based on these two situations, he proposed the following equations:

$$\mathcal{E}_{VC1} = \frac{2m_p C (V_p \sin \alpha - K)^2}{\sqrt{(V_p \sin \alpha)}} \left\{ V_p \cos \alpha - \frac{C (V_p \sin \alpha - K)^2}{\sqrt{(V_p \sin \alpha)}} \chi \right\} \text{ for } \alpha \leq \alpha_{p0} \quad (2.14)$$

$$\mathcal{E}_{VC2} = \frac{\frac{1}{2} m_p [V_p^2 \cos^2 \alpha - K_1 (V_p \sin \alpha - K)^{\frac{3}{2}}]}{\chi} \text{ for } \alpha > \alpha_{p0} \quad (2.15)$$

where χ is cutting wear factor defined as the energy required to remove a unit volume of material from the target surface due to cutting wear. K , K_1 and C are model constants and are calculated by following,

$$K = \frac{\pi^2}{2\sqrt{10}} y^{\frac{5}{2}} \cdot \left(\frac{1}{\rho_p} \right)^{\frac{1}{2}} \cdot \left[\frac{1 - q_p^2}{E_p} + \frac{1 - q_t^2}{E_t} \right]^2 \quad (2.16)$$

$$K_1 = 0.82 y^2 \sqrt[4]{\frac{y}{\rho_p}} \cdot \left[\frac{1 - q_p^2}{E_p} + \frac{1 - q_t^2}{E_t} \right]^2 \quad (2.17)$$

$$C = \frac{0.288}{y} \sqrt[4]{\frac{\rho_p}{y}} \quad (2.18)$$

where, ρ_p is the density of the particle, y is the elastic load limit of the target material. q_p and q_t are the Poisson's ratio of the particle and the target material similarly, E_p and E_t are the elastic modulus of the particle and the target material respectively. α_{p0} is the impacting angle at which particles horizontal velocity component becomes zero. Equation 2.14 predicts erosion volume loss when the horizontal component of particle velocity is not zero, and equation 2.15 predicts erosion volume loss when the horizontal component of particle velocity becomes zero. He proposed total erosion volume loss is cumulative of erosion caused by deformation mechanism and cutting mechanism and given as,

$$\mathcal{E}_{total} = \mathcal{E}_{VD} + \mathcal{E}_{VC1} \text{ when } \alpha \leq \alpha_{p0} \quad (2.19)$$

$$\mathcal{E}_{total} = \mathcal{E}_{VD} + \mathcal{E}_{VC2} \text{ when } \alpha > \alpha_{p0} \quad (2.20)$$

Bitter's erosion model predicts results for low impact angle as well as normal impact angle[15] (i.e. impact angle = 90°), in which Finnie [13] erosion model had a limitation.

Neilson's Erosion Model

Neilson and Gilchrist [16] proposed erosion prediction model for the small and large angle of impact of particle. Their work is based on Finnie's model[13] and Bitter's model[14, 15]. Neilson and Gilchrist [16] simplified the complexity of Bitter's final relationships into a simpler equation. They proposed that the vertical component of particle's velocity is responsible for deformation wear and the horizontal component of particle velocity is responsible for cutting wear. They also used deformation wear factor ϕ and cutting wear factors χ in their model. They proposed two equations for low and high angle of impact as follow:

$$\mathcal{E}_V = \frac{\frac{1}{2}m_p(V_p^2 \cos^2 \alpha \sin n\alpha)}{\chi} + \frac{\frac{1}{2}m_p(V_p \sin \alpha - K)^2}{\phi} \text{ for } \alpha \leq \alpha_{p0} \quad (2.21)$$

$$\mathcal{E}_V = \frac{\frac{1}{2}m_p(V_p^2 \cos^2 \alpha)}{\chi} + \frac{\frac{1}{2}m_p(V_p \sin \alpha - K)^2}{\phi} \text{ for } \alpha \geq \alpha_{p0} \quad (2.22)$$

where, K is velocity component normal to the surface below which no erosion takes place, which is sometimes also referred to as threshold velocity.

They outlined a general procedure to estimate deformation and cutting wear factor in his proposed erosion model as follow:

1. If the actual erosion-angle of impact characteristic exhibits a maximum then $\frac{\chi}{\phi} < 1$
2. Using erosion value from experiment at $\alpha = 90^\circ$, ϕ can be obtained using relation $\mathcal{E}_{90} = \frac{\frac{1}{2}m_p V_p^2}{\phi}$
3. Using ϕ , contribution of deformation wear towards total wear at all impact angles can be calculated.
4. Similarly, cutting wear can be obtained at all impact angles by subtracting deformation wear from total wear, and the angle at which cutting wear is maximum is obtained.
5. Using this angle for maximum cutting wear and equation 2.23, value for constant n and α_{max} can be determined by using $\frac{\chi}{\phi} = 0$.
6. From n and α_{max} value of χ can be obtained.

$$\frac{\chi}{\phi} = \sin n\alpha_{max} - \frac{n \cos n\alpha_{max}}{2 \tan \alpha_{max}} \quad (2.23)$$

7. If the actual erosion-angle of impact characteristic does not exhibits a maximum then $\frac{\chi}{\phi} > 1$. Then the procedure here is to follow (2), (3), (4) and (5) above and to determine the angle giving half the erosion experienced at 90° from the actual characteristic. Thus n and α can be used to obtain $\frac{\chi}{\phi}$ and χ .
8. For cases where the maximum cannot be obtained accurately, it is recommended to find the maximum possible α (greatest α for the smallest n , i.e. when $\frac{\chi}{\phi} = 0$) and to use a value greater than this to obtain χ and hence $\frac{\chi}{\phi}$.

2.3.3 Empirical Erosion Equations

Oka's Erosion Model

Oka et al. [19] proposed one of the most popular erosion model based on empirical correlation. He proposed an equation for erosion dependency on particle velocity at normal impact angle, while considering the effect of particle properties, size, shape along with target material properties.

$$\mathcal{E}_{90} = K_P(H_V)^{k_1}(V_p)^{k_2}(d_p)^{k_3} \quad (2.24)$$

where, K_p denotes particle properties such as particle shape (angularity) and particle hardness and is of arbitrary unit. H_V is material hardness, exponent k_1 and k_3 are exponent factors and k_2 is a function of material hardness and particle properties. v_p is velocity of particle and d_p is diameter of particle. They generalised proposed equation 2.24 for all impact angles by introducing angle function.

$$f(\alpha) = (\sin \alpha)^{n_1}(1 + H_V(1 - \sin \alpha))^{n_2} \quad (2.25)$$

The first term on the right-hand side of equation 2.25 is associated with repeated plastic deformation while the second term shows cutting action, which is more dominant at a low angle of impact. Here, exponents n_1 and n_2 depend on material hardness and other particle properties such as shape. Erosion at any impact angle can be calculated by using equation 2.26

$$\mathcal{E}_{VR} = f(\alpha) \cdot \mathcal{E}_{90} \quad (2.26)$$

In later studies, Oka and Yoshida [20] modified equation 2.24 to compensate effect of work hardening with new mechanical property load relaxation.

$$\mathcal{E}_{90} = K_P(aH_V)^{k_1b} \left(\frac{V_p}{V'_p} \right)^{k_2} \left(\frac{d_p}{d'_p} \right)^{k_3} \quad (2.27)$$

where, a and b are constant and exponents which are of an arbitrary unit and are

determined by particle properties. V_p' and d_p' are reference particle velocity and diameter used in the experiment.

DNV Erosion Model

Haugen et al. [18] proposed an erosion model for straight pipe, elbow, welded joints, plugged tees and reducers. This model is also known as Det Norske Veritas (DNV) erosion model, and it is constructed empirically from numerous experimental erosion test results [34].

$$\mathcal{E}_{Rate} = m_p [C V_p^n f(\alpha)] \quad (2.28)$$

$$f(\alpha) = \sum_{i=1}^8 (-1)^{(1+i)} A_i (\alpha)^i \quad (2.29)$$

where, C is material constant value of which for steel is given as 2.9×10^{-9} , n is velocity exponent and value is given as 2.6.

Function of α is as given in equation 2.29, where A_i are the model constants and values of which are given in Table 2.2.

Table 2.2: Values of Constants (DNV Model) reported by Veritas [34]

A1	A2	A3	A4	A5	A6	A7	A8
9.37	42.30	110.86	175.80	170.14	98.40	31.21	4.17

E/CRC Erosion Model

Erosion and Corrosion research centre (E/CRC) from the University of Tulsa proposed many erosion models based on series of erosion experiments. Zhang et al. [17] proposed one widely used form of E/CRC erosion model.

$$\mathcal{E}_{Rate} = m_p [C (BH)^{-0.59} F_S V_p^n f(\alpha)] \quad (2.30)$$

$$f(\alpha) = \sum_{i=1}^5 A_i \alpha^i \quad (2.31)$$

where, $C = 2.17 \times 10^{-7}$, $n = 2.41$ is empirical constants, α is particle impact angle in radians. F_S is particle shape coefficient where $F_S = 1$ for sharp, angular particles, $F_S = 0.53$ for semi rounded and $F_S = 0.2$ for rounded particles. BH is Brinell hardness for the wall material. Angle function for Zhang et al. [17] (E/CRC) erosion model is given by equation 2.31 where, α is particle impact angle in radians and A_i is model constants and value of which are given in table 2.3.

Table 2.3: Values of Constants (E/CRC Erosion Model) reported by Zhang et al. [17]

A1	A2	A3	A4	A5
5.40	-10.11	10.93	-6.33	1.42

2.4 CFD based Erosion Modelling

As discussed in the previous section, many different factors such as particle properties, material properties, particle size, shape, velocity, impact angle, flow conditions, fluid properties and geometry play vital role influencing erosion. Many of these erosion influencing factors interact with each other, and hence it makes the study of erosion with experiments more complex. Moreover, some of the mechanistic erosion equations, as discussed earlier, are easy to use but are valid for limited flow conditions or for simple geometries. Theoretically or empirically derived erosion equations can be used for the complex geometries, but as discussed earlier, it needs accurate particle velocity and impact angle as erosion models input. CFD is a powerful tool which can track particle information in detail to predict accurate particle velocity and impact angle even in complex geometries. These theoretically and empirically derived erosion equations can be implemented in CFD to predict erosion accurately. CFD not only enables us to study the effect of different properties on erosion, but it helps to predict maximum erosion rate, identify areas more susceptible to erosion in complex geometries.

Benchaita et al. [97] in 1983 performed one of the earliest erosion study using CFD on jet impingement geometry. They solved potential flow for the fluid phase on simple two-dimensional geometry and used Newton's equation of motion to track particles. They neglected a few of a factors such as the effect of turbulence and boundary layer in their studies. Their numerical results showed reasonable accuracy in locating erosion position and distribution, but erosion rate was over predicted. While analysing the effect of erosion in the choke valve using CFD McLaury [98] studied the effect of turbulence on erosion rate. Many researchers have studied erosion using CFD for pipe elbows [17, 99–101], choke valve[3, 4], sudden contraction or expansion [102–105] and many more complex geometries[106–109]. Nguyen et al. [25] have studied erosion using the coupling of CFD and DEM (Discrete Element Method) code to study the effect of particle-particle interaction on erosion rate in jet impingement geometry. They showed good agreement between the predicted erosion rate with experimental data. Solnordal et al. [110] conducted experimental and CFD based study of erosion in elbow geometry. While studying erosion in elbow using CFD, Solnordal et al. [110] showed that incorporating wall roughness effect in CFD improved erosion prediction results.

Zamani et al. [111] investigated the erosion of an elbow pipe due to the gas-solids turbulent pipe flow using CFD for different particle velocities using particle size of 300 μm . They analysed a few of widely used (DNV [34], E/CRC [17] and Oka's[19, 20]) erosion models in their study. They reported that the DNV erosion models underpredicted the relative erosion rate while other models overpredicted the relative erosion rate. Similarly Vieira et al. [112] and Peng and Cao [113] analysed erosion in 90° elbow using CFD for different particle velocities with particle size of 300 μm . Vieira et al. [112] reported from his CFD analysis that erosion rate was overpredicted up to an order of magnitude in their analysis. While Peng and Cao [113] reported overprediction of erosion rate for small particles using Oka et al. [19][20] erosion model and underprediction of erosion rate using other erosion models (DNV[34], E/CRC[17], Neilson[16]). Chen et al. [6] investigated the relative erosion severity between plugged tees and elbows experimentally and using CFD. They used different particle velocities and particle size in their study and reported overprediction of erosion rate using CFD for the small particle size (up to 150 μm). Wallace et al. [114] studied erosion in simple geometry with a similar configuration as the real choke valve. They also studied the complex geometry of a real choke valve. They reported underprediction of erosion rate up to 60% in simple geometry case and by a factor of 10 to 15 in complicated choke valve case.

It is interesting to note that many researchers using CFD, have reported overprediction and/or underprediction of erosion rate using different erosion models in different test cases. While analysing different test cases, a lack of consistency is observed in the prediction of erosion rate by the widely used erosion models. As outlined by Parsi et al. [1], CFD based erosion modelling consists of two main steps, modelling of solid particle and fluid (two-phase) flows and predicting the erosion using erosion models. Both of these steps are invariably important and any non-physical result in any of these steps will affect final erosion prediction.

2.5 Summary

In this chapter fundamentals of erosion and number of different mechanisms involved in erosion is discussed. Also, a comprehensive review of several factors such as particle properties, target material properties, particle size, shape, velocity, impacting angle, flow conditions and fluid properties and its influence on erosion is presented. Many different mathematical formulations proposed by a number of researchers to calculate erosion using particle and material properties along with flow conditions, is discussed. CFD based erosion modelling by many different researchers on various geometries and flow conditions is discussed. However, past studies showed that many different parameters play a significant role in influencing

erosion. In past studies of CFD based erosion modelling, many different researchers have used different erosion models to calculate erosion, as each erosion model has got its own advantages and limitations. In present studies, few of the widely used erosion models will be investigated for common test cases. While investigating erosion models, attention will be given to few key erosion influencing factors such as particle velocity, particle impact angle, material properties etc. The development of erosion solver and erosion model will be discussed in later chapters.

Chapter 3

Erosion Solver

Researchers have proposed many different mathematical formulations to predict erosion. Mechanistic erosion models are simple to use but are only limited to use in simple geometries. To predict erosion in complex geometries and flow conditions, theoretical and empirically derived erosion equations can be used along with computational fluid dynamics (CFD). For accurate prediction of erosion, it is imperative to provide various parameters pertinent to particle behaviour such as particle velocity, angle of impact, forces acting on the particle, material and particle properties etc. [1]. CFD is a powerful tool which can be used to simulate fluid flow and track particle's behaviour and trajectories in complex geometries [25, 115]. Along with the prediction of erosion rate and volume loss, CFD modelling also enables to identify the location with high susceptibility of erosion on the surface of the domain [110, 116]. CFD allows analysing fluid velocity, path, particle velocity, trajectories, erosion rate, and the concentration of particles etc. which helps to identify the critical area within systems for design optimisation [117]. CFD based erosion modelling consists of two main steps, modelling of solid particle and fluid (two-phase) flows and predicting the erosion using erosion models. Both of these steps are invariably important and any non-physical result in any of these steps will affect final erosion prediction [1].

OpenFOAM is a set of open-source C++ libraries capable of solving complex fluid mechanics problems [118]. OpenFOAM is distributed completely free and is based on object-oriented programming in C++ [119]. This reusability feature makes it popular among researchers and engineers to develop new solvers catering to their needs [118]. In the current study, OpenFOAM is used to build erosion solver due to its availability, flexibility and documentation. OpenFOAM provides several built-in libraries such as particle wall interaction, rebound models, drag models, RANS turbulence models etc. ready to use which can be integrated with the solver according to the needs [119].

The following sections of this chapter, a brief overview of multiphase flows, classification of multiphase flows and the modelling approaches for multiphase

flows is given. The governing equations to model dispersed two-phase flows using the Eulerian-Lagrangian approach is discussed here. Coupling between the fluid phase and the dispersed phase is discussed briefly. The turbulence modelling approach for simulating dispersed two-phase flow is discussed briefly. The last part explains the detailed framework and outline of the constructed CFD based erosion solver.

3.1 Multiphase flows

Multiphase flow term in context to this thesis is referred to the simultaneous flow of material with more than one thermodynamic phases. Applications of the multiphase flow can be observed in the diverse industrial branches such as fluidised bed, boiler, cyclone, cooling system, mixer vessels etc. Numerical simulation of such multiphase flows allows understanding the fundamentals of process parameters from macro scale to the nanoscale. Multiphase flows are usually classified on the bases of the structure of the interface between the phases. Based on the interface between phases Ishii [120] classified multiphase flows in three main categories.

- Separated flows
- Dispersed flows
- Transient flows

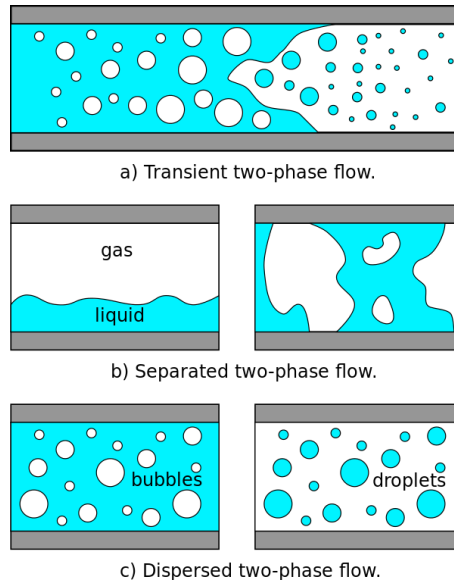


Figure 3.1: Classification of multiphase flows [121]

As shown in figure 3.1, in separated flows, phases are separated from each other with the clear interface between fluids (annular flows, film flows etc.) However, in

dispersed flow, the secondary phase is scattered in small volumes into continuous primary phase (liquid bubbles, solid particles, droplets etc). Transient flows lie in between separated flows and dispersed flows (condensation, evaporation etc).

The scope of present work for erosion modelling is concerned with the numerical simulation of dispersed two-phase flows. Thus, the continuous primary phase here is referred to as the carrier phase for the dispersed solid particles which forms the secondary phase. In liquid-solid flows, the liquid is the carrier medium, while in gas-solid flows, the carrier medium is gaseous. In liquid-solid flows, carrier phase liquid can be ideally regarded as of incompressible nature but in gas-solid flows, carrier phase gas can be of compressible nature. In the scope of present work, incompressible gas-solid flows is considered.

3.2 Modelling techniques for dispersed flows

The direct approach for numerical simulation of such two-phase flows is to solve conservation of mass, momentum and energy together along with the equations of phase and interface in between carrier and the dispersed phase. The advantage of this approach is that it offers fully resolved simulation of any dispersed two-phase flows. The challenge here using such approach is associated with the resolution of the interfaces. The numerical methods used to deal with such problems are computationally expensive and hence are limited to be used with flows where a small number of dispersed entities are involved [122]. In an industrial application which involves solid particle erosion, the above-mentioned method is not applicable. Two most widely used approaches in CFD while dealing with such problems are

- The Eulerian-Eulerian approach
- The Eulerian-Lagrangian approach

In the Eulerian-Eulerian approach, both phases are treated as continuous, non-mixing, interpenetrating phases. The idea behind this approach is to set up transport law in each computational control volume based on the volume fraction of two phases. In a computational domain, each of the two phases occupies certain space volume. Since both of the phases are treated as continuous phase both phases have to fulfil conservation of mass, momentum and energy in each control volume. Hence, they are weighted by the fraction of volume they occupy in the control volume. The sum of volume fractions is one in every control volume is used as a closure relation. In the Eulerian-Lagrangian approach, the carrier phase is treated as the continuous phase while the dispersed phase is approximated as a mass point and tracked individually by solving Newton's equation of motion for each dispersed entities. Both of the approaches are applicable to mesoscale modelling of dispersed flows. Both the approaches provide reliable and often identical results

[123]. The choice of approach to be used often depends on the specifics of the physical problem. For the denser mixture, often Eulerian-Eulerian approach is used while, for the dilute dispersed flows, Eulerian-Lagrangian approach is preferred. Although, Eulerian approach for particle tracking is computationally less expensive, predicting particle's behaviour using this approach near to the wall can be problematic. Particle's motion near the wall consists of impacting and rebounding, whereas the Eulerian approach gives only mean value of particle motions in the control volume [1]. This may cause inaccuracy in predicting particle impacting velocity near the wall, which will lead to inaccurate erosion prediction [124]. In the scope of the current work, for modelling solid particle erosion, Eulerian-Lagrangian approach is used and the approach is discussed in detail in later sections.

3.2.1 Modelling dispersed flows

In the scope of current work, the Eulerian-Lagrangian approach is selected. The carrier phase is treated as a continuous phase while the dispersed particles are tracked individually by solving Newton's equation of motion. Since the dispersed phase (i.e. solid particles) is modelled as a point mass, the interfaces between the phases are not resolved here and the solid particles are represented by their velocity and position. The mass, volume, size and shape of the solid particles are considered here in terms of the simulation parameters. In terms of the material boundaries, the carrier phase is not affected by the presence of the solid particle. This allows using simple models to include adequate closure relation to the governing equations for the carrier phase in order to introduce the presence of the secondary phase and coupling between both phases.

The Eulerian-Lagrangian approach has the limitations regarding the size of the dispersed entity and the volume loading of the dispersed entity in the dispersed flow. This approach is suitable if the dispersed entity in the dispersed flow is of moderate extent. If the size of the dispersed entity i.e. solid particle is too large, then the scale of the fluid flow around the entity becomes significant, and the mass point approximation does not hold any more [125]. Also, if the volume loading in the dispersed phase is too high then the flow becomes dense reducing spacing between the dispersed entities. Reduced space between dispersed entities makes it difficult to accurately predict the trajectories of the entities as the entities are now collision driven and further modelling effort has to be made to address this [122]. In the scope of current work relatively smaller size (micrometre) dispersed entities (solid particles) are considered with volume loading of less than 1%. The Eulerian-Lagrangian approach is suitable for such a small size and volume loading of the dispersed entities.

In the Eulerian-Lagrangian approach, the use of point mass approximation

prevents dispersed entities to have any specific shape. The most simple approach to model the dynamics of such dispersed entities is to regard entities as spherical shape. This represents the size of the dispersed entity by the diameter of the sphere and relatively simple formulae to the model carrier flow around the dispersed entity can be applied. The size of the dispersed entities (solid particle) with respect to the computation grid used for the carrier phase simulation is of vital importance in the Eulerian-Lagrangian approach. The flow around the dispersed entities cannot be simulated accurately if the diameter of the dispersed entity (solid particle) is of same length scale as the grid cell used for simulating carrier phase. Hence, to ensure accurate numerical prediction the diameter of the dispersed entities are of order smaller than the computational grid cell [126].

In the current work, the dispersed entities are modelled as mass points with assuming spherical shape, the volume of the dispersed entity (solid particle) V_d is given as,

$$V_d = \frac{\pi d^3}{6} \quad (3.1)$$

The dispersed two-phase flows can be further classified as dilute and dense flow. In the dilute flow, the fluid forces acting on the dispersed entity is the main driving force. However, in the dense flow, collisions between the dispersed entities play a vital role. The dispersed phase volume fraction ($\alpha_{dispersed}$) and the spacing between the dispersed entities L/d are the two main quantities that classify the flow pattern in the dispersed flows. For n number of spherical dispersed entities with diameter d in a control volume V_c , the volume fraction α_d is given as

$$\alpha_d = \frac{nV_d}{V_c} = \frac{n\pi d^3}{6V_c} \quad (3.2)$$

The characteristic spacing between two dispersed entities is given as

$$\frac{L}{d} = \left(\frac{\pi}{6\alpha_d} \right)^{\frac{1}{3}} \quad (3.3)$$

where L is the distance between the centre point of two dispersed entities and d is the diameter of the dispersed entity as shown in figure 3.2. The maximum volume fraction for the spherical dispersed entity (i.e. $L/d = 1$) in a cubic lattice arrangement is given as

$$\alpha_{d_{max}} = \frac{\pi}{6} \quad (3.4)$$

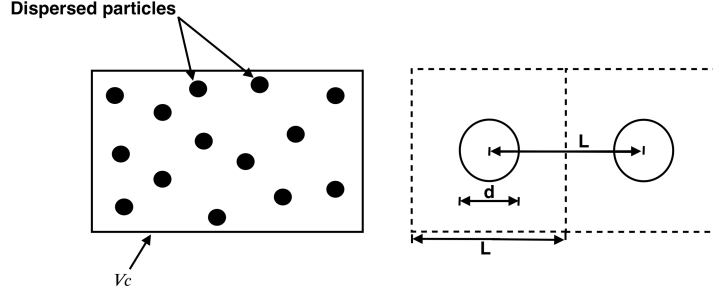


Figure 3.2: a) Dispersed entities in control volume V_c , b) Concept of entity spacing [122]

The response time scale of the dispersed entity to the momentum fluctuation of the carrier phase is one of the crucial parameters. The response time τ_d of the spherical dispersed entity in a flow is derived from the drag force acting on the entity and is given as

$$\tau_d = \frac{4\rho_d d^2}{3\mu Re_d C_D} \quad (3.5)$$

where μ is the dynamic viscosity of the carrier phase, d is the diameter of the dispersed entity, ρ_d is the density of the dispersed entity, C_D is the coefficient of the drag and $Re_{dispersed}$ is the Reynolds number of the entity.

When the response time of the dispersed entity τ_d is normalised with the response time of the carrier phase τ_c the resultant non-dimensional number is called Stokes number and is given as

$$St = \frac{\tau_d}{\tau_c} = \frac{\rho_d d_p^2 V_c}{18\mu L_s} \quad (3.6)$$

where V_c and L_c is the characteristic velocity and length scale of the flow.

Stokes number (St) and particle mass loading (β) are important parameters which help to choose the correct approach in constructing particles equation of motion. Stokes number (St) defines the degree at which particles are tied to the fluid flow [58]. Lopez [58] mentioned that flow will be dominated by particle wall interaction when $St > 2.0$ and effect of particle wall interaction will be negligible for $St < 0.25$. Particle and fluid are tightly coupled for $St < 0.05$. For $St \ll 0.01$ particle are so strongly coupled with a fluid such that particle responds instantaneously with the change in fluid flow.

3.3 Governing equations

The physical representation of the carrier phase and the dispersed phase in the Eulerian-Lagrangian approach is different. Here the carrier phase is treated as the continuum and hence can be represented by the single-phase flow equations which can be discretised in space using a computational grid. However, for the dispersed phase due to mass point approximation, it is necessary to formulate the equation of motion for each dispersed entity in the two-phase dispersed flow. As such, initially, the governing equations for both the phases are completely decoupled from each other and later suitable approach for the coupling of mass, momentum and energy exchange between phases is formulated.

3.3.1 Carrier phase equations

The continuum carrier phase can be described by the Navier-Stokes equation, which essentially expresses the conservation equations for mass, momentum and energy. In the scope of current work, incompressible and isothermal flow is considered. Hence, the density of the carrier phase is constant and the energy conservation equation is not considered here. As such, the governing equation for the continuous carrier phase is given by the incompressible Navier-Stokes equation, which essentially governs the velocity and the pressure of the carrier phase.

In the two-phase dispersed flow mixture, a significant amount of volume fraction of dispersed phase α_d may be present. The presence of significant dispersed phase (i.e. solid particles) in the flow may violate the conservation laws of the mass and momentum in the fluid volume of the carrier phase. To address this, the weighted Navier-Stokes equation for the carrier phase is considered. The Navier-Stokes equation is weighted by the volume fraction of the carrier phase α_c given as

$$\alpha_c = (1 - \alpha_d) \quad (3.7)$$

The weighted Navier-Stokes equation for the carrier phase consisting of a non-negligible amount of dispersed entities (solid particles) is written as

- Continuity Equation

$$\frac{\partial \alpha_c}{\partial t} + \nabla \cdot \alpha_c \mathbf{U} = 0 \quad (3.8)$$

- Momentum Equation

$$\frac{\rho_c \partial(\alpha_c \mathbf{U})}{\partial t} + \rho_c \nabla \cdot \alpha_c (\mathbf{U} \otimes \mathbf{U}) + \alpha_c \nabla p + \nabla \cdot \alpha_c \boldsymbol{\tau}_c = \mathbf{S} \quad (3.9)$$

In case of very dilute flow, i.e. low volume fraction of the dispersed phase ($\alpha_d \rightarrow 0$) in the dispersed flow, the effect of the secondary phase can be neglected.

Neglecting secondary phase reduces equation 3.8 and 3.9 to incompressible Navier-Stokes equation for the single-phase flow and is given as

- Continuity Equation

$$\nabla \cdot \mathbf{U} = 0 \quad (3.10)$$

- Momentum Equation

$$\frac{\rho_c \partial(\mathbf{U})}{\partial t} + \rho_c \nabla \cdot (\mathbf{U} \otimes \mathbf{U}) + \nabla p + \nabla \cdot \boldsymbol{\tau}_c = \mathbf{S} \quad (3.11)$$

where \mathbf{U} is the velocity of carrier phase in m/s , ρ_c is the density of the carrier phase in kg/m^3 , $\boldsymbol{\tau}_c$ is the viscous stress tensor of the carrier phase and in the present study is modelled assuming Newtonian behaviour of the fluid. In the scope of the current work, it is assumed that no mass transfer happens between the carrier phase and the dispersed phase (solid particles) hence the right-hand side of the equation 3.8 and 3.10 is zero. In the momentum equation, 3.9 and 3.11 the first term in the left-hand side is the substantial derivative, the second term represents the convective transport term, the third term is the pressure gradient term, the fourth term represents the diffusive transport term and the right-hand side of equations shows the source term. The source term \mathbf{S} represents the momentum transfer between the carrier phase and the dispersed phase. The details of the coupling between the carrier phase and the dispersed phase are discussed in the later section of this chapter.

3.3.2 Dispersed phase equations

In the Eulerian-Lagrangian approach, the dispersed phase (solid particles) are modelled individually by solving Newton's equation of motion. The ordinary differential equation for the velocity of the dispersed entity \mathbf{U}_d is given as

$$m_d \frac{d\mathbf{U}_d}{dt} = \mathbf{F}_d \quad (3.12)$$

where m_d is the mass of the dispersed phase and substantial derivative term of velocity \mathbf{U}_d is the acceleration of the dispersed entity. The left-hand side of the equation 3.12 is balanced by the sum of surface and volume forces acting on the dispersed entity. The velocity of the dispersed entity \mathbf{U}_d is linked to the position of the dispersed entity x_d by the second ordinary differential equation and is given as

$$\frac{dx_d}{dt} = \mathbf{U}_d \quad (3.13)$$

Thus, the solution of ordinary differential equations 3.12 and 3.13 gives the trajectories of the dispersed entities. These equations are also known as the

Lagrangian equation of motion. The forces acting on the dispersed entities F_d in a viscous fluid is given as

$$\mathbf{F}_d = \mathbf{F}_D + \mathbf{F}_p + \mathbf{F}_g + \mathbf{F}_A \quad (3.14)$$

where \mathbf{F}_D is drag force acting on the particle, \mathbf{F}_p is pressure gradient force, \mathbf{F}_g is gravity and buoyancy force, and \mathbf{F}_A is added mass force acting on the particle.

For the spherical dispersed entity the drag force is calculated as

$$\mathbf{F}_D = m_d \frac{18\mu}{\rho_d d_d^2} \frac{C_D Re(Re)}{24} (\mathbf{U} - \mathbf{U}_d) \quad (3.15)$$

where m_d , d_d , ρ_d and \mathbf{U}_d is the mass, diameter, density and velocity of the dispersed entity respectively, μ , \mathbf{U} is the dynamic viscosity and velocity of the carrier phase respectively. Re is the Reynolds number and C_D is the coefficient of drag and is obtained for a spherical particle from the following correlations

$$C_D = \begin{cases} \frac{24}{Re_d} & \text{if } Re_d < 1 \\ \frac{24}{Re_d} (1 + 0.15 Re_d^{0.687}) & \text{if } 1 \leq Re_d \leq 1000 \\ 0.44 & \text{if } Re_d > 1000 \end{cases} \quad (3.16)$$

The gravity and the buoyancy force acting on the dispersed entity is calculated as

$$\mathbf{F}_g = m_d \mathbf{g} \left(1 + \frac{\rho}{\rho_d}\right) \quad (3.17)$$

The pressure gradient force acting on the dispersed entity is calculated as

$$\mathbf{F}_p = \frac{1}{6} \pi d_d^3 \nabla p \quad (3.18)$$

The added mass force acting on the dispersed entity is calculated as

$$\mathbf{F}_A = \frac{1}{12} \pi d_d^3 \rho_d \frac{d\mathbf{U}_d}{dt} \quad (3.19)$$

In the simulations carried in the present work, the particle diameter is small and due to low Reynolds number the response time τ_d to balance the velocity difference $\mathbf{U} - \mathbf{U}_d$ is very small and hence, the Saffman lift force acting on the particle is found to be negligible and is not considered here.

3.3.3 Coupling between carrier and dispersed phase

In the dispersed two-phase flow, the carrier phase and the dispersed phase interact with each other in various ways. The coupling allows exchanging mass, momentum and energy in between the two phases. Evaporation, condensation or sublimation of the dispersed entity are the examples of mass exchange between the two phases. The mass exchange between the phases can also happen due to the chemical

reaction. Momentum exchange between the phases can affect the dynamics of the carrier phase and the dispersed entity. Momentum exchange depends strongly on the flow pattern of the carrier phase and the inertia of the dispersed entities. Energy exchange is an example when thermal augmentation happens in the carrier phase due to hot dispersed entity. In the current work, the phase change is not considered and the isothermal condition is assumed hence, mass and energy coupling is neglected and momentum coupling is considered here.

Momentum coupling

Different approaches are available for coupling of momentum between carrier phase and the dispersed phase and it depends on the dynamics of both the phases expected to be influenced by the presence of each other. The volume fraction, entity spacing and Stokes number are criteria used to distinguish these effects between the phases. The classification of the interacting between the carrier phase and the dispersed phase based on the particle volume fraction made by Elghobashi [127] is as shown in figure 3.3. For particle volume fraction lower than 10^{-6} and spacing between particles (entity spacing) $(L/d) = 100$, one-way momentum coupling between the phases is considered to be sufficiently accurate [122, 128]. In one way coupling, the effect of carrier phase on the dispersed entities is considered. Here the effect of dispersed entities on the carrier phase is negligibly small and hence the source term in the equation 3.9 containing momentum transfer from dispersed phase to the carrier phase is neglected. In one way coupling, the motion of the dispersed entities in the flow is entirely driven by the fluid forces acting on the dispersed entities.

If the dispersed entities volume fraction is greater than 10^{-6} , the effect of the dispersed entities on the carrier phase cannot be neglected and two-way coupling has to be considered. Due to the impact forces imposed on the dispersed entities by the carrier phase, the dispersed entities causes reaction forces on the carrier phase at the position of the dispersed entities. The reaction force caused by the dispersed phase on the carrier phase is modelled by the source term in the Navier-Stokes equation 3.9. The reaction force exerted by the dispersed entity i on the carrier phase is given as

$$\mathbf{F}_{d,i} = - \left(\frac{\mathbf{F}_D + \mathbf{F}_P + \mathbf{F}_g + \mathbf{F}_A}{V_{d,i}} \right) \quad (3.20)$$

The momentum transfer between the phases in the source term in Navier-Stokes equation for a control volume j in a general formulation is given by

$$\mathbf{S} = \frac{1}{V_j} \sum_{i=0}^{N_j} V_{d,i} \mathbf{F}_{d,i}(\mathbf{x}_i) \delta(\mathbf{x} - \mathbf{x}_i) \quad (3.21)$$

In the control volume V_j of the carrier phase, the reaction forces from all the

dispersed entities i are summed up and are weighted by the volume $v_{d,i}$ of the dispersed entities. Due to mass point approximation, the last term in the equation 3.21 shows that the dispersed entities are modelled as Dirac forces at positions x_i .

If the dispersed entities volume fraction is greater than 10^{-3} , the interaction between the dispersed entities can not be neglected and four-way coupling needs to be considered. In the four-way coupling, the dispersed entities along with fluid forces are driven by the collision of the dispersed entities. In the Eulerian-Lagrangian approach, the momentum equation of the dispersed entities is decoupled from each other. Hence, no direct information of the interaction of a dispersed entity with its neighbouring entity is available because of this collision models needs to be considered. To precisely model the collision between the dispersed entities, we need to correlate the entities trajectories in the simulation process to find the intersection. From the position and the relative motion of the dispersed entities, the impact between the dispersed entities can be determined. This direct approach is computationally very expensive and hence is not applicable to the complex problems. However, computationally less expensive stochastic approaches are available to model collision. In a stochastic approach, the inter-collision between the dispersed entities are modelled by the means of collision probabilities. Such methods are reliable at the macroscopic level but are invalid at a microscopic level [122]. However, in the current work due to low particle volume fraction, the collision between the dispersed entities is not considered.

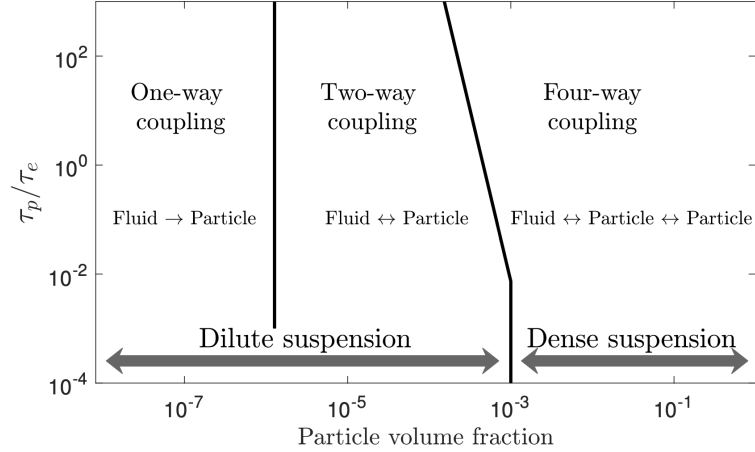


Figure 3.3: Quantification of momentum coupling approach in terms of particle volume fraction and Stokes number reported by Nakhaei et al. [129]

3.4 Turbulent dispersed flow

Interaction of the dispersed entities with the turbulent carrier phase is one of the important aspects in turbulent dispersed flows. Several investigators have studied

turbulence in dispersed flow in past. Hetsroni [130] studied turbulent particle-laden flow experimentally and reported that the particles with low Reynolds number tends to decay turbulence in carrier phase and particles with Reynolds number higher than 400 tends to enhance the turbulence in carrier phase. Gore and Crowe [82, 131] carried the comparative study of turbulence behaviour and related it to the ratio of particle diameter and turbulent length scale. They reported that the transition in low to amplification of turbulence occurs when particle size is of 1/10 of turbulent integral scale as shown in figure 3.4.

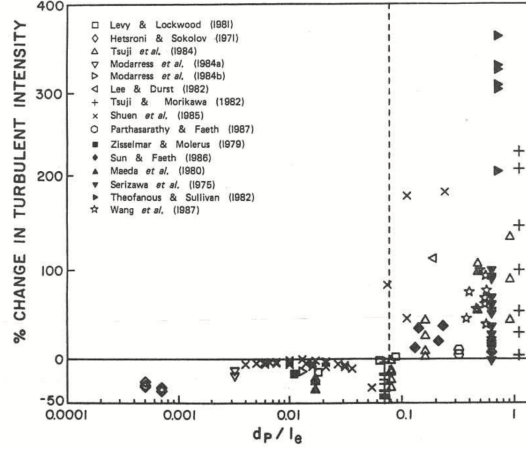


Figure 3.4: Effect of particle size on turbulence intensity reported by Gore and Crowe [82]

To classify the effect of particle size on turbulence, Elghobashi [127, 132] proposed a map as shown in figure 3.5. For the particle volume fraction of less than 10^{-6} , the one-way coupling is considered and it is assumed that the particles do not affect the carrier phase turbulent structure. For particle volume fraction of less than 10^{-3} , the two-way coupling is considered. In the two-way coupling region, the presence of particles can decay or enhance turbulence depending on the Stokes number of the dispersed flow. For the particle volume fraction is greater than 10^{-3} , four-way coupling in the carrier phase and the dispersed phase is considered. In the four-way coupling region, the turbulence of the carrier phase is affected by the oscillatory motion of the particles caused due to the collisions of the particles.

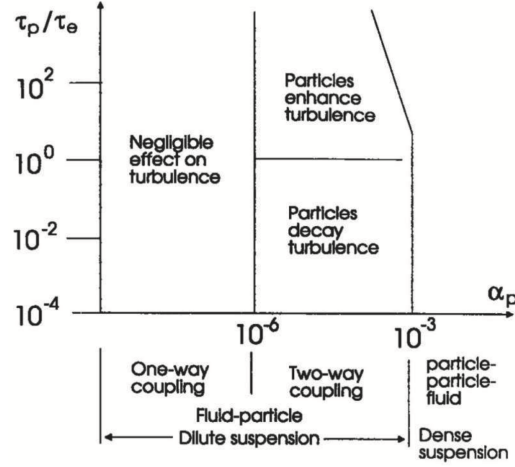


Figure 3.5: Effect of Stokes number and particle volume fraction on turbulence modulation reported by Elghobashi [127]

The turbulence models for single-phase flows can be applied to the Eulerian-Lagrangian approach since this approach has one continuous phase. However, for the chosen turbulence model the transport coefficients and the source terms has to be modified in order to take the presence of dispersed entity into account. The most commonly used approaches to model turbulence using the Eulerian-Lagrangian approach is discussed in this section.

3.4.1 Direct Numerical Simulation

Direct Numerical Simulation (DNS) is the most straightforward and most costly method to model turbulence. This method is the most accurate method to predict turbulence since in this approach all the turbulent length scales are resolved. The computational mesh used in this method is resolved up to the Kolmogorov scale which makes this method computationally expensive. In the DNS method, there are no restrictions with momentum coupling (one way, two way or four-way coupling) with Lagrangian particles since all the turbulent length scales are resolved here. However, in this method to ensure accurate prediction of the carrier phase and dispersed phase interaction, the size of dispersed entities cannot be greater than the Kolmogorov length scale of the turbulence spectrum.

3.4.2 Large Eddy Simulation

In Large Eddy Simulation (LES), the large scales of the flows are resolved directly and the small scale below the certain cutoff are modelled using sub-grid models. LES method is less computationally expensive than the DNS method. Advantage of LES method is that it predicts accurate large eddies and large eddies are most important in terms of momentum and energy transport. LES offers reasonably

accurate results as large eddies are resolved accurately and the filtered small scale eddies in most cases are regarded as isotropic and homogeneous over time and space average, also independent of overall flow geometry [122]. Although LES provides accurate results, the coupling of LES to the Lagrangian tracking of the dispersed entities is a relatively new topic for CFD community [122]. Elghobashi [127] pointed out while implementing this method in predicting two-way momentum coupled flows that the dispersed entities affect mostly the small scales of turbulent structure and this implies that modification in sub-grid models has to be made.

3.4.3 RANS models

Reynolds-average Navier-Stokes (RANS) models are researched quite extensively in the CFD community for modelling turbulent flow over the last few decades. Many different one equation and two-equation closure model has been derived over past years and applied frequently in complex industrial problems. Among such, two-equation models most widely used are the $\kappa - \epsilon$ model and the $\kappa - \omega$ turbulence model. In these models, the conservative equations are solved for the turbulent kinetic energy and the turbulent dissipation energy along with the Navier-Stokes equation of the mean flow [122]. These turbulence models are robust, well resolved and are implemented in almost all the commercial CFD software available.

In the RANS modelling approach, since only the mean velocity is calculated by the momentum equation and velocity fluctuations are expressed in terms of kinetic energy and its dissipation, the local instantaneous velocity at the position of the dispersed entity is not directly available from the solution of the flow field. To overcome this, researchers have introduced various stochastic approaches to model these velocity fluctuations. Yuu et al. [133] estimated random particle displacement based on the Gaussian distribution corresponding to a dispersion coefficient, Dukowicz [134] estimated it from the Gaussian distribution around the mean velocity with variance related to turbulent kinetic energy. Lockwood et al. [135] introduced diffusional velocity related to the flow velocity gradient and turbulent kinetic energy. Although all these approaches are in a stochastic manner they found to be robust and relatively simple to implement. Discrete Random Walk (DRW) model is one of the popular models used to model the turbulent dispersion of the dispersed entities and is based on the model proposed by Gosman and Ioannides [136]. In the DRW approach, the velocity fluctuation components are estimated based on randomly distribute Gaussian variable whose root mean square values are estimated from the turbulent kinetic energy.

Near-wall modelling

The near-wall region can be largely divided into three main regions as shown in figure 3.6. The first layer close to the wall is called viscous sublayer, here flow is almost laminar and the molecular viscosity plays a dominant role in momentum and mass or heat transfer. The second layer is called the buffer layer, and in this region along with the effects of molecular viscosity effects of turbulence are equally important. The third region is the fully turbulent region, where turbulence plays the dominant role.

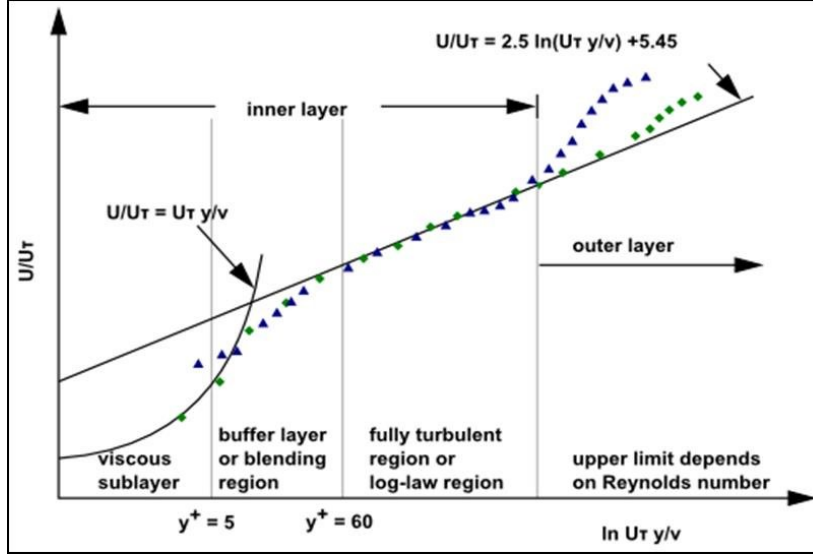


Figure 3.6: Subdivision of the near-wall region [137]

While the RANS modelling approach is robust, computationally less expensive than LES and DNS, the turbulence models in the RANS approach are valid in the area where turbulence is fully developed and underperforms near in the area close to the wall [138]. To deal with this issue, there are mainly two approaches. In the first approach, the turbulence models are modified to enable viscosity affected region to be resolved with the mesh down to the wall including viscous sublayer as shown in figure 3.7 b. To use modified low Reynolds number turbulence models, the first cell centre of the mesh has to be placed in viscous sublayer (i.e. $y^+ \sim 1$). This approach increases the mesh size and makes it computationally expensive. The second approach to deal with this is to use wall functions as shown in figure 3.7 a. The empirical equations used to satisfy the physics between the fully developed turbulent region and the wall is called wall function. Wall functions essentially bridge the gap between the wall and the fully developed turbulent region by providing near-wall boundary conditions to the momentum and turbulence transport equations at the first cell of the mesh near the wall [138]. Use of wall functions requires placing the first cell of the mesh near the wall in the log-law region (i.e. $y^+ \sim 60$) which significantly reduces the mesh size making

it less computationally expensive.

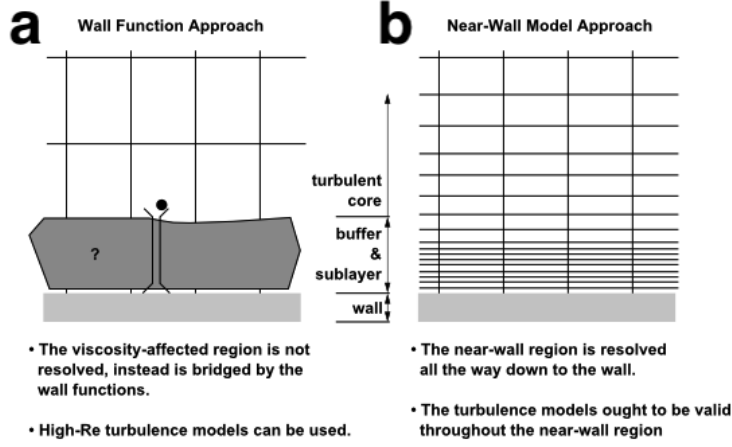


Figure 3.7: Near-wall modelling approach [137]

In OpenFOAM solver, two types of wall functions are available for the turbulent kinetic and dissipation energy. The wall functions such as *kqRWallFunction*, *epsilonWallFunction*, *omegaWallFunction* are suitable for the flow with high Reynolds number. The wall functions such as *kLowReWallFunction*, *epsilon-LowReWallFunction* are suitable for flow with low and high Reynolds number and the conditions are based on the position of the y^+ . The detailed mathematical descriptions and working of each of the mentioned wall functions can be found in the report submitted by Liu [138].

Over past years, researchers [110, 116, 139] have used the RANS modelling approach along with the Eulerian-Lagrangian method to predict erosion and has shown reasonably accurate erosion predictions. As the RANS approach is less computationally expensive than DNS and LES, robust, simple to implement and has shown reasonably accurate erosion predictions, the RANS approach is used in the present work.

3.5 Erosion Solver in OpenFOAM framework

The open-source C++ libraries called OpenFOAM is used to simulate fluid flow and track lagrangian particles. In OpenFOAM, the Lagrangian particle can be represented in *SolidParticle* or *KinematicParcel* class [58]. In *SolidParticle* class, each particle is tracked separately, which makes *SolidParticle* class computationally expensive [58]. While in *KinematicParcel* class, particles can be treated and tracked as a set or a group of particles. *KinematicParcel* class provides several submodels that can be added to Lagrangian particle cloud class among which *ParticleErosion* is one of the submodels. *KinematicParcel* class provides the option to have single or multiple numbers of particles in a single parcel. Being less computationally expensive for practical engineering problem and option to have single or multiple particles in a parcel, *KinematicParcel* class was selected to construct the erosion solver. In *ParticleErosion* submodel of *KinematicParcel* class, six different erosion models discussed earlier in section 2.3 are implemented.

Erosion solver is constructed using *pimpleFoam* solver in OpenFOAM. *pimpleFoam* is a transient solver for an incompressible Newtonian fluid. As discussed in section 3.3, in the constructed erosion solver fluid flow is simulated using the Eulerian approach by solving Reynolds Average Naiver Stokes (RANS) equations. At each time step, ensemble-averaged of fluid flow components are computed in each computational cell such as fluid velocity. At each time step, using the calculated fluid velocity in each computational cells, the relative velocity of the particle along with various forces acting on the particle is calculated. Using these computed relative velocity and forces acting on particles Newton's equation of motion is solved for each particle as discussed in section 3.3. By solving Newton's equation of motion particle trajectories are computed. In the run time of simulation at each timestep, the particle's position is calculated and updated. During each time step, solver checks if the newly computed particle's positions hit any of the boundary patches, and if it does, then solver checks if any submodels are active at these patches. For example, if particle hits the wall boundary patch, it checks if *ParticleErosion* submodel is active at this patch else, it will rebound the particle. If *PaticleErosion* model is active at the boundary patch where particle hits, then it will merely pass particle information to *ParticelErosion* submodel such as particle velocity.

When *ParticleErosion* submodel is activated, *ParticleErosion* submodel calculates erosion with updated particle information at that respective surface. Figure 3.8 shows a schematic of how erosion is calculated at each cell face on the target surface. Figure 3.8 shows the cell faces on the target surface boundary patch. At each time step particle position is updated, and if particle hits this target wall boundary patch, *ParticleErosion* submodel is activated. As *ParticleErosion* submodel is activated upon particle impact, it calculates the particle's velocity

relative to the patch. As shown in figure 3.8, \mathbf{U} is the velocity of the particle hitting the boundary patch and \mathbf{n} is the surface normal vector of the cell face on the boundary patch. If the inner product of the surface normal vector \mathbf{n} and the particle velocity \mathbf{U} is less than zero then the particle travels away from the boundary patch. If not, then the particle velocity unitary vector \mathbf{U}_{dir} (showing direction of particle at impingement) is calculated as

$$\mathbf{U}_{\text{dir}} = \frac{\mathbf{U}}{\text{mag}(\mathbf{U})} \quad (3.22)$$

The impact angle of the particle on the boundary patch is calculated from the surface normal vector \mathbf{n} of the cell face on the boundary patch and the particle velocity unitary vector \mathbf{U}_{dir} as,

$$\alpha = \frac{\pi}{2} - \cos^{-1}(\mathbf{n} \cdot \mathbf{U}_{\text{dir}}) \quad (3.23)$$

The particle information such as particle velocity magnitude U , the impact angle α along with respective erosion model's constant and exponent and particle, material properties are provided to the erosion equations. Erosion equations then calculate erosion rate at the respective cell face on the patch and stores calculated erosion value as scalar value at respective cell face centre. At every time step erosion is calculated, and old scalar value of erosion at the cell face centre is updated by cumulative addition.

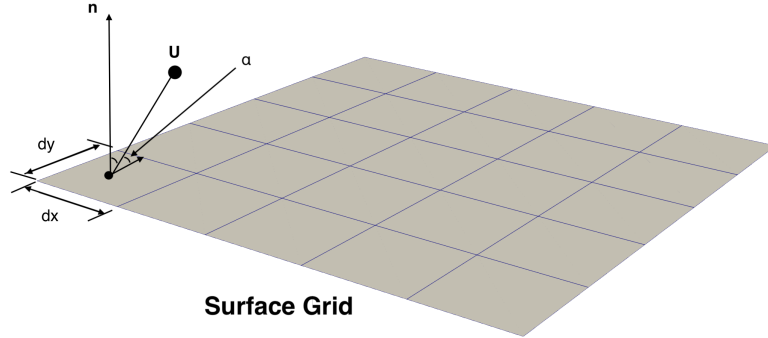


Figure 3.8: Schematics representation showing erosion calculated at the cell face on the target surface.

3.5.1 Erosion Solver Outline

Figure 3.9 outlines flow chart of one-way coupled CFD based erosion solver constructed in OpenFOAM framework. As shown in figure 3.9, solver starts at time = 0; it reads the initial and boundary conditions for the test case along with fluid properties. User-specified turbulence model is then activated. With an initial guess of pressure, it solves momentum equations and calculates the velocities. Using these calculated velocities, it solves the pressure correction equation and then with updated pressure, it solves the momentum correction equation. This calculation for the pressure correction is iterated in a loop until the velocities satisfy the mass conservation equation.

As solution converges to the given criteria for the fluid flow for the respective time step, next is the lagrangian phase. Here at first particles are injected using a user-specified injection model at and for user-specified time. The particle's relative velocity to the fluid is calculated; subsequently, various forces acting on a particle are calculated such as drag force, pressure force etc. Particles position is then calculated by using particle's velocity and forces acting on the particle by solving Newton's equation of motion. After updating the particle's position solver checks if the particle has hit the surface patch where *ParticleErosion* submodel is active, if not it merely rebounds particle using particle-wall interaction model. If particle hit a surface patch where *ParticleErosion* model is active, then *ParticleErosion* submodel calculates particle's velocity relative to the patch and calculates particle impact angle at the respective cell face on the patch. Erosion equations implemented in *ParticleErosion* submodel then gets the information of particle velocity and impact angle. This particle information, along with particle properties, material properties, and erosion model constants are then provided to erosion equations to calculate erosion at the respective cell face on the respective patch. The calculated erosion scalar information is then stored at the cell face centre of the respective patch. If the lagrangian time step is smaller than the Eulerian time step, it will repeat the process; else it will update the current time step by $t = t + \Delta t_E$. If the current time step is greater or equal to end time step, the solver will stop, or it will iterate the process.

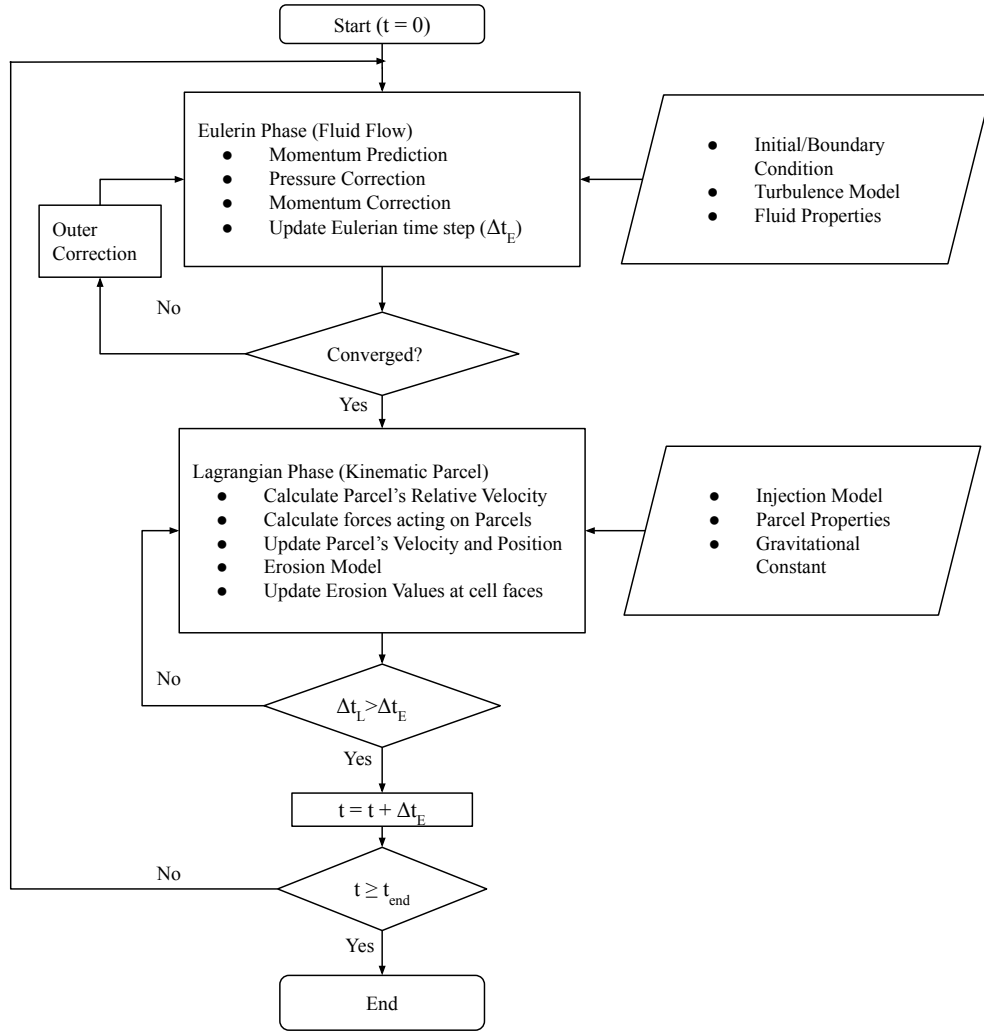


Figure 3.9: Flow Chart of the CFD based erosion solver in OpenFOAM framework (One-way coupled)

3.6 Summary

In this chapter, the working of the constructed CFD based erosion solver in OpenFOAM framework is presented. The governing equations to simulate two-phase dispersed flow using the Eulerian-Lagrangian approach is discussed briefly. The CFD based erosion solver is a constructed using *pimpleFoam* solver in OpenFoam which is capable of simulating incompressible flows. The validation of the CFD based erosion solver and implemented erosion equations will be discussed in later chapters.

Chapter 4

Validation of Erosion Solver

For accurate erosion prediction, it is essential to model flow field and particle tracking accurately. When particles hit the target wall, particle information such as particle velocity and impact angle along with material and model constants are provided to the erosion models. Erosion models then calculate erosion rate at each cell face on the boundary patch of the target surface. For accurate calculation of erosion rate, it is crucial to provide accurate particle velocity and impact angle information to erosion models. In order to test implemented erosion models, it is necessary to validate CFD based erosion solver with its capability to model the fluid flow and particle tracking. In this chapter, the CFD based erosion solver and the implemented erosion models are validated. In the first section, CFD based erosion solver is validated for its capability to predict particle velocity and impact angle on the target wall surface for slurry jet impact and dry jet impact cases. Later, erosion models implemented in the CFD based erosion solver are validated with AISI-1018 dry jet impact test case.

4.1 Slurry Impact Test Case

The CFD based erosion solver is validated using experimental data reported by Mansouri et al. [140, 141]. Particle axial and radial impact velocity along with particle impact angle at the target surface is validated against experimental data [140, 141]. In experimental submerged slurry impact test case by Mansouri et al. [140, 141], a slurry of sand and water was used with 1% sand concentration by weight. The nozzle diameter (D) of 7.6 mm was used, and the standoff distance between the nozzle and the target wall was 12.7 mm. The target wall used in simulation is of diameter 35 mm. The velocity of the slurry (sand water mixture) at the inlet was 8.15m/s, and the mean particle size was 300 μm .

4.1.1 Computational Domain

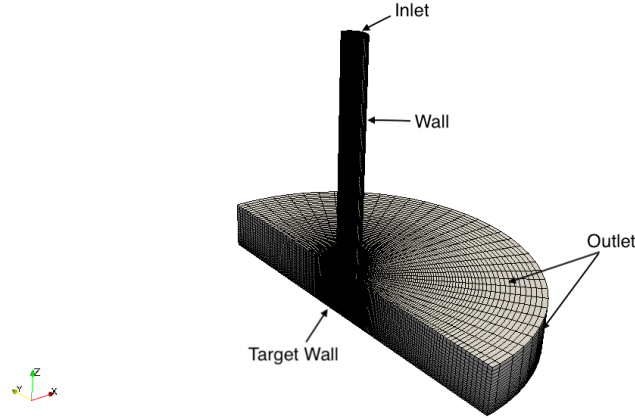


Figure 4.1: Cut section of Computational Domain

Computational domain and mesh used to analyse the submerged slurry impact jet case are created using the *blockMesh* utility in OpenFOAM with the same dimension as reported in the experiment [140, 141]. The nozzle length of 156 mm is chosen ($L \approx 12D$) in order to achieve the turbulent inlet profile at the nozzle exit. To avoid the influence of far-field boundary on the impacting jet, far-field was created of diameter $12D$. Geometry created is as shown in figure 4.1. The structured mesh is generated using the block-Mesh utility. In order to capture jet core and near-wall particle interaction, the mesh is refined at the jet core and the near the wall region, as shown in figure 4.2.

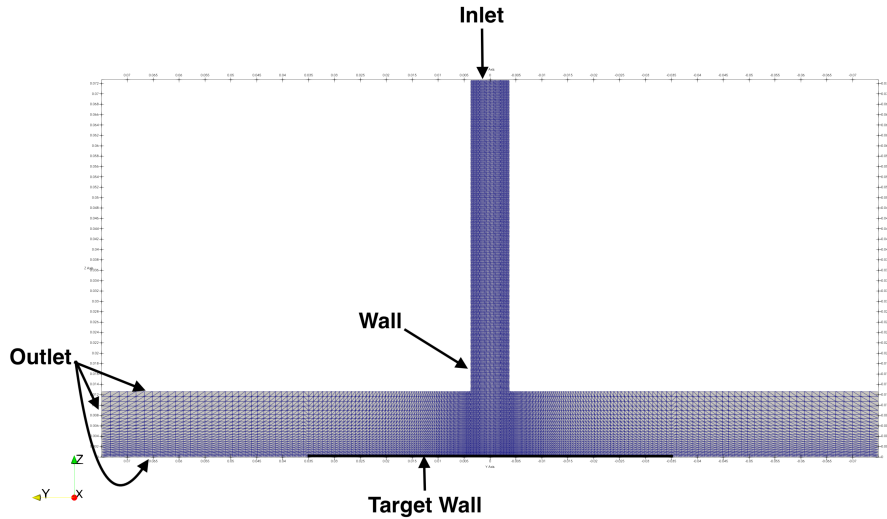


Figure 4.2: Computational mesh showing grid refinement at the core and near the wall

4.1.2 Mesh Independence Study

For mesh independence study, multiple meshes with different cell counts are created. The axial velocity of the fluid at the jet centre line and radial velocity at half of the jet length are compared for mesh independence study. The mesh independency of the numerical study has been performed by comparing the results obtained at different mesh sizes. The number of cells in each mesh used for mesh independence study is as summarised in table4.1.

Table 4.1: Mesh Size

Mesh	Number of Cells	Y+	First layer thickness (μm)
Mesh 1	128,400	30	300
Mesh 2	192,372	30	300
Mesh 3	236,164	30	270
Mesh 4	287,040	30	270

The CFD based erosion solver is used for simulating the test cases. Experimental test conditions are applied for the simulation's initial and boundary conditions. The velocity of -8.15 m/s is applied at the inlet, and no-slip wall condition is applied at the wall. As discussed in section 3.4.3, to model turbulence using the RANS approach, $\kappa - \epsilon$ turbulence model is applied with *kLowReWallFunction* for κ and *epsilonLowReWallFunction* for ϵ . These near-wall functions were used as it offers hybrid near-wall treatment for low and high Reynolds number, and it depends on mesh resolution near the wall [138]. In each mesh, although cell count is different, the first layer of the cell is set using an average $y+ \approx 30$. The turbulence model $\kappa - \epsilon$ and $y+ \approx 30$ is employed based on the numerical study performed by Zhang et al. [139] to study the effect of the turbulence model and near-wall treatment for a similar test case. To get an optimum mesh size, only fluid flow is modelled in these simulations and particles are not injected.

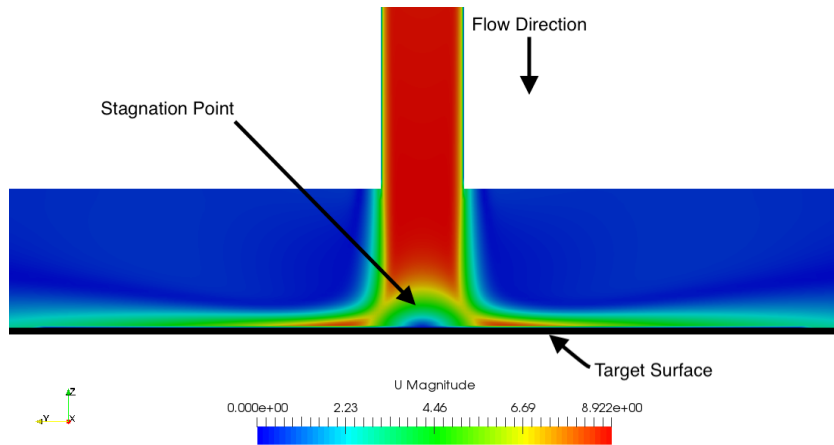


Figure 4.3: Velocity contour plot at an inlet velocity of 8.15 m/s

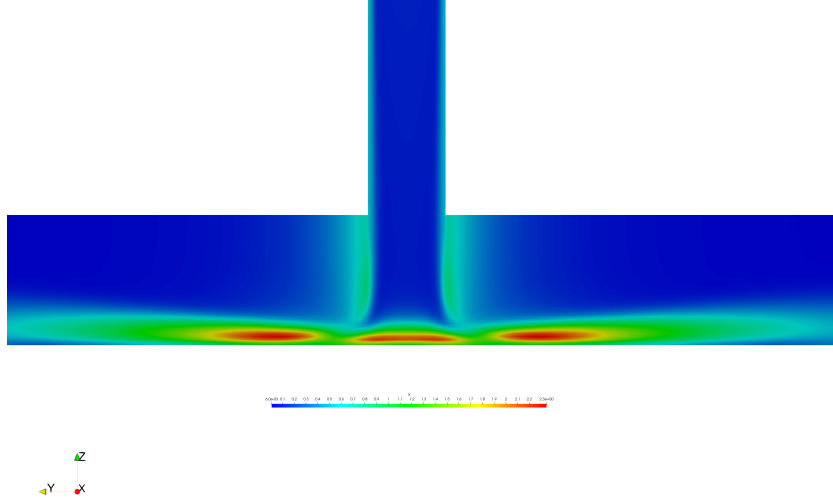


Figure 4.4: Turbulence Kinetic energy contour plot at an inlet velocity of 8.15 m/s

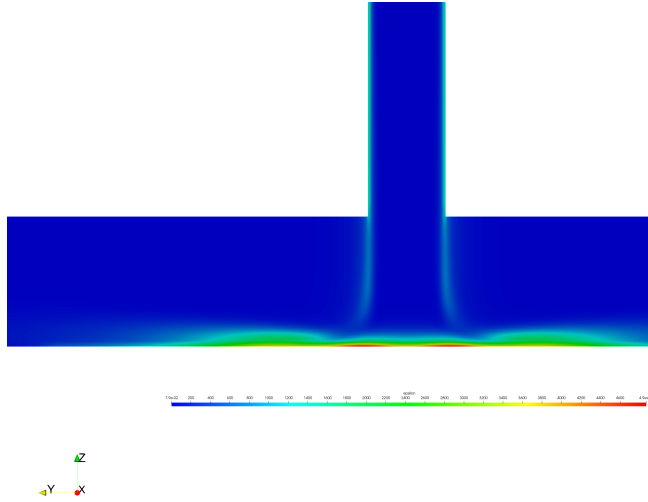


Figure 4.5: Turbulence dissipation rate contour plot at an inlet velocity of 8.15 m/s

Figure 4.6 shows that in the simulation test cases for mesh independence studies; each mesh predicted a similar trend for axial velocity and the turbulent quantities of the fluid. Figure 4.6a shows the calculated axial velocity along the centre-line of the jet. The velocity of fluid found to be maximum at the nozzle exit, gradually reducing near the impacting target wall. Figure 4.6b shows axial velocity away from the centre-line at height 6 mm above the target wall. The velocity of fluid found to be maximum in the jet core region and decreases gradually away from the jet core. At the centre of the jet core, velocity of fluid drops slightly;

this is due to the presence of the stagnation zone on the target wall; this can also be seen in figure 4.3. Figure 4.6c and 4.6d, shows the turbulence dissipation rate and the turbulent kinetic energy along the centerline of the jet, respectively.

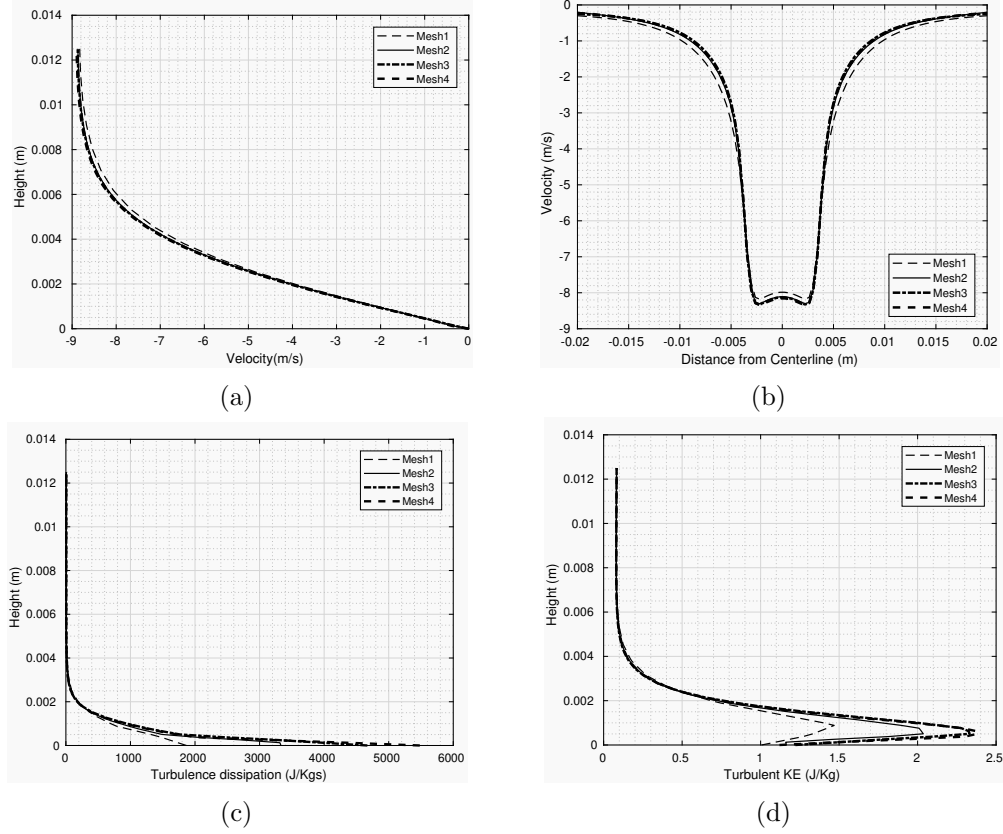


Figure 4.6: a) axial velocity along the centre-line of the jet, b) Axial velocity at height of 0.006 m of the jet centre-line, c) Turbulence dissipation rate along the centre-line of the jet and d) Turbulence Kinetic Energy along the centre-line of the jet

The accuracy of the predicted results improved as the mesh is refined from coarse to fine. Above predicted results showed that no comparable difference in the predicted results is observed with fine meshes, i.e. mesh 4 and mesh 5. Being less computationally expensive, mesh 4 is selected for further simulations.

4.1.3 Solver Parameters

After mesh independence study, fluid flow prediction and particle tracking are performed using mesh 4. For fluid flow modelling, similar parameters to experimental conditions [140, 141] are used. In the experimental conditions, the slurry inlet velocity was 8.15 m/s at the inlet, particle concentration of 1% on mass bases and the particle diameter is $300\text{ }\mu\text{m}$ with a density of 2650 kg/m^3 was used. Fluid flow is modelled by solving the RANS equations. PIMPLE (PISO + SIMPLE) algorithm is used for pressure velocity coupling. Semi-Implicit-Method-Of-Pressure-Linked-

Equations (SIMPLE) algorithm do not have time derivative and hence it is used for a steady-state analysis, while Pressure-Implicit-Of-Split-Operations (PISO) algorithm having time derivative is used for transit calculations. The calculations using PISO algorithms is limited to the time step based on the Courant number ($C < 1$). However, PIMPLE algorithm is merged PISO and SIMPLE algorithms and the main advantage of this algorithm is that larger Courant number ($C \gg 1$) can be used, therefore the time step can be increased drastically. For convective and diffusive terms in RANS equations, second-order upwind scheme and second-order central differencing scheme are used respectively. Newton's equation of motion is solved using the first-order scheme for calculating particle trajectories. The time step here is limited using the Courant number ($C < 0.3$).

Drag force and gravitational force experienced by the particles are also considered here. In the experimental study [140, 141], non-spherical particles were used. There are many models available to estimate the drag coefficient for the non-spherical particles, among such the most popular drag coefficient for the non-spherical particle are of Haider and Levenspiel [104], Ganser [142], Hölzer and Sommerfeld [143] etc. Haider and Levenspiel [104] model is one of the earliest generalised correlation for estimating drag coefficient of non-spherical particle and is based on the Reynolds number (Re) and the sphericity (ϕ) of the particle. Bagheri and Bonadonna [144] analysed many different drag models for non-spherical particles and showed that Haider and Levenspiel [104] model performed well for estimating drag of non-spherical particle. Similarly, Mansouri et al. [140] used Haider and Levenspiel [104] drag model in their numerical analysis while using non-spherical particles. Due to the non-spherical shape of particle Haider and Levenspiel [104] drag coefficient C_D , suitable for the non-spherical particle is used here. Coefficient of drag used in the simulation test case is calculated from,

$$C_D = \frac{24}{Re}(1 + ARe^B) + \frac{C}{1 + \frac{D}{Re}} \quad (4.1)$$

$$A = \exp(2.3288 - 6.4581\phi_s + 2.4486\phi_s^2) \quad (4.2)$$

$$B = 0.0964 + 0.5565\phi_s \quad (4.3)$$

$$C = \exp(4.905 - 13.8944\phi_s + 18.422\phi_s^2 - 10.2599\phi_s^3) \quad (4.4)$$

$$D = \exp(1.4681 - 12.2584\phi_s + 20.7322\phi_s^2 - 15.8855\phi_s^3) \quad (4.5)$$

where, A , B , C , and D are coefficients and are calculated using spherical coefficient ϕ_s . The spherical coefficient is given as $\phi_s = s/S$, where s is the surface area of a sphere having a similar volume of the particle, and S is actual surface area. Considering particle as sharp as mentioned in experimental conditions [140, 141] and assuming it as cube shape, $\phi_s = 0.8$ is used. As particle mass loading is less

than 1%, the particle-particle collision effect is neglected, and two-way coupling between particle and fluid is considered here. Parcel injection rate used in the simulation is about 5200 parcels per second, where each parcel consists of 100 particles. Over 100,000 such parcels were injected from the nozzle and tracked as they hit the target surface. Reason for using the high number of particles, it is to ensure that the average impact data is independent of the number of particles impacting the target surface.

In experimental conditions, mean particle size is given as 300 μm , but not all particles are of the same size [140, 141]. The experimental condition provides detailed particle size distribution used in the experiment. This particle size distribution is incorporated in solver using Rosin-Rammler size distribution function. Rosin-Rammler size distribution is given as

$$Y_d = e^{\left(\frac{-d_p}{\bar{d}_p}\right)^n} \quad (4.6)$$

Where, Y_d is volume fraction, d_p is the diameter of the particle, \bar{d}_p is mean diameter of particle and n is spread parameter. Using MATLAB curve fitting tool and experimental data [140, 141] value of $n = 4.5$ is obtained. Rosin-Rammler curve fit plot for the particle size distribution as reported in the experimental conditions [140, 141] using a spread parameter of 4.5 is as depicted in figure 4.7.

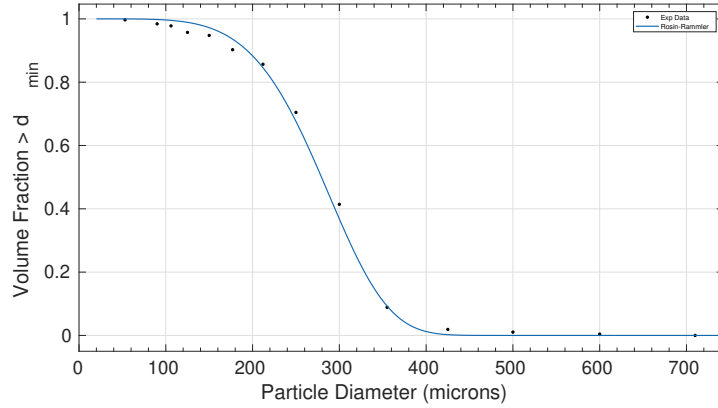


Figure 4.7: Rosin-Rammler fit function for the particle size data reported by Mansouri et al. [140]

4.1.4 Results and Discussion

Figure 4.8 shows the calculated average impact angle and average impact velocity magnitude of the particle for the submerged slurry jet impact test case by the CFD based erosion solver. The method used to calculate particle velocity and the impact angle is as explained in section 3.5. Figure 4.8a shows the time-averaged particle impacting velocities while particles hit the target surface. In slurry jet core centre, it is observed that as particles approach the target surface, its normal

velocity component decreases, this may be due to the presence of a stagnation region on the target wall. It is moving radially away from the jet core, normal velocity decreases and the tangential velocity increases. This can be seen in figure 4.8a that the high-velocity ring is formed along the jet core region. Figure 4.8b shows the time-averaged impact angle distribution on the target surface while particles hit the target surface. In slurry jet, particles hit the target surface at a wide range of impacting angles from approximately $5^\circ < \alpha < 90^\circ$. Particles hit at the maximum angle of impact at the jet core and decrease gradually away from the core.

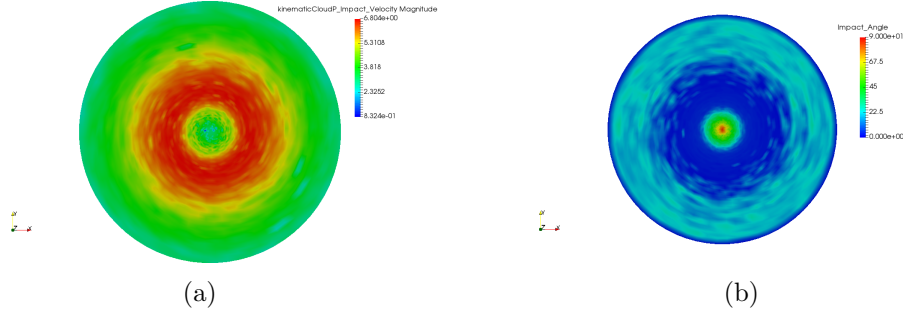


Figure 4.8: Average particle information predicted on the target surface (35 mm diameter) at inlet velocity of 8.15m/s . a) Average particle impact velocity magnitude, b) Average impact angle of particles

In slurry flow, due to high viscosity of liquid compared to gas, particle relaxation time decreases by order of magnitude. Hence, in the slurry flow with low stokes number, fluid flow effect dominates particle inertia and its trajectories. This makes the particles to follow the fluid flow path and causes curvature in particle trajectories near the target surface. Hence, particle as that of fluid flow hit the target wall in slurry jets with a wide range of impact angles, and high-velocity ring away from jet core is observed.

Figure 4.9 shows a comparison of CFD simulation results and experimental data [140, 141] using CFD based erosion solver. Figure 4.9a shows the axial component of particle velocity and figure 4.9b shows the radial component of velocity at the target surface and experimental data along with its standard deviation. Particle velocity predicted by the CFD based erosion solver matches reasonably accurate with experimental data, especially in the jet core region and are within the error bar of experimental data.

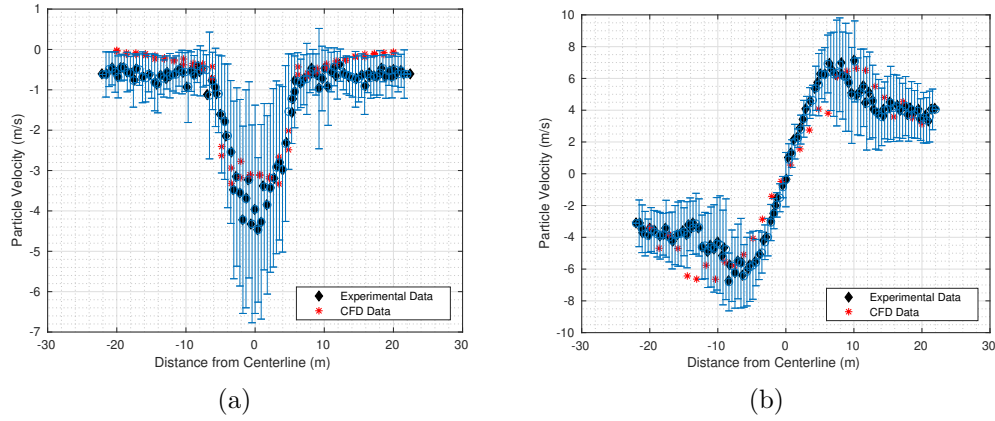


Figure 4.9: Average particle information predicted on the target surface at inlet velocity of 8.15 m/s . a) Particle axial velocity on the target surface, b) Particle radial velocity on the target surface, experimental data reported by Mansouri et al. [140, 141]

In the test case simulated without size distribution function size, i.e. all of the particles simulated are of $300\text{ }\mu\text{m}$ size. In contrast, the test case with particle size distribution function had particles with size ranging from $50\text{ }\mu\text{m}$ to $700\text{ }\mu\text{m}$. Figure 4.10b shows the average impact angle of particles predicted on the target surface using constant particle size. The results show that the average impact angle of uniform particle size matches well with the experimental data near the jet core but shows comparable results away from the jet core region. While in figure 4.10a, it can be observed that the test case with particle size distribution function predicts a better angle of impact near the jet core as well as away from the jet core region. The bigger particle with higher Stokes number dominates the fluid flow due to inertia and tend to move straight. Comparatively smaller particles are strongly coupled with fluid flow due to low inertia and change its path along with fluid, i.e. near the target wall. Hence in figure 4.10a, particles hit the target surface with bigger impact angles away from the jet core. This emphasised that the CFD based erosion solver predicts impact angle well at the jet core in both with and without particle size distribution function, but it is crucial to use size distribution function to predict smaller particle's impact angle away from the jet core.

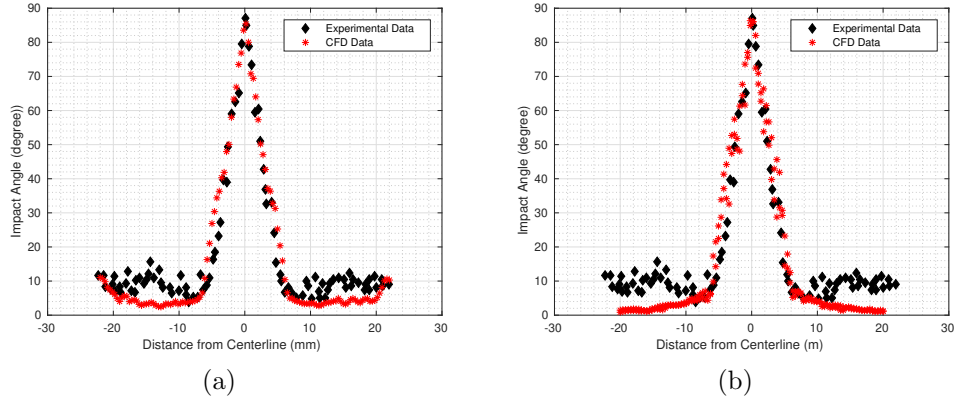


Figure 4.10: Average particle impact angle predicted on the target surface at inlet velocity of 8.15m/s . a) Using Rosin-Rammler size distribution function, b) Using constant particle size ($300\mu\text{m}$), experimental data reported by Mansouri et al. [140, 141].

To understand the effect of the turbulence models on the particle impact angle and the particle impact velocity, three different cases are simulated using $\kappa\text{-}\omega$, $\kappa\text{-}\epsilon$ and $\kappa\text{-}\epsilon\text{-RNG}$ turbulence models. In the standard $\kappa\text{-}\epsilon$ turbulence model transport equations for turbulent kinetic energy and its dissipation rate is solved. This model assumes that the flow is fully turbulent and the effects of the molecular viscosity are negligible [137]. The $\kappa\text{-}\epsilon\text{-RNG}$ model is based on a statistical technique called renormalizing group theory. The model contains an additional term in dissipation rate which improves accuracy in rapidly strained flows [137]. The RNG model contains the effect of swirl on turbulence and hence enhances the accuracy in predicting swirling flows. In the $\kappa\text{-}\omega$ turbulence model the transport equations for the turbulent kinetic energy and its specific dissipation rate is solved. The model predicts free shear flow spreading rates, mixing layers, and jets, and is thus applicable to wall-bounded flows and free shear flows [137].

Figure 4.11, shows results of particle impact angles calculated using $\kappa\text{-}\omega$, $\kappa\text{-}\epsilon$ and $\kappa\text{-}\epsilon\text{-RNG}$ turbulence models. CFD simulation results show that with the particle size of $300\mu\text{m}$ negligible difference is observed for all three different turbulence models (especially at the jet core region). For smaller particles impacting away from the jet core, a small difference in predicted result is observed for the different turbulence models. Although in all the simulation test cases, the mesh count is kept the same, the distance of the first cell near the wall was adjusted according to y^+ value. For $\kappa\text{-}\epsilon$ and $\kappa\text{-}\epsilon\text{-RNG}$ y^+ was kept around 30 and for $\kappa\text{-}\omega$ y^+ was kept less than 5 [145]. Simulation results show that away from the jet core $\kappa\text{-}\omega$ turbulence model overpredicts impact angle slightly while $\kappa\text{-}\epsilon$ slightly under-predicts in the same region. $\kappa\text{-}\epsilon\text{-RNG}$ turbulence models showed better agreement with experimental data at the jet core and away from the jet core.

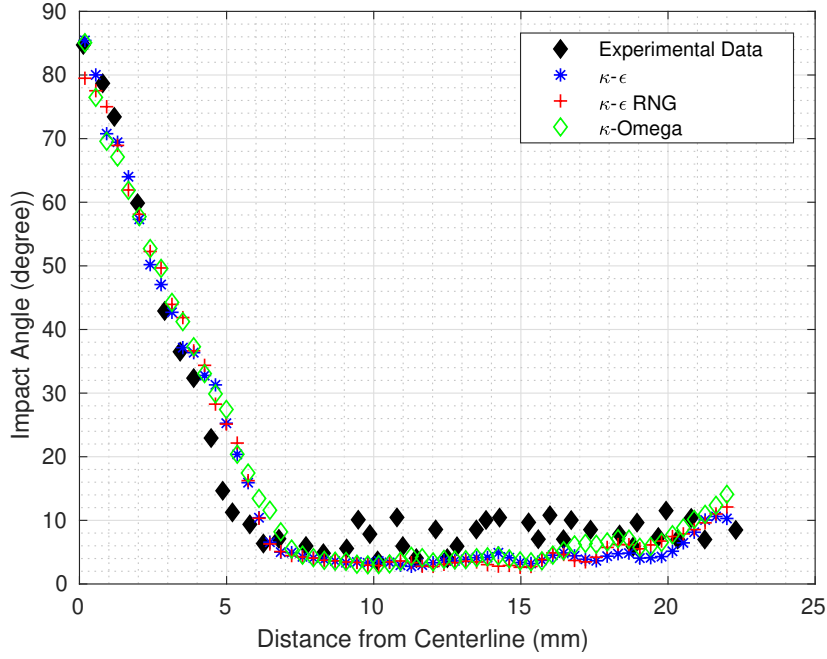


Figure 4.11: Average particle impact angle predicted using different turbulence models, experimental data reported by Mansouri et al. [140, 141].

4.2 Air-Sand Impact Test Case

Mansouri et al. [141] also carried out an experimental study with gas-solid (dry) impact test case. Similar experimental setup, as described in section 4.1.3 was used only replacing fluid from water to air. In experimental conditions, all other parameters such as particle size type were kept the same as described in section 4.1.3. For simulating dry(air-sand) impact test case same domain and mesh as used in section 4.1.3 is used, and only fluid properties are changed from water to air. Around 100,000 particles are tracked, and κ - ϵ -RNG turbulence model is implemented with the Rosin-Rammler size distribution function.

Figure 4.12 shows the average particle impact velocity and impact angle on the target surface for air-sand or dry impact test case. Figure 4.12 shows that particle behaviour in gas-solid flow is different in liquid-solid flow (see figure 4.8). In liquid-solid flow (figure 4.8b), particle impacted the target surface with a wide range of impact angle, but in gas-solid flow, particles impact target surface at a small range of impacting angles (see figure 4.12b). In dry impact simulation test case, the particles are injected through the nozzle at 90° impact angle to the target wall. Figure 4.12b shows that the calculated impact angle at the target wall is mostly 90°. Similarly, in dry impact simulation test case particles are injected at the inlet velocity of 8.15m/s and figure 4.12a shows the majority of particles hit the target wall with the same velocity. This results emphasised that in the dry impact test case particle hit the target surface with the same velocity and angle at

which it exits from the nozzle. There exists a slip velocity between air and sand, but due to small standoff distance in simulated test case result shows this to be negligible. Similar observations about particle impact angle and impact velocity on the target surface were reported by Mansouri et al. [141] in their experimental studies.

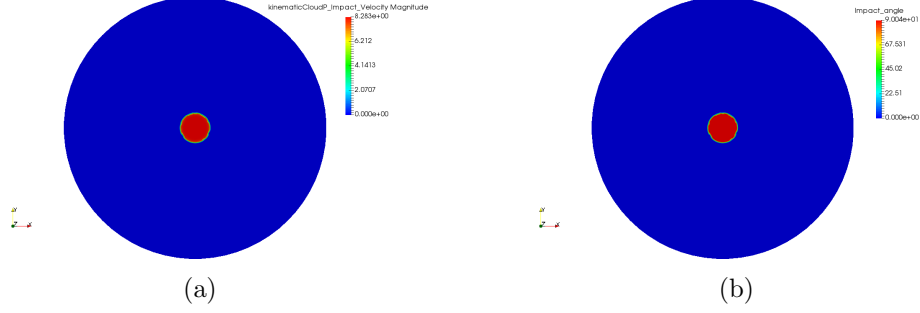


Figure 4.12: Average particle information predicted on the target surface at inlet velocity of $8.15m/s$. a) Average particle impact velocity magnitude, b) Average impact angle of particles

In gas-solid flow, where Stokes number is high, particle inertia dominates the flow effect of fluid on particle trajectories. The impact angle of the particle on the target surface in gas-solid flow is the same as the nozzle's angle with the target surface. One of the reasons why researchers use dry (air-sand) impact test case to develop erosion models is because controlling the particle's impact angle and velocity is easier than in slurry impact test case. Figure 4.13a and 4.13b shows particle impact velocity and angle around centerline of jet. As particle inertia dominates the flow trajectories, particles impact target surface in a small circular area of a diameter similar to the nozzle as depicted in figure 4.12.

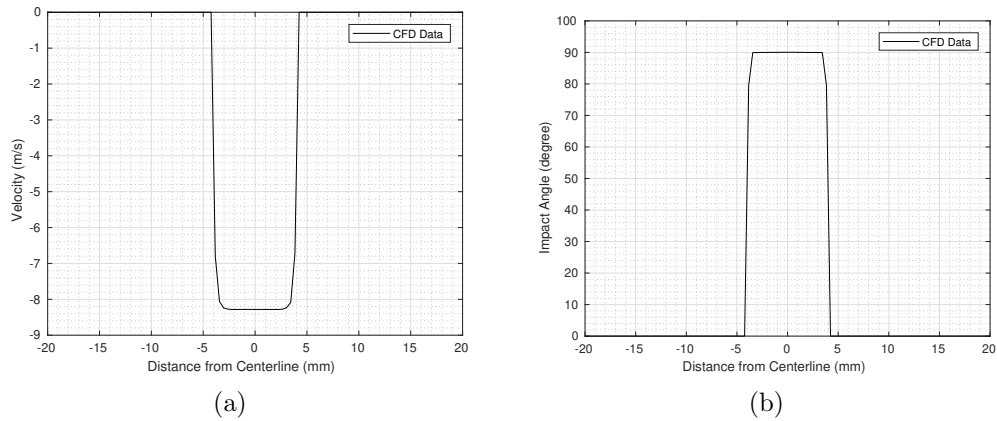


Figure 4.13: Average particle information predicted on the target surface at inlet velocity of $8.15m/s$. a) Particle axial impact velocity magnitude, b) Particles impact angle

Results obtained from the air-sand simple jet simulation test case gives liberty

to test the capability of existing erosion model, not only by CFD simulations but also with analytical code. As particle impact angle and velocity of the particle is the same on target surface as at nozzle exit, analytical MATLAB code with erosion models was developed to test erosion prediction capabilities for the erosion models. MATLAB analytical code enables us to get quick erosion results and modifications can be made in erosion models accordingly. Reliability of MATLAB code is validated by simulating test case using the CFD based erosion solver, and by MATLAB solver. Erosion rates predicted by MATLAB solver and the CFD solver are found similar.

In this chapter in section 4.1 and 4.2 erosion solver is validated with its capability to predict accurate particle impact angle and velocity on the target surface with experimental data [140, 141]. It is observed from the predicted results that for air-sand impact test case with small standoff distance, particle impact angle and speed is nearly same at the target wall at which it exits the nozzle. To validate capabilities of different proposed erosion models air-sand jet impact on pipeline steel (AISI-1018) is simulated in CFD and MATLAB analytical code. Impact test simulations are carried out for four different velocities, impact angles and feed rate using the same particle and target material and other simulation parameters in all test cases. Simulating these test case will give ideas about the advantages and limitations of existing implemented erosion model.

4.3 AISI-1018 Test Case

To validate erosion models implemented in the CFD erosion solver, dry jet impact tests case is simulated and validated against experimental data of Islam et al. [22]. Islam et al. [22] carried out dry impact erosion experimental study on AISI 1018 steel as a target material and using alumina AL_2O_3 as erodent particles. AISI 1018 steel is commonly used steel in the pipeline industry. Particle size used reported in the experimental conditions was around 57 ± 3 microns. Experiments were carried out for four different particle velocities $36m/s$, $47m/s$, $63m/s$ and $81m/s$. For each velocity, experiments were conducted at four different impact angel 30° , 45° , 60° and 90° . Each experiment was carried out for a time of 600 sec. Four different particle feed rates were used with respect to velocities, $126g/min$, $155g/min$, $178g/min$ and $185g/min$. They measured detailed erosion rate and weight loss at each velocity, impact angle and at different time intervals. Having this broad range of experimental data with the same particle and material properties but at different velocities, impact angels and feed rates make it ideal for testing the capability of erosion solver and model. Details of experiments, domain size, mesh used herein the simulation are given in the latter part of this section.

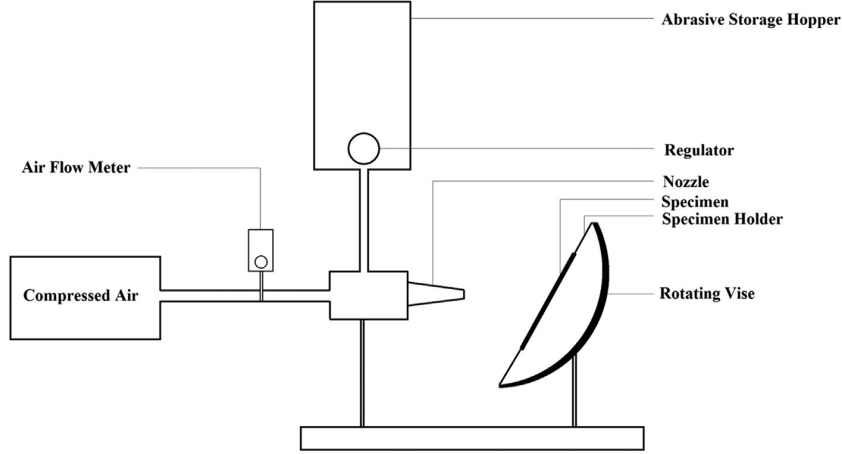


Figure 4.14: Schematic of experimental setup for dry impact test reported by Islam and Farhat [10]

Figure 4.14, shows schematic of experimental set up used by Islam et al. [22]. Nozzle diameter used by Islam et al. [22] here was 2.3mm , and standoff distance from the nozzle to specimen (target wall) was 3mm . They conducted these experiments at room temperature[22].

4.3.1 Computational Domain

Geometry and mesh for the test case are created using *blockMesh* utility which is available in OpenFOAM. Geometry and domain created and used herein simulation are as shown in figure 4.15. Nozzle diameter used here is 2.3 mm , standoff distance between the nozzle and target wall is 3 mm , domain far-field is 60mm in diameter to avoid any influence of boundary on impacting jet.

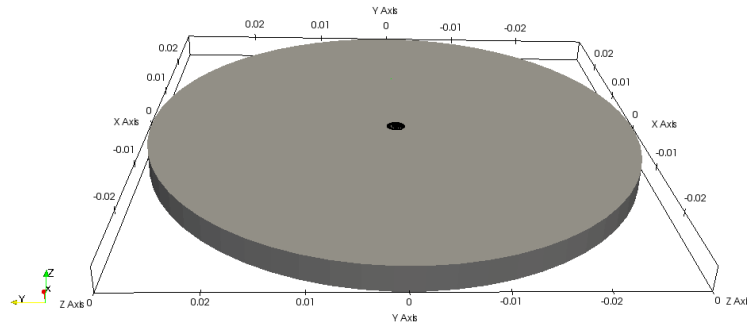


Figure 4.15: Computational domain used for CFD analysis

blockMesh utility is used to create the mesh for the domain, as *blockMesh* has the capability of creating structured hexahedral mesh using block, and it supports

cell size grading and curved block edge. Mesh is refined near the wall and at the core of jet to capture accurate physics. Mesh independence study is carried out to avoid any influence of mesh on the solution. Cut section of the mesh generated is shown in figure 4.16 shows a close view of mesh refinement near the jet core and wall region.

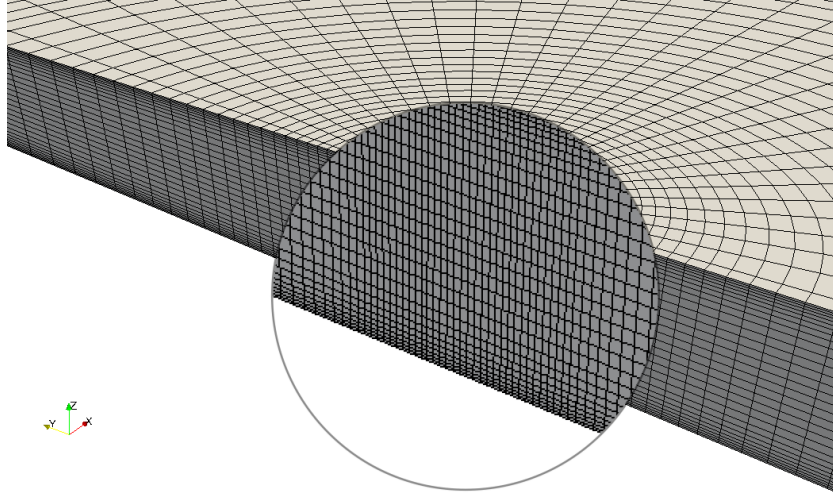


Figure 4.16: Close View of Mesh Refinement

A number of simulations are carried out using the same mesh according to experimental test conditions, and the details of these conditions are outlined in table 4.2.

Table 4.2: Parameters used for CFD analysis

Nozzle diameter	2.3 mm
Standoff distance	3 mm
Particle velocities	36 m/s , 47 m/s , 63 m/s & 81 m/s
Impact angel	30°, 45°, 60°& 90°

4.3.2 Solver Parameters

Simulations are carried out in both the CFD based erosion solver and in analytical MATLAB solver. Different erosion models explained in section 2.3 are implemented in both the CFD based erosion solvers in OpenFOAM CFD and in MATLAB code. For the implemented erosion models, parameters and constants of erosion models used for AISI -1018 test case are listed in table 4.3.

Table 4.3: List of Erosion Model constants and parameters used for test case of AISI 1018

Erosion Model	Symbol	Parameter	Unit	Value
Finnie's Model [13]	P	Plastic flow stress*	kgf/m^2	1.9×10^6
	ψ	Ratio of depth to cut	-	2
	κ	Ratio of vertical to horizontal force	-	2
Bitter's Model [14, 15]	y	Elastic Load Limit*	kgf/m^2	1.76×10^8
	ϕ	Deformation wear factor*	kgf/m^2	5.37×10^7
	χ	Cutting wear factor*	kgf/m^2	1.76×10^8
	q_p	Poisson's ratio of particle*	-	0.21
	q_t	Poisson's ratio of wall*	-	0.29
	E_p	Young's Modulus of particle*	kgf/m^2	4.23×10^{10}
	E_t	Young's Modulus of wall*	kgf/m^2	2.05×10^{10}
	ρ_p	Density of particle*	kg/m^3	3950
	α_{p0}	maximum erosion angle*	degree	18
Neilson's Model [16]	y	Elastic Load Limit*	kgf/m^2	1.76×10^8
	ϕ	Deformation wear factor*	kgf/m^2	5.37×10^7
	χ	Cutting wear factor*	kgf/m^2	1.76×10^8
	q_1	Poisson's ratio of particle*	-	0.21
	q_2	Poisson's ratio of wall*	-	0.29
	E_1	Young's Modulus of particle*	kgf/m^2	4.23×10^{10}
	E_2	Young's Modulus of wall*	kgf/m^2	2.05×10^{10}
	ρ_p	Density of particle*	kg/m^3	3950
	n	Neilson's model constant	-	4.5

Oka's Model [19, 20]	K_P	Model Constant	-	45
	H_V	Vicker's Hardness*	GPa	1.29
	k_1	Model constant	-	-0.05
	k_2	Model constant	-	3.006
	k_3	Model constant	-	0.19
	V'_p	Reference velocity of particle	m/s	104
	d'_p	Reference Diameter of particle	$microns$	326
	n_1	Model constant	-	0.73
	n_2	Model constant	-	2.17
E/CRC Model [17]	C	E/CRC model constant	-	2.17×10^{-7}
	BH	Brinelle's Hardness*	HB	127
	A_1	E/CRC Model constant	-	5.40
	A_2	E/CRC Model constant	-	-10.11
	A_3	E/CRC Model constant	-	10.93
	A_4	E/CRC Model constant	-	-6.33
	A_5	E/CRC Model constant	-	1.42
	n	E/CRC velocity exponent	-	2.41
DNV Model [34]	C	DNV model constant	-	2.9×10^{-9}
	A_1	DNV Model constant	-	9.37
	A_2	DNV Model constant	-	42.30
	A_3	DNV Model constant	-	110.86
	A_4	DNV Model constant	-	175.80
	A_5	DNV Model constant	-	170.14
	A_6	DNV Model constant	-	98.40
	A_7	DNV Model constant	-	31.21
	A_8	DNV Model constant	-	4.17
	n	DNV velocity exponent	-	2.6

Most of these erosion models constants and parameters are default and are as recommended by the respective authors [13–17, 19, 20, 34]. Some of these simulation parameters (marked with \star) are estimated from experimental data with the guideline recommended by the respective authors [13–17, 19, 20, 34] and from experimental conditions.

4.3.3 Results and Discussion

Figure 4.17 shows erosion rate predicted by different erosion models at particle impact velocity of $36m/s$. Y-axis shows predicted erosion rate over different impact angle (X-axis). Figure 4.17a shows predicted erosion results which are obtained by using erosion model constants as reported in the literature by the

respective authors and used as default. Finnie's erosion model predicts erosion rate maximum at an impact angle of around 18° but predicts no erosion at an impact angle of 90° . Bitter's and Neilson's erosion models predict a similar erosion result because Neilson's erosion model is a simplified version of Bitter's erosion model. Both models predict good erosion rate at an impact angle of 30° and 90° but under predicts erosion at impact angle 45° and 60° . E/CRC erosion model over predicts erosion rate at all impact angles.

DNV and Oka's erosion model predicts good erosion results at an impact angle of 90° but under predicts erosion rate for other impact angles. DNV, E/CRC and Oka's model calculates erosion rate at 90° and predicts erosion rate at other impact angles using angle functions. Angle function given for the DNV and E/CRC erosion model is a polynomial function, and even if we modify it will be test case dependent. For Oka's erosion model given angle function has some constants which Oka et al. [19][20] has reported for specific particle and target material. These model constants in present study are obtained by using MATLAB curve fitting tool and experimental data [22]. For Oka's erosion model, these angle function constants, i.e. n_1 and n_2 are obtained here by curve fitting using experimental data. Using modified angle function constants for Oka's erosion model, erosion rate predicted for all the impact angle at particle velocity of 36m/s are plotted in figure 4.17b. Modified constants for Oka's angle function found slightly underpredicting the erosion rate at an impact angle of 60° but predicting better erosion rate at all impact angles compares to the earlier one (see figure 4.17a). For the simulation test cases with other velocities modified Oka's angle function constants are used.

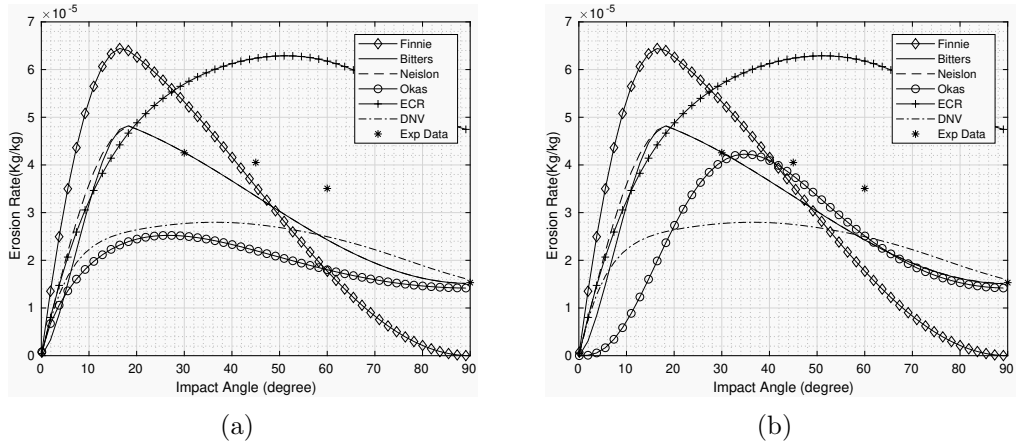


Figure 4.17: Erosion rate vs Impact Angle (AISI 1018) at particle velocity of 36m/s , a) Standard constants for erosion model, b) modified constant for Oka's angle function (n_1 & n_2), experimental data reported by Islam et al. [22]

Figures 4.18a, 4.18b, 4.18c and 4.18d show erosion rate prediction results with the implemented erosion models at 36m/s , 47m/s , 63m/s and 81m/s particle

velocity. The constants and exponents required for erosion models are evaluated from experimental data at 36m/s particle velocity. Figure 4.18a shows erosion for particle velocity of 36m/s . At this velocity it is observed that Neilson's, Bitter's and Oka's erosion model predicts erosion rate at good margins. As particle velocity increase most of the models overpredicted erosion rate at all the impacting angels as seen in figure 4.18b, 4.18c and 4.18d.

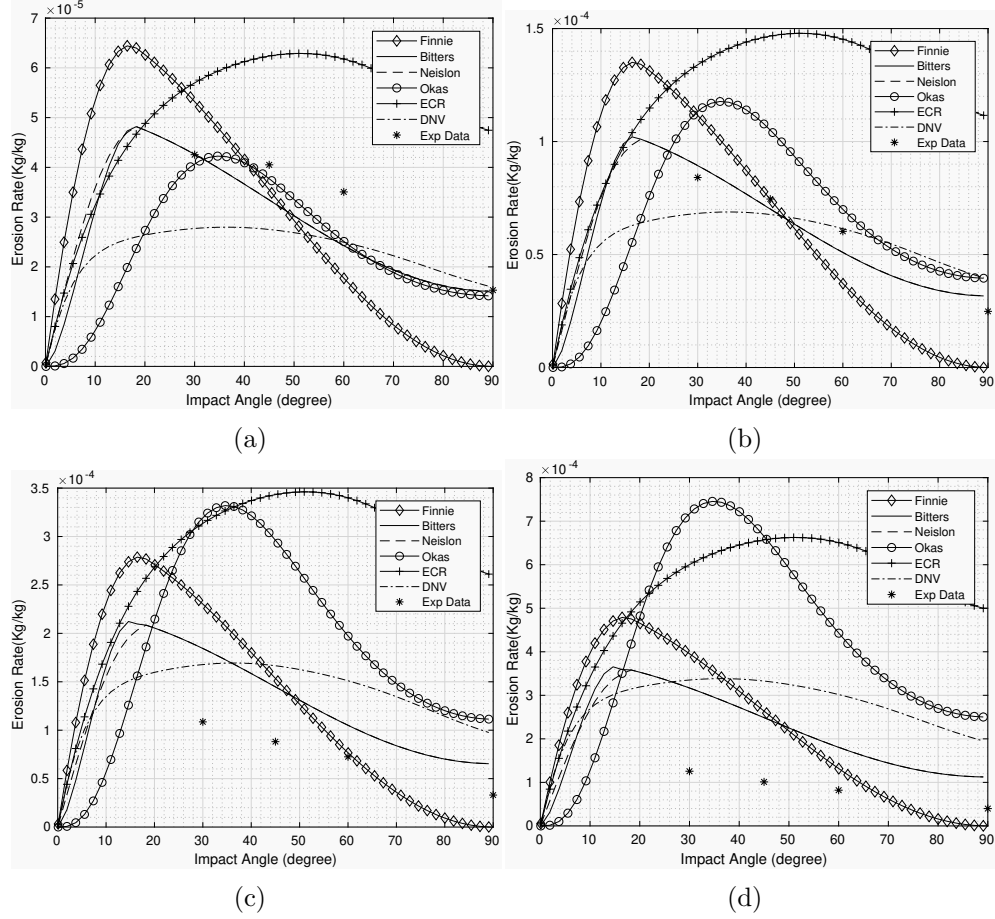


Figure 4.18: Erosion rate vs Impact Angle (AISI 1018), a) at particle velocity of 36m/s , b) at particle velocity of 47m/s , c) at particle velocity of 63m/s , d) at particle velocity of 81m/s , experimental data reported by Islam et al. [22]

For Finnie's, DNV and E/CRC erosion models, constants reported by the authors are listed in table 4.3. For Neilson's and Bitters model, cutting and deformation factors are evaluated from experimental data at a particle velocity of 36m/s . By looking at erosion rate prediction results for other velocities, this deformation and cutting factors need to be modified for different velocities. Similarly, Oka's erosion model predicts erosion rate well at 90° impact angle for particle velocity of 36m/s but overpredicts erosion rate at 90° impact angle for all the other particle velocities.

Oka's model constants used (see table 4.3) for results in figure 4.19a are

reported by Oka et al. [19][20]. Figures 4.19a and 4.19b shows the predicted erosion rate at 90° impact angle for different particle velocities. Figure 4.19a shows that using standard (reported) model constant, Oka's erosion model overpredicts erosion rate for an increase in velocity. These constants (standard) reported by Oka et al. [19][20] are evaluated from the experimental data for specific particle and target materials. Using MATLAB curve fitting tool, these model constant for Oka's model are evaluated for the current test case. Similar approach was used by Duarte et al. [146, 147] for evaluating Oka's model constants in their numerical study. By using a curve fitting tool and using experimental data [22] new evaluated Oka's model constants are as given in table 4.4

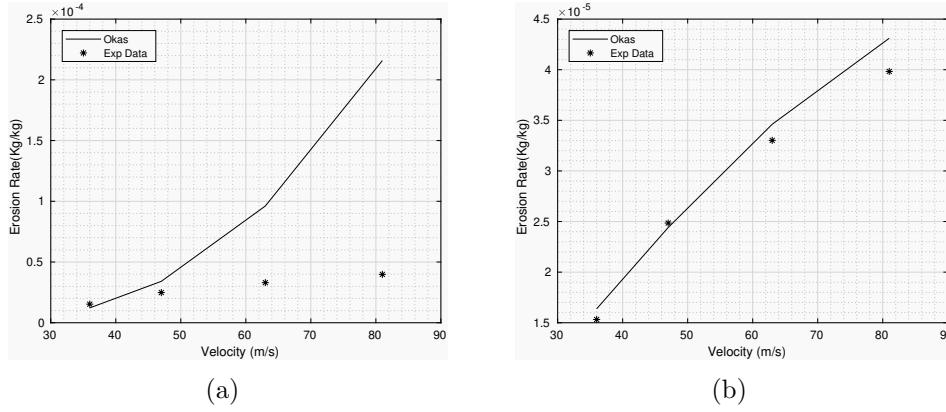


Figure 4.19: Erosion rate vs particle velocity at 90° impact angle for AISI 1018 test case, a) standard constant reported by Oka et al. [19], Oka and Yoshida [20], b) modified constants for Oka's erosion model evaluated from the experimental data reported by Islam et al. [22]

Table 4.4: Modified constants for Oka's erosion model evaluated for AISI 1018 test case

Symbol	Parameter	Unit	Value
K_P	Model Constant	-	5
H_V	Vicker's Hardness	GPa	1.29
k_1	Model constant	-	-0.05
k_2	Model constant	-	0.72
k_3	Model constant	-	0.19
V'_p	Reference velocity of particle	m/s	104
d'_p	Reference diameter of particle	$microns$	326
n_1	Model constant	-	3
n_2	Model constant	-	6.29

Figure 4.19b shows erosion rate predicted at 90° impact angle for all the particle velocities with modified constants for Oka's erosion model. Erosion rates predicted with modified constant for Oka's model figure 4.19b are found to be

in better agreement with the experimental data than that of results obtained by using standard constants for Oka's model. Using these modified constants (as listed in table 4.4) for Oka's model, erosion rate for all the impact angles and particle velocities is plotted in figure 4.20.

Figure 4.20 shows the variation of the erosion rate with variation in the impact angle and particle velocity predicted with modified constant for Oka's erosion model. Erosion rate predicted by Oka's model is found to be in good agreement with experimental data [22], especially at 90° impact angle. Erosion rate predicted for all other impact angles are found to be in good agreement for particle velocity of 36 m/s . For all the other particle impact velocities, the erosion rate is slightly under predicted.

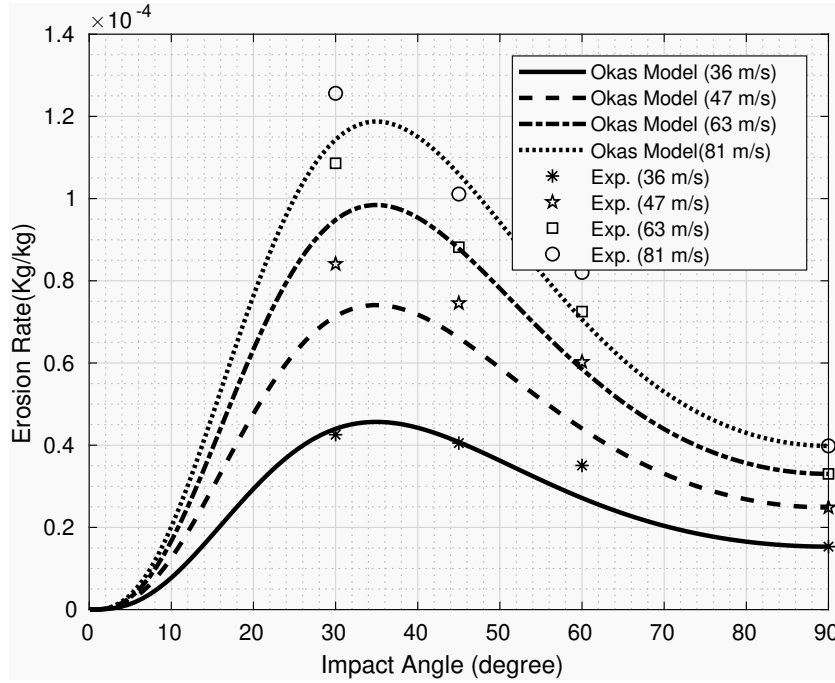


Figure 4.20: Predicted erosion rate vs impact angle (AISI 1018), experimental data reported by Islam et al. [22]

Oka et al. [19] explained that the constants from Oka's angle function n_1 and n_2 are dependent on the target material properties and particle size and shape and these constants are independent of the velocity and size of the particle. In the test case used here target wall material, particle material, particle's size and shape is all the same, and the only velocity of the particle is changed. Angle function if it is independent of particle velocity then it should predict better erosion rate for all the particle impacting velocities. However, by observing under prediction of erosion rate for velocities higher than 36 m/s in figure 4.20, it is emphasised that angle function also depends on particle velocities. A similar inference of angle function dependency on particle velocity was reported by Arabnejad et al. [43].

During the analysis of the air-sand (dry) jet impact test case, it is observed

that among all implemented erosion models, Oka's erosion model predicts the erosion rate in a good margin for all the impacting velocities and impact angles. Finnie's erosion model predicts no erosion for impacting angle near 90° . Bitter's and Neilson's erosion model predicts similar erosion rate for all the impacting velocities. Both models predict better erosion for a particle impact velocity of 36m/s but over predicts the erosion rate for all other particle velocities. To get better erosion prediction by these models, cutting and wear deformation factors need to be modified for respective velocities. For Oka's erosion models calculating accurate erosion for 90° impact angle is crucial. DNV and E/CRC erosion model have given impact angle function in the form of a polynomial, which is not parametric. DNV and E/CRC under or over predicts erosion for all velocities with reported constants. Oka's erosion model with modified constants for the simulated test case predicts better results compare to all other implemented erosion models. Although Oka's model predicts erosion rate better than other implemented erosion models, it has limitations using angle function for different particle velocities. Erosion rate prediction shows that the angle function used in Oka's erosion model, along with target surface, particle material and size and shape of the particle is also found to be dependent on particle velocities.

Further, two more test cases are simulated in order to analyse the dependency of the calculated erosion rate on the selected test case. In the new test cases, experimental conditions and the parameters used for erodent particles are kept the same as the earlier (AISI 1018) test case, and only target wall material is changed. The new test cases are simulated by using target materials API-X70 and API-X100, which are commonly used in the pipeline industry [24].

Figure 4.21 and 4.22 shows erosion rate predicted by using Oka's erosion model for API-x70 and API-x100 steel. For the new simulated test cases, Oka's erosion model predicts better erosion rate compared to all other erosion models implemented in the CFD based erosion solver. Other implemented erosion models showed similar trend in predicted erosion rate as observed with AISI 1018 test case.

Figure 4.21 depicts the erosion rate predicted by the Oka's erosion model for API-X70 steel is found to be in good agreement with experimental data [24] for particle velocity of 36m/s . For all other particle velocities, the erosion rate is found to be over predicting. Similarly, figure 4.22 shows erosion rate predicted by Oka's model for API-X100 steel agrees well with the experimental data[23] at the particle velocity of 36m/s , but erosion rate is slightly overpredicted for all other particle velocities.

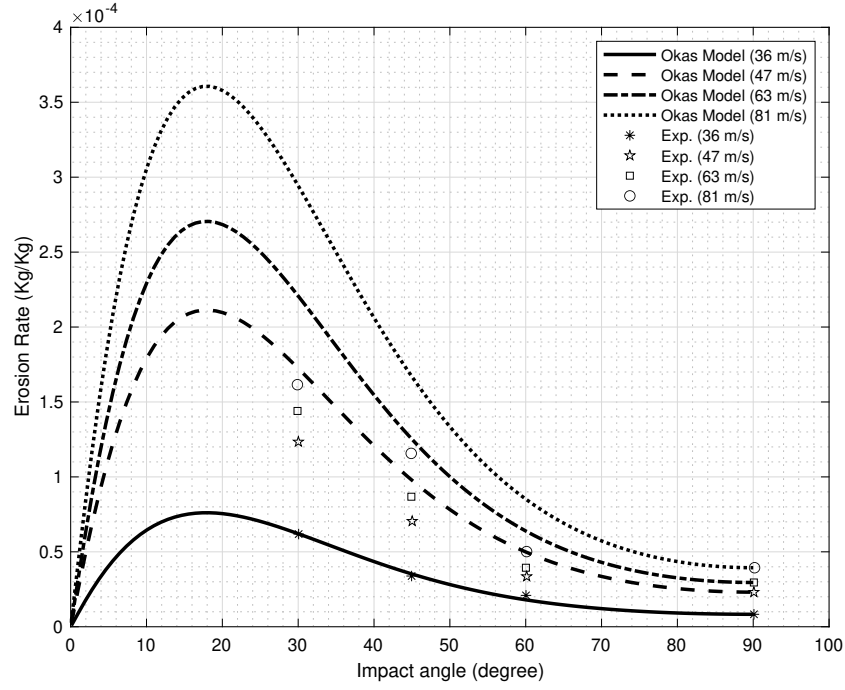


Figure 4.21: Predicted erosion rate vs impact angle (API -X70), experimental data reported by Islam et al. [24]

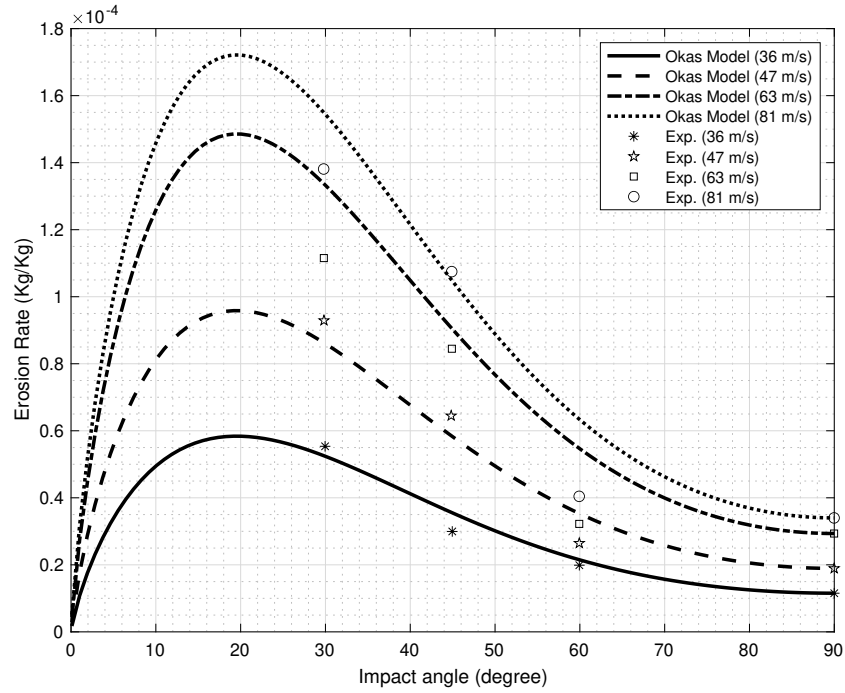


Figure 4.22: Predicted erosion rate vs impact angle (API-X100), experimental data reported by Islam et al. [23]

It is observed that Oka's erosion model predicts better erosion rate compared to all other erosion models for all the predicted erosion rates. Oka's angle function of the erosion model is found to be valid for certain velocities (velocity at which

angle function constants are evaluated from experimental data i.e. $36m/s$ in current test cases). If particle impact velocity is in a wide range, limitations in angle Oka's function is observed, which results in erosion rate over or under prediction.

4.4 Summary

In this chapter, the CFD based erosion solver is validated for its ability to track particles accurately using slurry and dry impact test case. For validation of implemented erosion models, dry impact test cases for different target materials are simulated. It is observed from the erosion rate predicted results that Oka's erosion model predicts better erosion rate compared to all other implemented erosion models. Oka's erosion model predicts better erosion rate at the velocity at which constants of Oka's models are obtained for all impacting angle and for all target materials. For all other particle impacting velocities and angles and for all the target materials, Oka's erosion model over or under predicts the erosion rate.

In the next chapter using experimental data of dry impact test cases from the literature, few observed gaps in erosion prediction rates will be explored such as erosion rate dependency on particle velocities, target material properties etc. A new form of erosion model is proposed, which is used to analyse the effect of different particle velocities on the erosion rate.

Chapter 5

Erosion Model Development and Validation

In the previous chapter, CFD based erosion solver is constructed, and six different erosion models available in the literature are implemented in the CFD based erosion solver. Among such, three erosion models, i.e. Finnie's[13], Neilson's[16] and Bitter's[14, 15] erosion models are theoretically derived, while other three, i.e. Oka's[19, 20], DNV[18, 34] and E/CRC[17] erosion models are based on experimental correlations for specific conditions of experiments performed by the authors respectively. Applicability of these erosion models for fine particles having various feed rate and velocity are already tested in chapter 4. It is observed from simulation results that the implemented erosion models work well under specific given test conditions also some limitations are observed for dynamic test cases (such as for different particle velocities).

In the oil and gas industry, especially the pipelines in the desert of middle east region are exposed to high sand flux causing erosion [10]. In the complex geometries and flow conditions, the particle can hit the target surface at different velocities and impact angles. For such complex cases, it is crucial for erosion models to predict erosion accurately at all particle impact velocities and impact angles which will provide total erosion magnitude and detect the highly susceptible erosion regions. In this chapter, the erosion model has been developed, to predict the erosion rate at a wide range of particle impact velocities and impact angles. Erosion rate predicted by the developed erosion model is then validated against experimental data [10, 22–24] and compared with results predicted by the Oka's erosion model [19, 20].

To develop erosion model experimental data of dry impact erosion test cases reported by Islam and Farhat [10], Islam et al. [22, 23, 24] is used. To develop erosion model first parametric study of experimental data is carried out to analyse the effect of each parameter on the erosion rate. New erosion model is proposed based on these experimental data and previous erosion models reported by Neilson

and Gilchrist [16], Bitter [14], Oka et al. [19], Levin et al. [74] and Zhang et al. [17]. Developed erosion model predicts erosion at steady conditions such as constant velocities and feed rate and also with varying velocities and feed rate.

To develop erosion model experimental data reported by Islam et al. [24],[22], [10, 23] is used. They studied erosion for four different particle impact velocities and impact angles at four different feed rates. They performed dry impact erosion tests using sandblast type erosion tester and reported experimental erosion data for four different material at well-controlled exposure conditions. Sharp angular alumina particle was used in their experiments with the particle size of about 57 μm . They used four different particle velocities in their experiments by keeping a constant feed rate at a constant velocity. In their experiments, they used particle impact velocity of 36m/s, 47m/s, 63m/s and 81m/s. Four different target material were used in experimental dry impact tests, and all the target materials used are also used as pipeline steel. The target materials used in their experimental tests are AISI 1018, AISI 1080, API X70 and API X100 steel and the details of mechanical properties of these materials reported in Islam et al. [24] is given in table 5.1.

Table 5.1: Properties of the target materials used in experiments reported by Islam et al. [24]

Material Properties	AISI 1018	AISI 1080	API X70	API X100
Vickers Hardness (GPa)	1.29	3.03	1.81	2.50
Elongation (%)	20	12	17	18.6
Young's Modulus (GPa)	205	200	203	210
Yield Strength (MPa)	370	585	482	690
Tensile Strength (Mpa)	415	965	570	760
Density(kg/m^3)	7870	7870	7870	7870

In all experimental test cases, they used similar erodent particles. The particles used in experiments is aluminium oxide, and properties of the particle are outlined in table 5.2

Table 5.2: Properties of the erodent particle used in experiments reported by Islam et al. [24]

Particle Properties	
Vickers Hardness (GPa)	27.13
Density(kg/m^3)	3950
Size (μm)	57 \pm 2
Shape	Angular, Sharp
Crystal Phase	Alpha

5.1 Parametric Analysis of Data for Erosion Model Development

Erosion is found to be unsteady during its initial period. This unsteady erosion rate period is known as the incubation period [148]. After this incubation period at constant flow parameters, the erosion rate reaches a steady state. Experimental data sets used here for erosion model development are obtained at time 600 seconds, where it is assumed that erosion rate might have reached a steady state. To confirm the steady-state, erosion rate as a function of time and velocity for API x42 [10] target material is plotted in figure 5.1.

Figure 5.1 presents the erosion rate as a function of time and velocity. Axis Z and Y show erosion rate and velocity, from figure 5.1, it is observed that as velocity increases erosion rate increase. The increase in erosion rate with increasing particle velocity is because as the velocity of particle increases, the kinetic energy of the particle increases, leading to higher erosion rate. Z and X-axis show change in erosion rate with respect to time. The change of erosion rate with time is plotted for particle velocity of 81 m/s. Figure 5.1 shows at initial erosion period, the erosion rate is unsteady and shows incubation period. Between 180 - 400 seconds, the erosion rate is observed to be becoming steady. The new erosion model is developed based on the assumption of a steady-state erosion rate for respective velocity. Therefore the experimental data for 600 s is used in further erosion model development

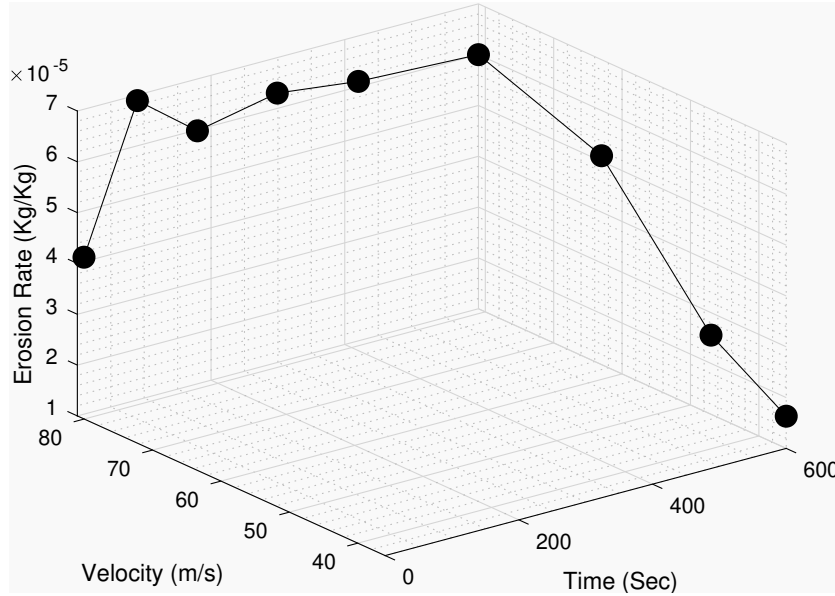


Figure 5.1: Erosion rate plotted as a function of time and velocity for API X42 target material (experimental data reported by Islam and Farhat [10])

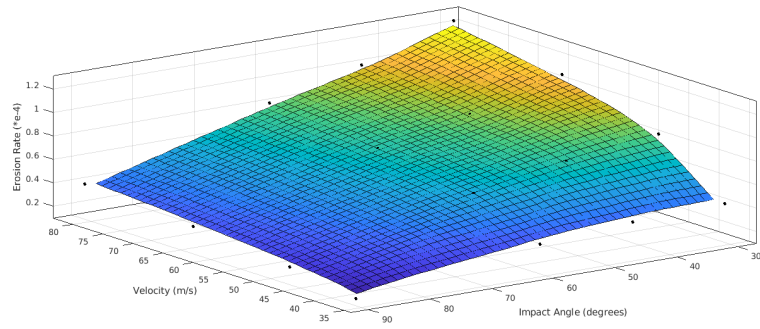
5.1.1 Erosion rate vs impact angle vs impact velocity

Surface response plots are generated from experimental data [10, 22–24] to understand and analyse the effect of particle impact angle and velocity on erosion rate. Surface response plots generated are as shown in figure 5.2

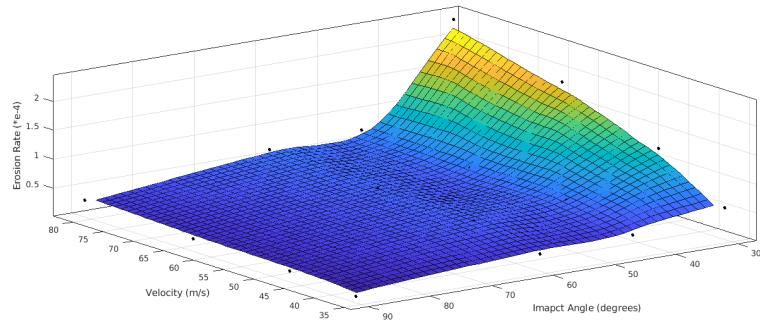
Figures 5.2a, 5.2b, 5.2c and 5.2d show surface response plot of erosion rate with respect to velocity of particle and impact angel of particle for AISI 1018, AISI 1080, API X70 and API X100 materials respectively. All the plots of figure 5.2 show erosion rate increases with an increase in the particle velocities, and the reason for this is attributed to the increase in particle’s kinetic energy. In all the plots, the low erosion rate is observed at high particle impact angle and erosion rate increases with a decrease in particle impact angle.

Many researchers [13, 14, 16, 19] have divided erosion wear according to particle’s vertical and horizontal velocity components. The vertical component of kinetic energy is associated with deformation wear, and the horizontal component is associated with cutting wear. Parsi et al. [1] discussed that wear in a ductile and brittle material is different. In a ductile material, the higher erosion rate is observed at a low angle of impact, as cutting and platelets formation is the most efficient [14, 15]. Hence, here as the impact angle of the particle decreases the horizontal velocity component of the particle becomes dominant and cutting wear increases, subsequently increase in erosion rate with low impact angel. Increase in erosion rate with a decrease in impact angel is observed until a point where the vertical component of particle velocity becomes so low that it will not penetrate particle deep inside for cutting mechanism. Then erosion happens due to ploughing and sliding erosion mechanisms. Arabnejad et al. [149] has also explained that erosion occurs when particle impact velocity is above critical velocity. This critical point is known as threshold velocity below which no erosion takes place, and deformation is elastic in nature.

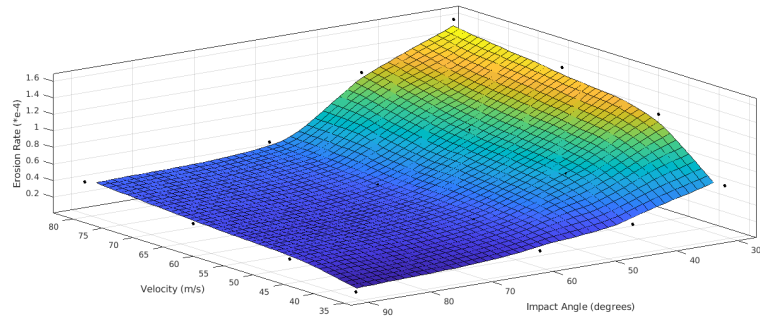
Plots in figure 5.2 show erosion rate for different materials. It is interesting to note that the transition of erosion rate for each different material with velocity and impact angle is non-linear. For AISI 1080 material in figure 5.2b, it can be noticed that erosion rate is comparatively low, up to impact angle of 45° . From impact angle, 45° to 30° sharp rise in erosion rate is observed, and it is maximum at velocity $81m/s$. Erosion rate response to angle and velocity is observed fairly similar for API X70 (figure 5.2c) and API X100 (figure 5.2d) material. For AISI 1018 material (figure 5.2a), comparatively smooth transition of erosion rate is observed with the change in particle velocity and impact angle. Despite using the same particle material, size and flow conditions in all test cases, different erosion rate and transition of erosion rate with particle impact angle and velocity are observed. The difference in erosion rate observed may be due to the difference in the target material properties.



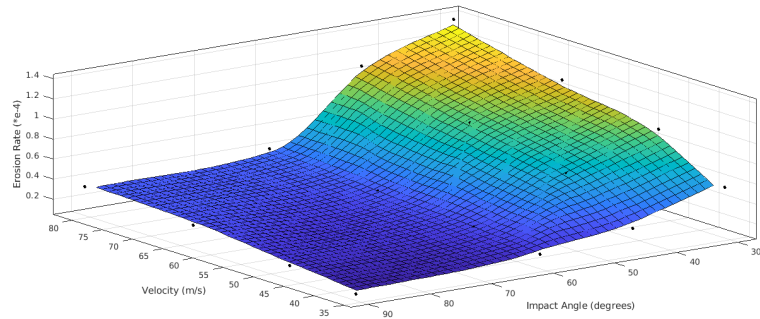
(a) AISI 1018 steel



(b) AISI 1080 steel



(c) API X70 steel



(d) API X100 steel

Figure 5.2: Erosion Rate as a function of Impact Angle and Velocity for a) AISI 1018 steel [22] b) AISI 1080 steel [22] c) API X70 steel [24] and d) API X100 steel [23]

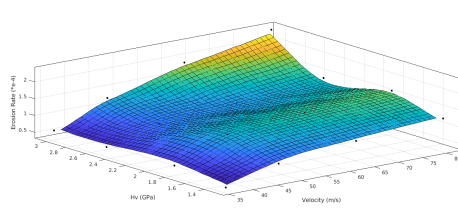
Effect of the material properties on erosion rate is studied extensively by researches but not yet clearly understood [1]. Many researchers have pointed a few vital material properties such as hardness, ductility and toughness having a significant effect on erosion [10]. Hardness can be defined as the ability of the material to resist deformation, abrasion or penetration [150, 151]. Ductility can be defined as the ability of the material to suffer plastic deformation without fracture [151, 152]. Earlier researchers believed that material with higher hardness is good erosion-resistant material [13, 31, 96]. Later, Levy and Chik [47] pointed from his experimental work that erosion rate could be higher for target material with higher hardness. Levy and Chik [47] reported that ductility also contributes significantly to erosion resistance. They explained that in the ductile material particle's kinetic energy can be distributed on the target surface through plastic deformation resulting in a low erosion rate.

In order to analyse the effect of different material properties such as hardness and ductility, using experimental data reported by Islam et al. [24][10, 22, 23] surface response plot has been created. Figure 5.3, shows surface response plot of erosion rate vs hardness, elongation (ductility) and particle velocity at different angle of impact. Figures 5.3a, 5.3c, 5.3e and 5.3g show erosion rate as function of hardness and velocity at impact angle 30°, 45°, 60° and 90°. Similarly, figures 5.3b, 5.3d, 5.3f and 5.3h show erosion rate as function of elongation (ductility) and velocity at impact angle 30°, 45°, 60° and 90°, respectively. Figure 5.4, shows surface response plot of erosion rate vs hardness and Elongation and impact angle at different particle velocities. Figures 5.4a, 5.4c, 5.4e and 5.4g show erosion rate as function of hardness and impact angle at 36m/s, 47m/s, 63m/s and 81m/s velocities. Similarly figures 5.4b, 5.4d, 5.4f and 5.4h show erosion rate as function of elongation (ductility) and impact angle at 36m/s, 47m/s, 63m/s and 81m/s velocities, respectively.

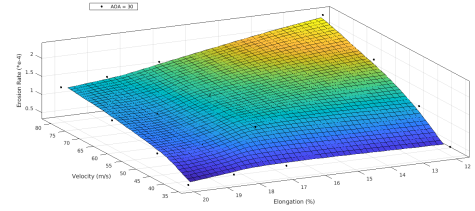
It can be noted from figure 5.3 and figure 5.4 that neither hardness nor elongation (ductility) alone gives an accurate indication of erosion resistance at all particle impact angel as well as at all velocities. Figures 5.3 and 5.4 indicate that the material with higher hardness shows excellent erosion resistance at low particle impact velocity and high impact angle. Similarly, the material with higher ductility shows better erosion resistance at high particle velocity and at low impact angle. Among all materials, AISI-1018 is the most ductile material and least in hardness while AISI-1080 is the hardest material and least ductile material among all. API-X70 and API-X100 are both ductile as well as a hard material.

Goretta et al. [153] discussed in their study about the benefits of material ductility and hardness properties in erosion resistance. They mentioned that material with higher hardness could be excellent erosion resistance if it retains sufficient ductility. In figures 5.3 and 5.4, AISI-1080 begin hardest material shows excellent erosion resistance at high impact angle and low velocity but is most

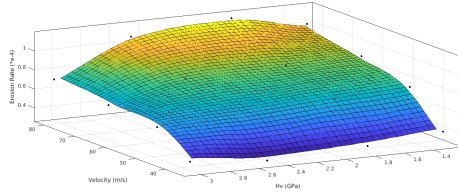
erosion-prone at high impact velocity and low impact angle being least ductile. Similarly, AISI-1018 being the least hard shows more erosion rate at low velocity and high angle of impact and being most ductile shows better erosion resistance at high velocity and low impact angle. Goretta et al. [153] revealed that the work hardening is the reason for the ductile materials, which is attributed to the excellent erosion resistance at high particle velocities. API X70 and API X100 having the balanced combination of both hardness and ductility shows overall better erosion resistance among all the materials.



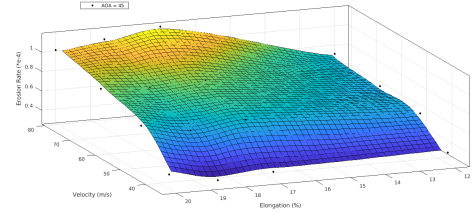
(a) Hardness ($\alpha=30^\circ$)



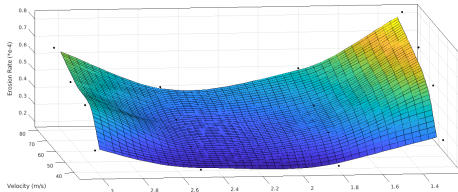
(b) Elongation ($\alpha=30^\circ$)



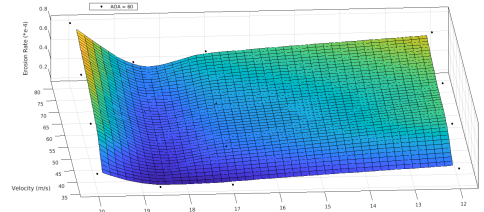
(c) Hardness ($\alpha=45^\circ$)



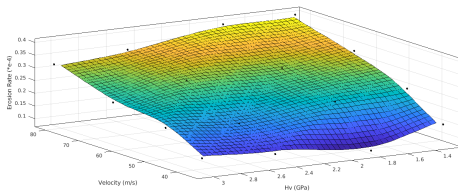
(d) Elongation ($\alpha=45^\circ$)



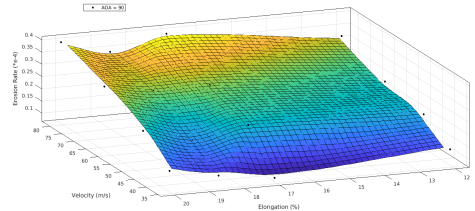
(e) Hardness ($\alpha=60^\circ$)



(f) Elongation ($\alpha=60^\circ$)

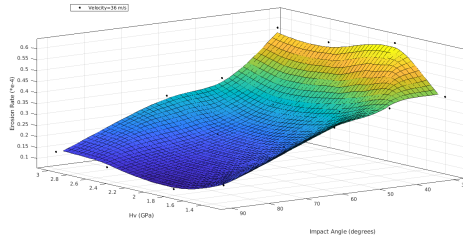


(g) Hardness ($\alpha=90^\circ$)

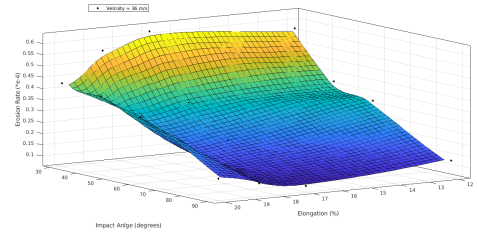


(h) Elongation ($\alpha=90^\circ$)

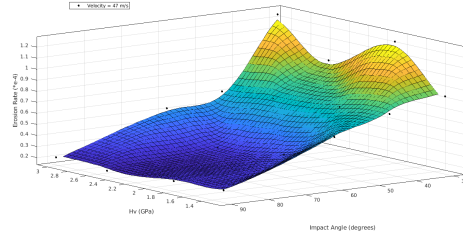
Figure 5.3: Erosion rate as function of hardness, ductility (elongation) and velocity at impact angle 30° , 45° , 60° and 90°



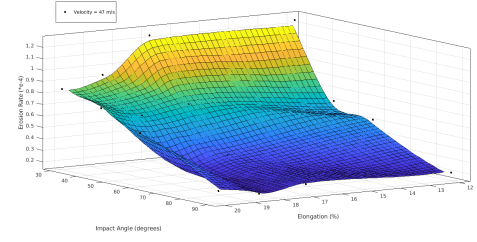
(a) Hardness (36 m/s)



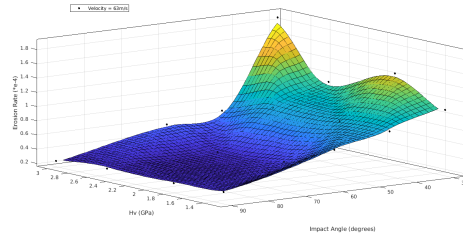
(b) Elongation (36 m/s)



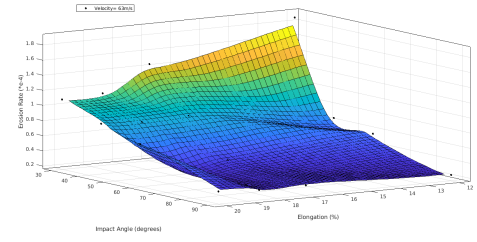
(c) Hardness (47 m/s)



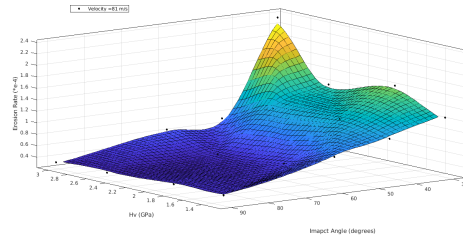
(d) Elongation (47 m/s)



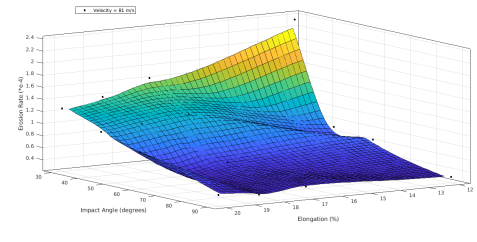
(e) Hardness (63 m/s)



(f) Elongation (63 m/s)



(g) Hardness (81 m/s)



(h) Elongation (81 m/s)

Figure 5.4: Erosion rate as function of hardness, ductility (elongation) and impact angle at 36m/s, 47m/s, 63m/s and 81m/s

By analysing the surface response plots for all the materials, it can be concluded that that the material's erosion resistance ability can not be expressed using a single material property. It is a combination of these material properties which resists erosion at different conditions.

5.2 Development of Erosion Model

Developed Erosion model is semi mechanistic model as it is based on experimental correlations. Developed erosion model is based on ideas reported by Levin et al. [74], Neilson and Gilchrist [16] and Bitter [14, 15] erosion model. In the developed erosion model erosion is calculated at 90° impact angle ' \mathcal{E}_{90} ' and erosion at all particle impact angel is given as product of \mathcal{E}_{90} and angle function $f(\alpha)$ similar concept as used by Oka's, DNV and E/CRC erosion models [17–20]. Total erosion at all impact angle and velocities is given as,

$$\mathcal{E}_\alpha = \mathcal{E}_{90} \cdot f(\alpha) \quad (5.1)$$

As Oka et al. [19],[20] has pointed out, to calculate accurate erosion at all impact angel it is absolutely essential to calculate accurate erosion at 90° impact angle.

5.2.1 Erosion at Normal Impact Angle

Levin et al. [74], divides kinetic energy (KE) of particle into two parts, (KE_{pd}) kinetic energy used for plastic deformation and (KE_{ed}) is kinetic energy used for elastic deformation. Hence, the total kinetic energy of a particle can be written as,

$$KE = \frac{1}{2}m_p V_{pi}^2 = KE_{pd} + KE_{ed} \quad (5.2)$$

where, m_p is mass, and V_{pi} is the initial velocity of the particle. The portion of this initial kinetic energy is transferred to the target material upon impact. Amount of initial kinetic energy transferred to the target material depends upon target material properties such as hardness, ductility, toughness etc. [74]. The initial kinetic energy of the particle upon impact is transferred on the rebound of the particle (KE_{ed}) and plastic deformation (KE_{pd}). Kinetic energy spent on plastic deformation can be given as

$$KE_{pd} = \frac{m_p V_{pi}^2}{2} - \frac{m_p V_{pr}^2}{2} = \frac{m_p V_{pi}^2}{2} \left[1 - \left(\frac{V_{pr}}{V_{pi}} \right)^2 \right] \quad (5.3)$$

where, V_{pi} is the initial velocity of particle before impact and V_{pr} is rebound velocity of the particle. The ratio of rebound velocity and the initial velocity is also known as the coefficient of restitution [154]. It shows the amount of elastic energy stored in the target surface and particle. If the coefficient of restitution is maximum, i.e. 1, particle's rebound velocity will be equal to impact velocity. Hence, equation 5.3 will become zero, and the total amount of kinetic energy will be equal to kinetic elastic energy. Coefficient of restitution depends on target and particles mechanical properties.

Johnson [155] expressed coefficient of restitution as a function of elastic modu-

lus and hardness as,

$$e = \left(\frac{V_{pr}}{V_{pi}} \right) = \frac{1.75 \cdot H_V^{5/8} \cdot J^{1/2}}{\rho_p^{1/8} \cdot V_{pi}^{1/4}} \quad (5.4)$$

where, J depends on Poisson's ratio and elastic modulus of particle and target material and is given as,

$$J = \frac{(1 - q_t^2)}{E_t} + \frac{(1 - q_p^2)}{E_p} \quad (5.5)$$

Here, q_t and q_p are Poisson's ratio of target material and particle and E_t and E_p are elastic modulus of target material and particle.

Substituting equation 5.5 and 5.4 in equation 5.3 gives;

$$KE_{pd} = \frac{m_p V_p^2}{2} \cdot \left[1 - \left(\frac{3.06 \cdot H_V^{5/4}}{\rho_p^{1/4} \cdot V_{pi}^{1/2}} \right) \cdot \left(\frac{(1 - q_t^2)}{E_t} + \frac{(1 - q_p^2)}{E_p} \right) \right] \quad (5.6)$$

KE_{pd} gives the available kinetic energy for plastic deformation of the target material. Bitter [14], [15] and Neilson and Gilchrist [16] proposed that total erosion rate at normal impact angle is proportional ratio of available kinetic energy to deformation energy. Where they suggested that the deformation energy is the energy required to remove the unit volume of the target material. Similarly, Levin et al. [74] proposed that the erosion rate is proportional to the ratio of energy available for plastic deformation to the energy required to cause a fracture. Levin et al. [74] related the required energy for unit volume to fracture to the mechanical property of material called tensile toughness. They suggested that this fracture energy required can be estimated from the product of tensile toughness of material and volume of the plastic zone (volume in which plastic deformation is absorbed during erosion).

Erosion model proposed by Levin et al. [74] is given as

$$E_{parameter} = \frac{\frac{m_p V_p^2}{2} \cdot \left[1 - \left(\frac{3.06 \cdot H_V^{5/4}}{\rho_p^{1/4} \cdot V_{pi}^{1/2}} \right) \cdot \left(\frac{(1 - q_t^2)}{E_t} + \frac{(1 - q_p^2)}{E_p} \right) \right]}{TL_{plastic}} \quad (5.7)$$

$$\mathcal{E}_{rate} \propto E_{parameter} \quad (5.8)$$

where, T is tensile toughness of the material and $L_{plastic}$ is plastic-zone size. Levin et al. [74] emphasised that in $E_{parameter}$ even if particle velocity and density are constant for same test conditions, model take into account material with a combination of high hardness to modulus ratio. Also, while calculating kinetic energy, the model not only takes into account the material properties but also the particle properties responsible for plastic and elastic deformation. Tensile

toughness proposed in the model can be estimated from the area under the curve in the true stress-strain curve, but the estimating size of the plastic zone is challenging. Levin et al. [74] has estimated plastic zone size from the surface area of eroded samples and depth of deformed plastic surface beneath the eroded surface by micro-hardness measurement. This procedure of estimating plastic zone size makes it challenging to use the model in the practical engineering test case. Moreover, Levin et al. [74] proposed model can estimate erosion only at normal impact angle.

Here in the new proposed model, kinetic energy available for erosion at normal impact angle is estimated in the same way as in Levin et al. [74] erosion model as it takes a number of target and particle material properties into account. Furthermore, the wear energy concept of Neilson's and Bitter's erosion model is implemented in the newly developed erosion model [14–16]. So in the new proposed erosion model for normal impact angle erosion is given as;

$$\mathcal{E}_{90} = \frac{\frac{m_p V_p^2}{2} \cdot \left[1 - \left(\frac{3.06 \cdot H_V^{5/4}}{\rho_p^{1/4} \cdot V_{pi}^{1/2}} \right) \cdot \left(\frac{(1-q_t^2)}{E_t} + \frac{(1-q_p^2)}{E_p} \right) \right]}{\delta} \quad (5.9)$$

Bitter [14, 15] suggested that the erosion rate is proportional to the ratio of the input kinetic energy to the energy required to remove a unit volume of the target material. Based on this concept, the erosion rate here in equation 5.9 is given by the ratio of the energy used for the plastic deformation to the energy required to remove a unit volume of the target material. In equation 5.9, δ is the wear energy factor, which is the energy required to remove a unit volume of the target material. Wear energy factor depends on the material's mechanical properties, and it varies for different materials. Wear energy factor in equation 5.9, is similar to the fracture energy as explained by Levin et al. [74] in equation 5.7. Levin et al. [74] suggested using tensile toughness of the target material in J/m^3 and plastic zone size to estimate fracture energy. Estimating plastic zone size from the experiment makes it difficult to use this procedure in practice. Nevertheless, wear energy factor can be estimated in the same way as described by Neilson and Gilchrist [16] for deformation energy from experimental erosion data at the normal impact angle. For a given target material using the erosion value from the experimental data at $\alpha = 90^\circ$, the wear energy factor δ can be estimated using equation 5.9. This way of estimating wear energy factor is much more straightforward and practical than that suggested by the Levin et al. [74].

Levin et al. [74] showed from the experimental studies that during the erosion process, mechanical properties of the target material may get evolved. They showed from microhardness test that the target material hardness, due to work hardening changes with erosion. Levin et al. [74], explains that upon particle impact on the target material, the yield strength of the material exceeds locally,

which leads to plastic deformation of material at the vicinity of the impact. The plastically deformed surface layer may get formed at the eroded surface after multiple impacts of particles this increases the yield strength of the target material due to strain hardening. Further deformation due to particle impact will increase the yield strength of a material such that eventually, it will become equal to its fracture strength. At this point, the material becomes so brittle that its fragments may get removed upon any further particle impacts. Similar studies of evolution of target material properties during erosion are also reported by Goretta et al. [153], Divakar et al. [156].

Levin et al. [74] has evaluated the size of the plastic zone in their model from experimental erosion data. Levin et al. [74], in their model used plastic-zone size (L) term as seen in equation 5.7. From the size of plastic zone materials ability to absorb particle impact energy was estimated. Size of this plastic zone depends on multiple parameters such as the material mechanical properties, particle properties, impacting velocity, particle flux rate etc.

In section 2.2.2, we have discussed the relation of particle velocity exponent and erosion rate. In theoretically derived erosion models [13, 14, 16] velocity exponent value is 2 but many authors from experimental correlations have reported this value to vary between 2 and 3 [1, 17, 20]. Some researcher has reported this value below 2 [10]. It cannot be denied that varying velocity exponents with erosion model maybe is related to the fact that the target material properties get evolved in the erosion process. The evolution of the target material properties may change its energy absorbing capacity upon particle impact.

Erosion model by Oka et al. [19] (see equation 2.27) gives velocity exponent ' k_2 ' as a function of target material hardness and particle properties such as size and shape.

$$k_2 = s(Hv)^q \quad (5.10)$$

Here, Hv is Vickers hardness of material and constants s and q depends upon particle properties such as size and shape. In section 4.3.3, Okas's erosion model is used to predict the erosion rate for three different materials (AISI 1018, API X70, API X100) at four different particle velocities and impact angles. Particle material, size and shape used in all the three test cases are the same only target material is changed. Using MATLAB curve fitting tool, the constants s and q are evaluated from the experimental data for all the three test cases; subsequently, k_2 is evaluated for all the three cases by using equation 5.10. If velocity exponent k_2 is dependent only on the target material hardness and particle size and shape, then values of constants s and q should have been the same. As for all the three test cases particles used are of the same size, shape and material. While evaluating k_2 exponent for all three materials, it is found from the results that the velocity

exponent k_2 depends on more factors than just target material hardness and particle size and shape.

As discussed in section 2.3.2, theoretically derived erosion models by Finnie [13], Neilson and Gilchrist [16] and Bitter [14] have velocity exponent value 2. In section 4.3.3 Neilson's erosion model is used to predict the erosion rate using velocity exponent of 2 and deformation and cutting wear factors which are estimated from experimental data at the particle velocity of $36m/s$. In section 4.3.3, results showed that the Neilson's erosion model overpredicted the erosion rate for all other velocities than $36m/s$. These observations in the results show that either velocity exponent is not 2 or cutting and deformation wear factors changes with the change in particle velocities.

In the proposed erosion equation 5.9, δ is the wear energy factor, and the velocity exponent is 2. Estimating wear energy factor from the target material and particle properties have been attempted. Due to lack of sufficient experimental data for similar test cases, at this point, it is unable to include material and particle properties in the wear energy factor. Nevertheless, the wear energy factor can be estimated the same way as suggested by Neilson and Gilchrist [16] to estimate deformation wear energy. Wear energy can be estimated for all the particle velocities from experimental data for 90° impact angle. This wear energy (energy required to remove a unit volume of material) can be estimated at all particle velocities from the experimental data. The estimated wear energy for all particle velocities can be written as a function of velocity and some constants and is given as,

$$\delta \propto C \cdot \left(\frac{V_p}{V'_p} \right)^n \quad (5.11)$$

where, C is the wear energy evaluated from the experimental data at some reference velocity V'_p . Exponent n defines the amount of energy material can absorb, and it depends on several parameters. Value of n can be evaluated from wear energies evaluated from experimental data at different velocities. In equation 5.11, unlike constant cutting and deformation wear factors used in Neilson's and Bitter's erosion model, wear energy δ here evolves with the change in particle velocities.

To analyse erosion rate at 90° impact angle for AISI-1018 material, three different experimental data sets were used, reported by Islam et al. [22], Arabnejad et al. [43] and Okonkwo et al. [157]. All three experimental data sets are from dry impact test on AISI-1018 target material. Islam et al. [22] and Okonkwo et al. [157] used alumina particles as erodent of $57\mu m$ and $50\mu m$ respectively in their experiments while, Arabnejad et al. [43] used sand particle of $150\mu m$ in their experiments with velocity of particles as $9m/s$, $18m/s$ and $28m/s$ at constant particle feed rate. Arabnejad et al. [43] used particle velocity of $20m/s$, $40m/s$, $60m/s$ and $80m/s$ at constant particle feed rate in all experimental test cases.

Islam et al. [22], used particle velocity of 36m/s , 47m/s , 63m/s and 81m/s with varying particle feed rate at each velocity, respectively.

Using experimental data [22, 43, 157], erosion weight loss in kg with respect to the total available kinetic energy at each test case is depicted in figure 5.5. It is interesting to note that erosion weight loss show nearly linear relationship up to 2000 J of kinetic energy. As kinetic energy increases beyond 2000 J drop in erosion weight loss is observed. If equation 5.9 can be seen in terms of energy balance, in figure 5.5 drop in erosion weight loss with an increase in kinetic energy indicates that wear energy changes with respect to the kinetic energy.

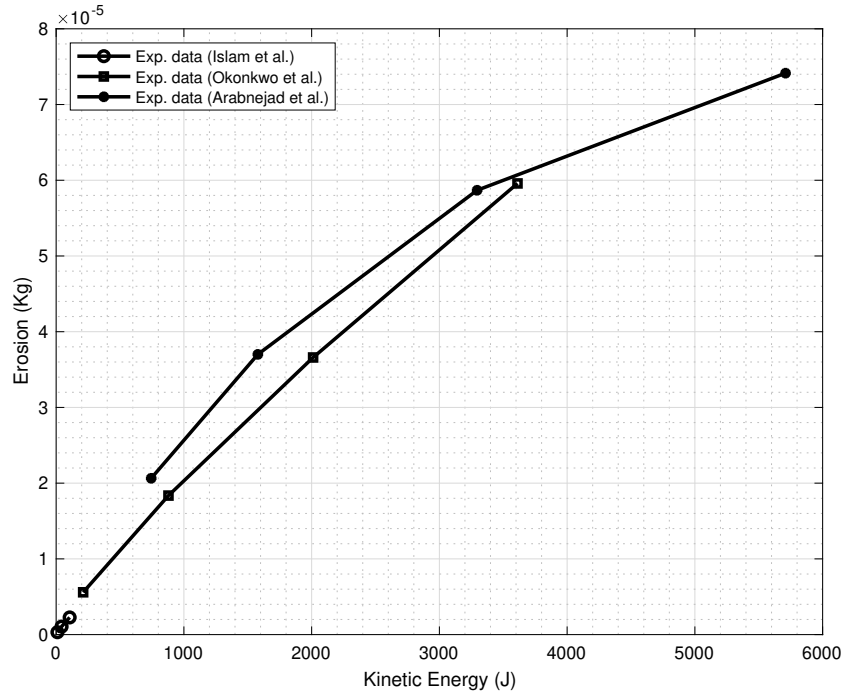


Figure 5.5: Erosion (kg) vs Kinetic Energy (AISI 1018) using experimental data reported by Arabnejad et al. [43], Okonkwo et al. [157] and Islam and Farhat [10]

Kinetic energy is associated with velocity as well as the mass of particles. Arabnejad et al. [43] and Okonkwo et al. [157] used constant feed rate in their experiments but changed particle velocities. In Islam et al. [22] experiment particle velocity is changed along with particle feed rate. Increase in particle feed rate will increase the frequency of particle impact on the target surface. Also, as pointed out by Nguyen et al. [25] increase in particle feed rate may increase interaction between particle-particle. This interaction between particle-particle and also rebounding particle may interact with incoming particles on the target surface and can reduce the kinetic energy of incoming particles. More number of hits by the particles on the target surface may change the rate at which wear energy is changed. It is challenging to quantify how much velocity or feed rate contributes to the change in the wear energy. Also, it is difficult to quantify particle-particle

interaction contribution towards erosion rate. To accommodate this effect of varying particle feed rate in erosion models equation 5.11 is modified by adding particle feed rate term and is given as,

$$\delta \propto C \cdot \left(\frac{V_p}{V'_p} \right)^n \cdot \left(\frac{f_{rate}}{f'_{rate}} \right)^m \quad (5.12)$$

where, f_{rate} is the amount of feed rate and f'_{rate} is reference feed rate at which C is estimated. Exponent 'm' defines the change in wear energy with change in feed rate.

For all the test cases using experimental data [22, 43, 157] and equation 5.9 wear energy δ is calculated for all the velocities and for all the test cases. Using this calculated wear energy δ , equation 5.12 and by regression analysis values of exponent n and m are obtained. As Arabnejad et al. [43] and Okonkwo et al. [157] reported using constant feed rate for all velocities hence equation 5.12 shows analogy with equation 5.11. The value of exponent 'n' for Arabnejad et al. [43] and Okonkwo et al. [157] test case is found to be 0.34. The value of exponents n and m for Islam et al. [22] test case is found to be 1.48 and -0.14 respectively. Using value of constant C as $4.57E - 7J$, estimated value of m and n in function 5.12 and equation 5.9, the erosion rate for all test cases are calculated and plotted in figure 5.6.

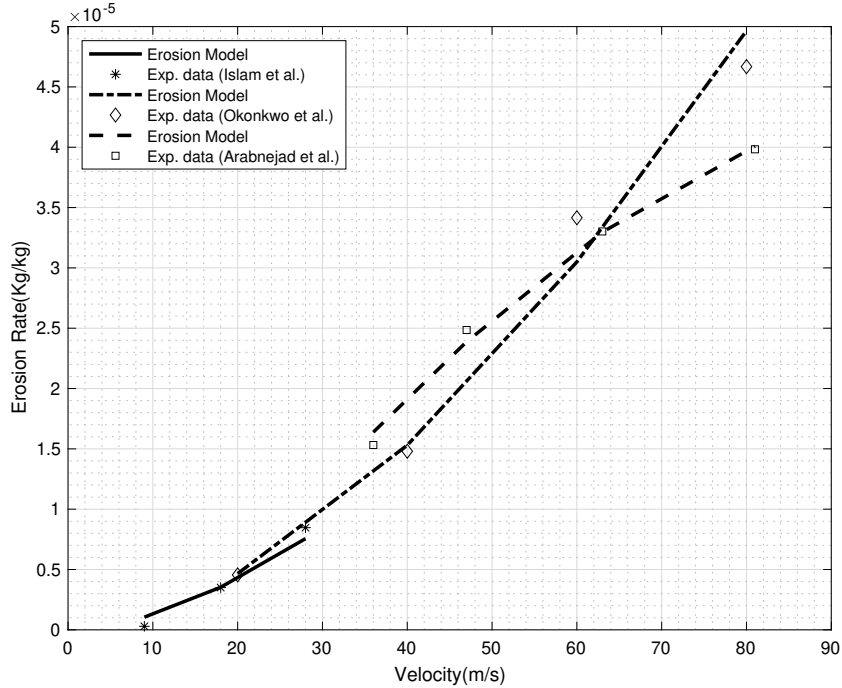


Figure 5.6: Erosion rate predicted by the developed erosion model at 90° impact angle for different particle velocities for AISI 1018 target material compared with experimental data reported by Arabnejad et al. [43], Okonkwo et al. [157] and Islam et al. [22]

Figure 5.6 shows predicted erosion rate using equation 5.9 compared with experimental data [22, 43, 157] for all the velocities. Predicted erosion rate by the developed erosion model (equation 5.9) at normal impact angle agrees well with the experimental data.

5.2.2 Impact Angle Function

In new proposed erosion model, erosion is calculated at normal impact angle using equation 5.9. In Oak's [19, 20] erosion models, erosion is estimated at normal impact angle and using angle function $f(\alpha)$ erosion is calculated at all other impact angles. Similar concept of angle function is used here in new developed erosion model to calculate erosion at different particle impact angles. Different forms of angle functions $f(\alpha)$ can be found proposed by number of researchers and is usually derived from experimental correlations [17, 19, 20, 34, 43] etc.

Angle function given by Zhang et al. [17] version of E/CRC erosion model is in the form of a polynomial of degree 5. Zhang et al. [17] has given values for constant for polynomial. Similarly, in DNV's erosion model [34], angle function is given in the form of a polynomial function of degree 8 and author has given constant values for his angle function. These angle function in the form of polynomial functions work reasonably for specific type and condition of erosion test but have limitations while applying the same for all erosion test cases and conditions. This limitation is because as discussed in section 4.3.3 erosion rate at different angles changes with change in velocities. Using the polynomial form of angle function keeps the shape of angle function same for all the velocities.

Oka et al. [19] erosion model gives angle function in the form of a trigonometric function, and it uses material and particle properties such as hardness of the material, particle size and shape.

$$f(\alpha) = (\sin \alpha)^{n_1} (1 + H_V (1 - \sin \alpha))^{n_2} \quad (5.13)$$

The first term in Oka's angle function 5.13 represent deformation wear and is dominant at higher impact angle of particle. The second term, shows cutting wear and is dominant at a shallow impact angle of particle. Oka's angle function 5.13, requires two constants n_1 and n_2 . Oka and Yoshida [20] has expressed these constants in terms of the initial material hardness and some constants.

$$n_1, n_2 = s(H_V)^q \quad (5.14)$$

Oka and Yoshida [20] has reported that in equation 5.14, constant s and exponent q are determined only by the type, shape and properties of the particle and not on particle velocity and size of the particle. To validate the Oka's angle function for the given test case, the values of constants s and q are obtained from

experimental data at velocity $36m/s$ and Matlab curve fitting tool. A similar procedure was applied by Malik et al. [158] to obtain these angle function constant from experimental data in their studies. Using these obtained constant Oka's angle function is tested for other test cases where experimental conditions for test case were kept identical, and velocity and feed rate of particles is changed.

Figure 5.7, 5.9 and 5.11 shows erosion rate predicted by Oka's erosion model for AISI-1018, API-x70 and API-x100 steel. Constants n_1 and n_2 are obtained from experimental data at particle velocity of $36m/s$. Erosion rate predicted by Oka's erosion model is compared with experimental data reported by Islam et al. [22][23][24]. For all the materials, erosion rate predicted by Oka's erosion model are in good agreement with experimental data for particle velocity of $36m/s$ and at all impact angle. Ideally, if Oka's model predicts accurate erosion rate at 90° impact angles for all velocity, it should predict accurate enough erosion rate at all impact angle at all velocities. Erosion rate predicted by Oka's erosion model in figure 5.7, 5.9 and 5.11 indicates that angle function is not constant for all velocities. Similar observations about varying angle function with velocities have been reported by Arabnejad et al. [43] based on their experimental and numerical studies. Figure 5.7, 5.9 and 5.11 shows erosion rate predicted by the Oka's erosion model is in good agreement at particle velocity of $36m/s$. However, the erosion rate is overpredicted or underpredicted for all other velocities and for all the materials. Erosion rate for API-X70 for particle velocity of $81m/s$ and at impact angle of 30° over predicts erosion rate of magnitude 6.

Oka and Yoshida [20] while giving the angle function, emphasised that the constants used in angle function, i.e. n_1 and n_2 are dependent only on the target material and particle properties such as size and shape. In all test cases simulated (in section 4.3.3) for all the respective materials (AISI1018, API X70 and API X100) erodent particles used are of the same size, shape and properties. So the value of n_1 and n_2 constants for the respective target material should not change with velocity or feed rate. These values of n_1 and n_2 are obtained from experimental data using the curve fitting tool at the particle velocity of $36m/s$. These obtained constants n_1 and n_2 are used in Oka's erosion model to predict erosion rate at all other velocities. Overprediction or underprediction of the erosion rate for different velocities for respective material suggests that particle velocity has influences on angle function. Hence it is essential to add the effect of velocity in angle function in order to predict the erosion rate accurately at all the impact angles and impact velocities.

For new developed erosion model proposed angle function is given as

$$f(\alpha) = (\sin \alpha)^{n_1} (1 + b(\cos(\alpha))^{n_2}) \quad (5.15)$$

Proposed angle function 5.15 is based on idea similar to Oka et al. [19] angle

function. The first term in the proposed angle function represents deformation wear, and the second term represents cutting wear. Constants n_1 , n_2 and b can be obtained from experimental data using the curve-fitting tool for all velocities. Constant n_1 , n_2 and b depends on target material, erodent particle properties and flow condition such as velocity. We tried to analyse experimental data for several materials and correlate material and particle properties to these constants n_1 , n_2 and b obtained from experimental data. Due to lack of sufficient experimental data, at this point, it is unable to express these constants in terms of material or particle properties. Although, these constants can be obtained from experimental data for given target material and particle at respective velocity. The way wear energy is represented in terms of velocity in equation 5.11 similarly, these constants can be expressed as a function of velocity as,

$$n_1 \propto n_1 \cdot \left(\frac{V_p}{V'_p} \right)^n \quad (5.16)$$

Similarly, functions for n_2 and b can be written for varying particle velocities. Value of exponent 'n' in equation 5.16 defines variation of n_1 with respect to velocity. Value of 'n' can be estimated from values of n_1 at respective velocities by curve fitting.

New proposed erosion model consist of equation 5.9 to predict erosion at 90° impact angle and equation 5.15 to predict erosion at all other impact angles. The final form of the new proposed erosion model is written as,

$$\mathcal{E}_{90} = \frac{\frac{m_p V_p^2}{2} \cdot \left[1 - \left(\frac{3.06 \cdot H_V^{5/4}}{\rho_p^{1/4} \cdot V_{pi}^{1/2}} \right) \cdot \left(\frac{(1-q_t^2)}{E_t} + \frac{(1-q_p^2)}{E_p} \right) \right]}{\delta} \quad (5.17)$$

$$f(\alpha) = (\sin \alpha)^{n_1} (1 + b(\cos(\alpha))^{n_2}) \quad (5.18)$$

$$\mathcal{E}_\alpha = \mathcal{E}_{90} \cdot f(\alpha) \quad (5.19)$$

In the new proposed erosion equation, constant δ , C and exponent n_1 and n_2 needs to estimated from experimental data of the impact test case. The accuracy of the new proposed erosion model also depends on the number of experimental data points available. Other parameters required for the newly proposed erosion model can be obtained from the experimental test condition (such as target material and particle properties). As the constants and exponents required for the erosion model are obtained from the experimental impact test case, then the erosion model with these constants and exponent can be used for a different application test case (such as erosion in the pipe elbow, choke valve, etc.) for the same target material and particle. The detailed procedure of estimating erosion model constant and exponents from the experimental data and the application of erosion model for

predicting erosion in the pipe elbow are explained later in chapter 6.

5.3 Validation of Erosion Model

To validate new proposed erosion model (equation 5.19) erosion rate is predicted for AISI-1018, API-X70 and API-X100 steel as target material and alumina as erodent particle for dry impact test. Wear energy factor and angle function constants along with exponents are obtained from experimental data [22–24] with procedure explained earlier in this section. Erosion rate at 90° impact angle is predicted using equation 5.17 and using equation 5.19 erosion rate is predicted at all impact angle angle. Angle function (equation 5.18) is used in equation 5.19. Predicted erosion rate by new proposed erosion model is as plotted in figure 5.8, 5.10 and 5.12 and compared with experimental data reported by Islam et al. [22, 23, 24].

New proposed erosion model takes target material and erodent particles into account. Erosion model takes a variation of the wear energy with the change in particle velocity and feed rate into account. Erosion rate predicted by the new proposed erosion model (equation 5.19) for AISI-1018, API-X70 and API-x100 materials is plotted in figures 5.8, 5.10 and 5.12. Overall erosion rate predicted by proposed erosion model is in good agreement with experimental data. For API-X70 (figure 5.10) and API-X100 (figure 5.12) materials, erosion rate is predicted comparably for the low or intermediate velocities. But erosion rate predicted by the new proposed erosion model is in better agreement with experimental data compared to that predicted by the Oka’s erosion model (figure 5.9 and 5.11).

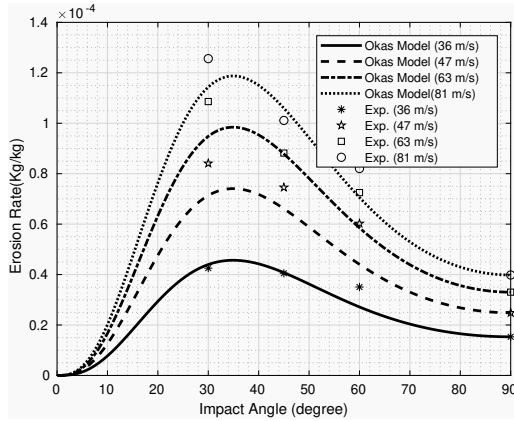


Figure 5.7: Oka's Erosion Model

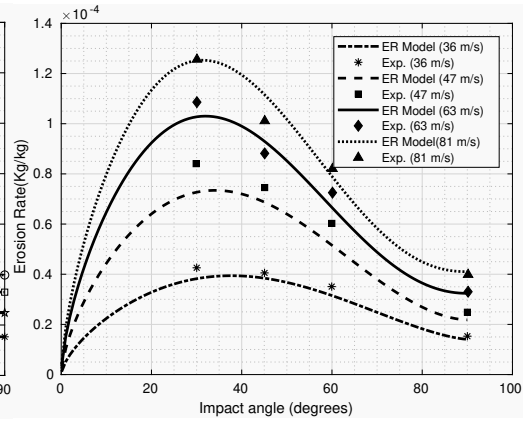


Figure 5.8: New Erosion Model

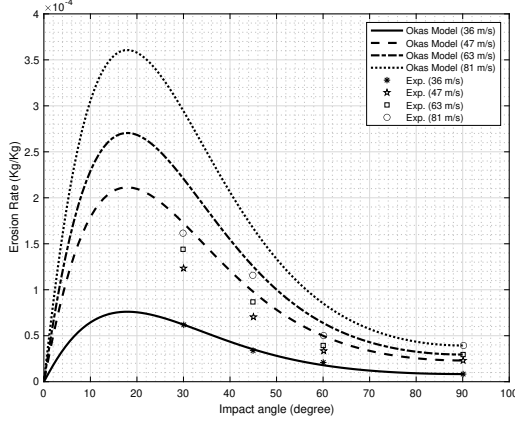


Figure 5.9: Oka's Erosion Model

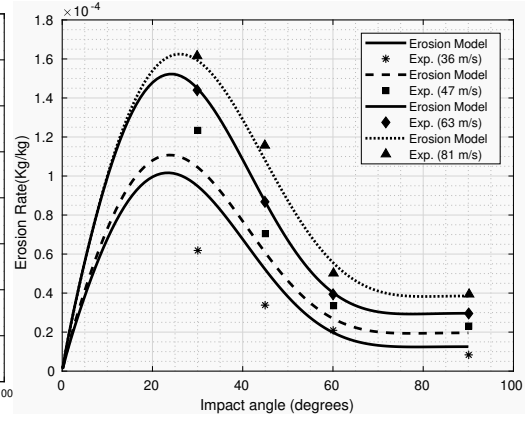


Figure 5.10: New Erosion Model

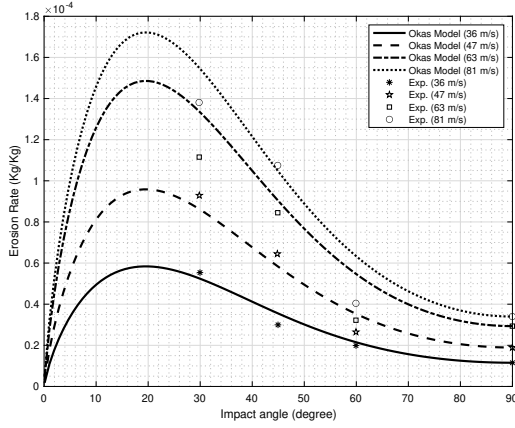


Figure 5.11: Oka's Erosion Model

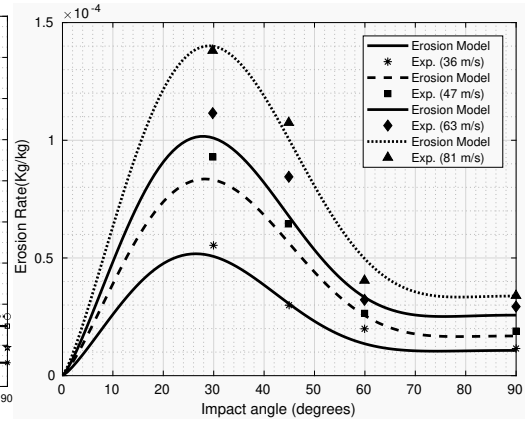


Figure 5.12: New Erosion Model

Table 5.3 summarises the mean absolute percentage error calculated between simulation results and the experimental data for different particle velocities. Error calculated between simulation results using Oka's model is lower at lower particle velocity but it tends to increase with the increase in particle velocity. The newly developed erosion model shows comparatively higher error at lower particle velocity but error decreases with increase in particle velocity. Table 5.4 shows the mean average percentage error calculated between experimental data and simulation results for different target materials. The error value shows that the overall erosion rate predicted by the newly developed erosion model for all the target materials is in better agreement with experimental data compared to the erosion rate predicted by the Oka's erosion model.

Table 5.3: Mean absolute percentage error between erosion rate predicted (using Oka’s and new developed erosion model) and experimental data for different particle velocities.

Model \ Velocity	AISI 1018		API X70		API X100	
	Oka	New	Oka	New	Oka	New
36 (m/s)	3.63%	4.39%	3.89%	16.78%	4.46%	6.13%
47 (m/s)	6.94%	6.17%	15.99%	8.97%	6.30%	4.97%
63 (m/s)	4.34%	2.51%	19.97%	1.07%	11.85%	5.90%
81 (m/s)	3.52%	2.27%	24.41%	2.82%	8.91%	3.97%

Table 5.4: Overall mean absolute percentage error between erosion rate predicted (using Oka’s and new developed erosion model) and experimental data

Material	Oka	New
AISI 1018	9.06%	7.47%
API X70	31.95%	14.60%
API X100	15.35%	10.30 %

5.4 Summary

In this chapter, key erosion influencing parameters were analysed by parametric study for experimental erosion data [22–24, 43, 157] from the literature. Influence of particle velocity, target material properties and particle impact angle on erosion rate has been analysed extensively. Based on experimental erosion data[22–24, 43, 157] and previously proposed erosion models[14–16, 19, 20, 74], a new form of erosion model is proposed in the present study. The proposed erosion model adjust dynamically for particle velocity and feed rate variations. The proposed erosion model has been validated with experimental data for three different material and dry impact test case. Later in chapter 6 proposed erosion model has been tested for an application test case to check its capability and validity along with other erosion models.

Chapter 6

Application of Developed Erosion Model and Solver

In many industrial applications, fluid is transported through the pipelines, which contains solid particles because of which pipelines are susceptible to erosion damage. Such erosion in the elbow is commonly observed in pneumatic and hydraulic transport systems. A test case of 90° elbow is analysed using the developed erosion model (as mentioned in chapter 5) and the CFD based erosion solver (as mentioned in chapter 3). The experimental test case of erosion in 90°elbow with air sand flow by Vieira et al. [112] is chosen as the authors have provided a detailed experimental erosion rate for SS316 steel elbow for various flow conditions. Another reason for choosing this test case is along with elbow test case, as authors have provided detailed erosion rate for dry jet impact test for the same material, which is crucial in determining constant and exponents required for the newly developed erosion model.

In this chapter, firstly parametric study of dry jet impact test has been carried out to obtained constants for erosion models. The procedure explained earlier (in chapter 5) to obtain constants and exponents, for the developed erosion model has been discussed here in detail. Later, using these constants and exponents erosion rate has been predicted for 90° elbow test case with developed erosion model. Erosion predicted by developed erosion model for various test conditions and parameters has also been discussed along with other implemented erosion models.

6.1 Parametric Study of dry impact case

The experimental data of dry impact test used for parametric analysis in the following section is reported by Vieira et al. [112]. Dry impact test case was carried out for SS316 steel using a mixture of air and sand. In all experimental test cases, the nozzle was located at 12.7 mm away from the target specimen(SS316 steel). The particle size of 300 μm was used, and the flow rate of 20g/min was maintained in all test cases. Experiments were carried out for three different particle velocities, and erosion measurement for different impact angles at each velocity was reported. Using this available set of experimental data constants and the exponents required for the newly developed erosion models have been obtained. These obtained erosion models constants and exponents are used later to predict erosion in 90° elbow test case.

In order to estimate the wear energy required for the newly developed erosion model, experimental erosion rate data at 90° impact angle is used. Wear energy required to achieve respective erosion rate at respective impact velocities are calculated using equation 5.17 (from chapter 5). Calculated wear energy at respective velocity is fitted to equation 5.12. As in the experimental test cases, the particle feed rate was kept constant at all the velocities the second term in equation 5.12 turns out to be 1. A Wear energy fit function of velocities (equation 5.12) is as plotted in figure 6.1

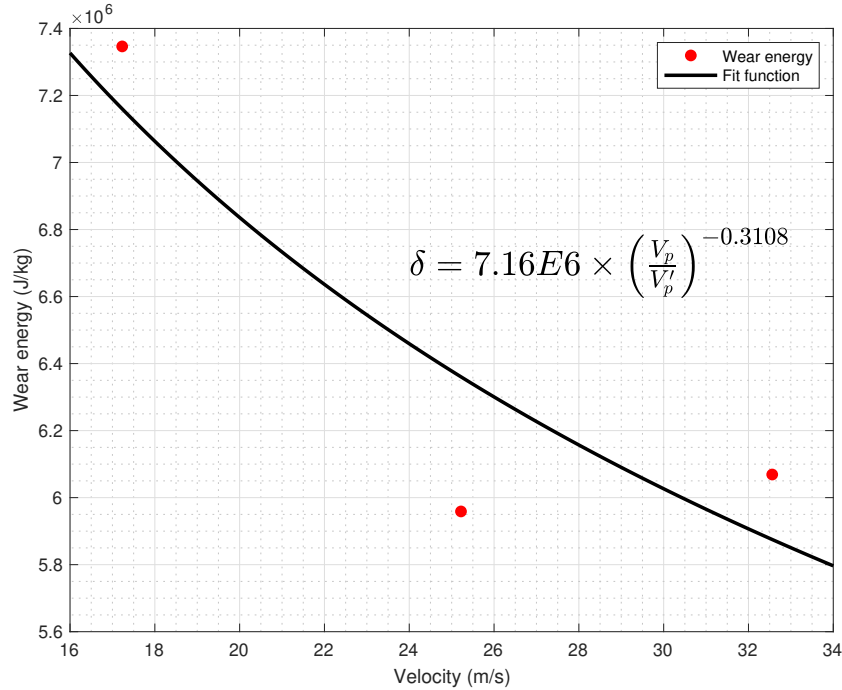


Figure 6.1: Variation of wear energy with particle velocity fitted with function 6.1 for (SS316 Steel)

Wear energy plotted here in figure 6.1, is for three velocities and the value

of exponent 'n' in fit function (for equation 5.12 in chapter 5) obtained is -0.3108. Increasing the range of velocity and experimental data point will increase the accuracy of the wear energy function. Nevertheless, in the present study, experimental erosion data is available for three different velocities which is used to obtain exponent 'n' for the fit function.

Wear energy function using $V_p' = 17.23 \text{ m/s}$ as reference velocity is written as,

$$\delta = 7.16E6 \times (V_p/V_p')^{-0.3108} \quad (6.1)$$

Erosion rate for all velocities are predicted using equation 5.17. Wear function (equation 5.12) with obtained exponent from experiment ($n = -0.3108$) is used in equation 5.17. Erosion rate predicted by proposed model is as shown in figure 6.2. Figure 6.2 illustrates that the erosion rate predicted at 90° impact angle by the proposed erosion model (equation 5.12) found to be in good agreement with experimental data. Hence, the wear energy function (6.1) has been used later, to predict erosion on 90° elbow test case along with obtained wear coefficient and exponent.

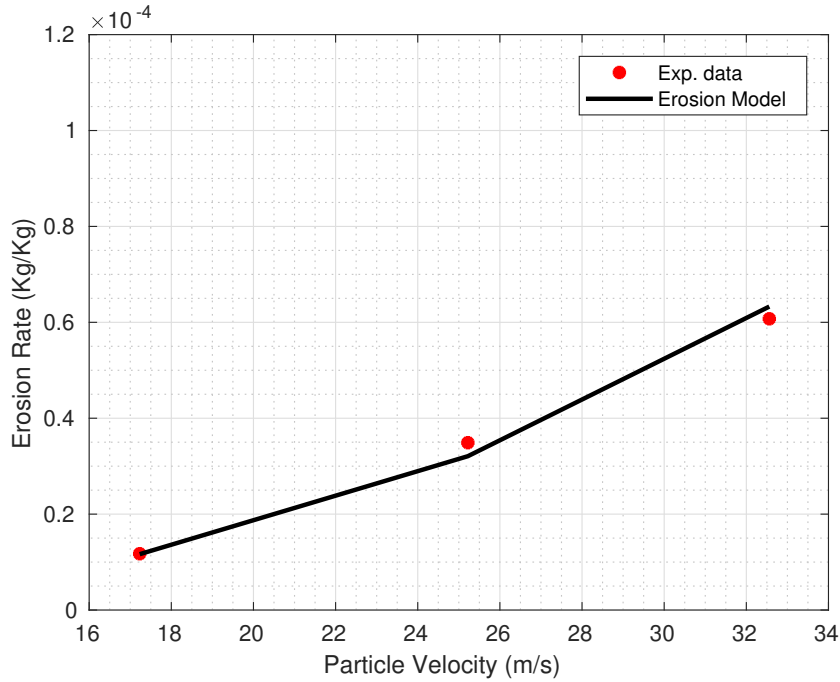


Figure 6.2: Predicted Erosion rate vs Velocity at 90° impact angle (SS316 Steel)

To predict erosion at all impact angles by proposed erosion model equation 5.19 is used. Erosion at 90° impact angle is calculated using equation 5.17. For calculating erosion rate using equation 5.19 at all impact angles, angle function is needed (equation 5.18). In angle function (equation 5.18) values of constants and exponents are obtained using experimental data and MATLAB curve fitting tool. Value of the constant and exponents b and n_1, n_2 are obtained for all the

velocities. Due to limitations of available experimental data for velocities and impact angel n_1 is kept constant and n_2 and b are obtained for all the velocities. The obtained constant b and exponent n_2 are fitted as a function of velocities, similar to the wear energy. Fitting functions used for constant b and exponent n_2 are given as,

$$b = 1.31 \times (V_p/V_p')^{-0.46} \quad (6.2)$$

$$n_2 = 1.98 \times (V_p/V_p')^{0.009} \quad (6.3)$$

where, V_p is particle velocity and V_p' is the reference velocity. The reference velocity used in present study is 17.23m/s . The constant and exponent b and n_2 variation with velocity is fitted with function 6.2 and 6.3 and is illustrated in figure 6.3 and 6.4. Figure 6.3 and 6.4 shows the plots of fit functions (equation 6.2 and 6.3) for different velocities used for the present study.

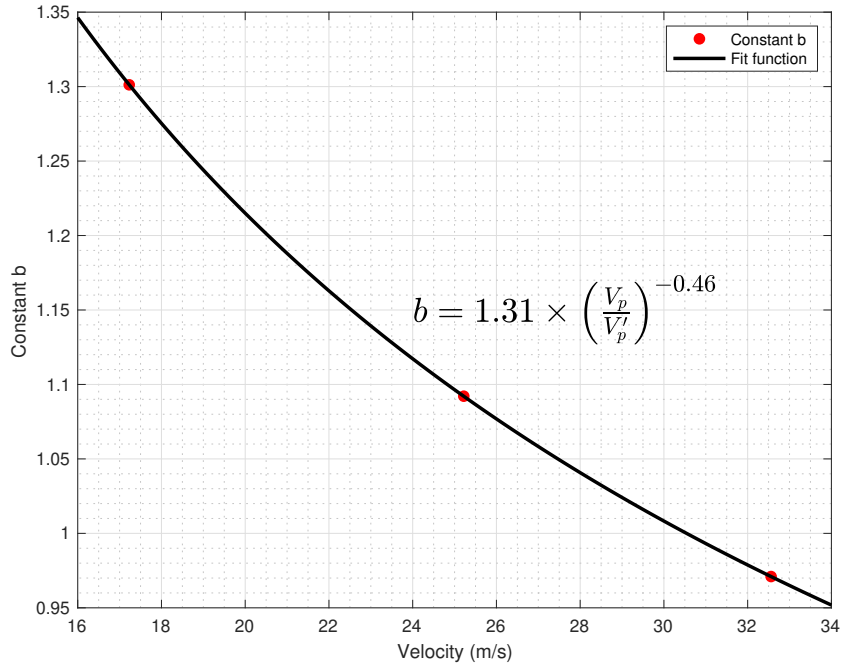


Figure 6.3: Variation of constant b with particle velocity fitted with function 6.2 for (SS316 Steel)

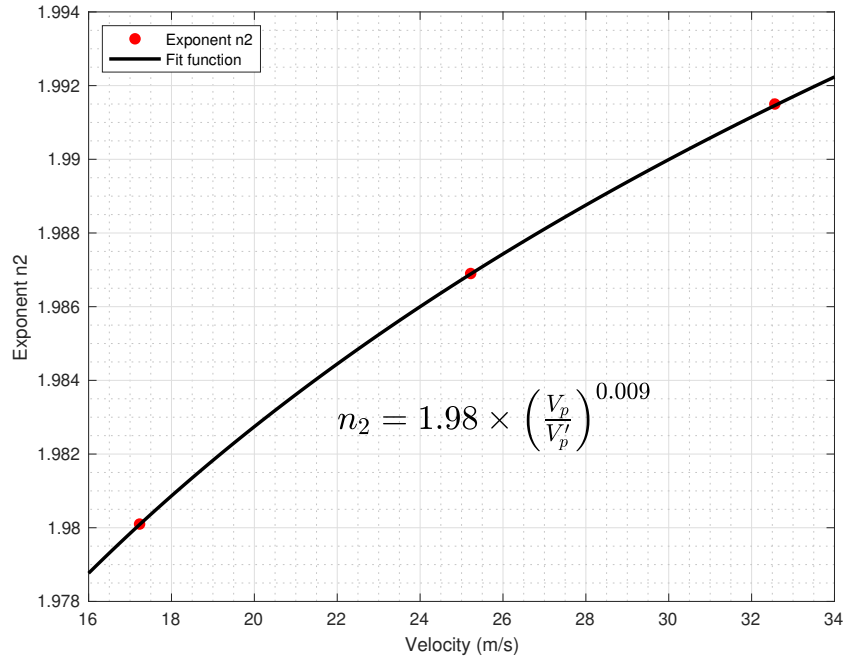


Figure 6.4: Variation of constant n_2 with particle velocity fitted with function 6.3 for (SS316 Steel)

Using these experimental data set and MATLAB curve fitting tool, erosion models exponents and constants were obtained and are summarised in table 6.1.

Table 6.1: Erosion model parameters used in developed erosion model for SS316 steel (marked with \star parameters are estimated from experimental data with the guideline explained in section 6.1)

Symbol	Parameter	Unit	Value
H_V	Hardness	N/m^2	1.83×10^9
ρ_p	Particle density	kg/m^3	2950
q_p	Poisson's ratio of particle	-	0.19
q_t	Poisson's ratio of wall	-	0.26
E_p	Elastic modules of particle	N/m^2	2.05×10^{11}
E_t	Elastic modulus of wall	N/m^2	1.55×10^{11}
δ	Wear energy \star	J/kg	$7.16e6 \times (V_p/V_p')^{-0.3108}$
$n1$	exponent \star	-	0.25
$n2$	exponent \star	-	$1.98 \times (V_p/V_p')^{0.009}$
b	constant \star	-	$1.31 \times (V_p/V_p')^{-0.46}$
V_p'	Reference velocity of particle	m/s	17.23

Erosion rate predicted by proposed erosion model for all velocities and impact angle using obtained constants, exponents material and particle properties as summarised in table 6.1 is plotted in figure 6.5.

Figure 6.5 shows a comparison of predicted erosion rate at different velocity and impact angle. It is depicted from figure 6.5 that the proposed erosion model is in good agreement with the experimental data. These derived erosion models constants and exponents are used later to predict erosion in 90 ° elbow test case.

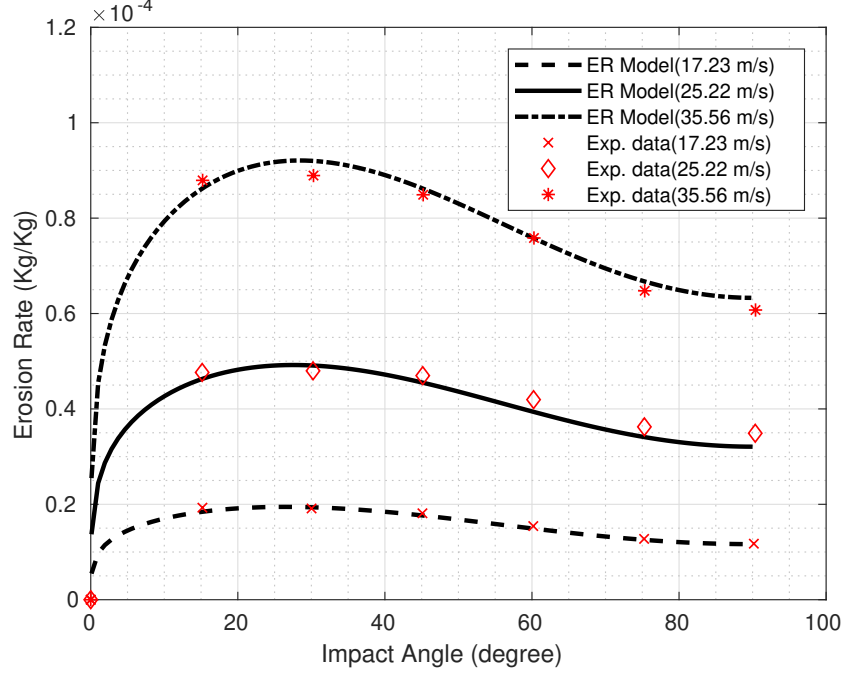


Figure 6.5: Erosion rate predicted by the proposed erosion model vs impact angle (SS316 Steel)

Figure 6.6 shows erosion rate predicted by other erosion models. For Finnie's and Neilson's erosion model plastic stress and deformation and wear rate is calculated from experimental data at particle velocity of 17.23m/s. For DNV and E/CRC erosion model standard constants and exponents are used as given by respective authors (in section 2.3.3). For Oka's erosion model, constants and exponents reported by Oka and Yoshida [20][19] for SiO_2 particle is used.

In figure 6.6, it can be seen that the erosion rate predicted by Neilson's erosion model is in good agreement with the experimental data. Other erosion models (Finnie, DNV, E/CRC and Oka's) over or under predicts erosion at all impact angles. For Finnie's erosion model to estimate plastic flow stress, procedure reported by Finnie [13] is followed. For DNV and E/CRC erosion model, constants used are reported by Veritas [34] and Zhang et al. [17]. Moreover, DNV and E/CRC erosion models give angle function in polynomial form; hence these angle function cannot be modified.

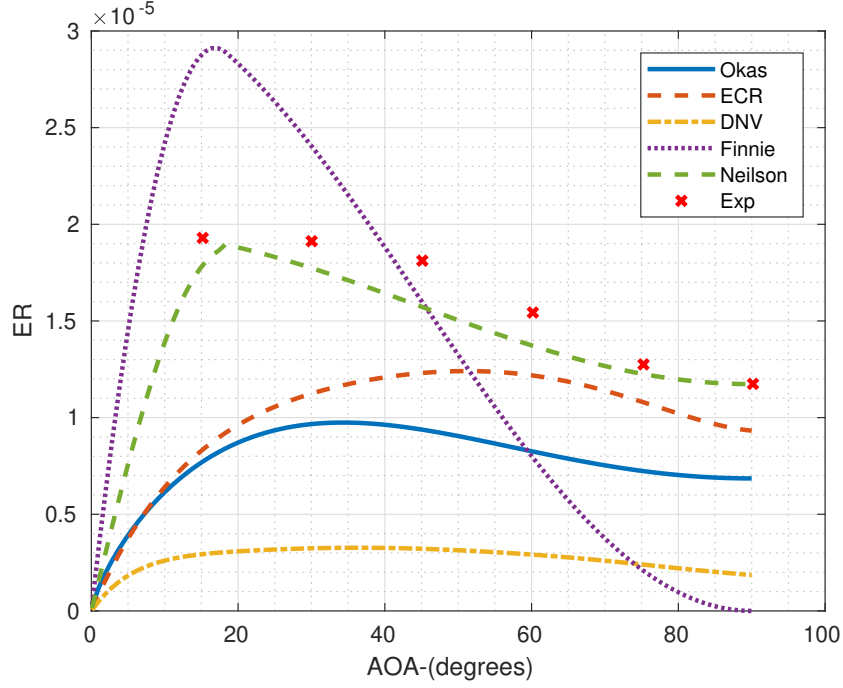


Figure 6.6: Erosion rate predicted by the other erosion models implemented in the CFD based erosion solver vs Angle (SS316 Steel) (Using constants and exponents for Oka's erosion model reported by Oka and Yoshida [20])

While for Okas erosion model, constants and exponents in the erosion model can be obtained from experimental data. These model constants are obtained using the MATLAB tool and experimental data at particle velocity 17.23. Modified constants and exponents for Oka's erosion model are outlined in table 6.2

Table 6.2: Modified constants and exponents for Oka's erosion model evaluated from the experimental data reported by Vieira et al. [112] for SS316 target material

Symbol	Parameter	Unit	Value
K_P	Model Constant	-	110
H_V	Vicker's Hardness	GPa	1.83
k_1	Model constant	-	-0.12
k_2	Model constant	-	$2.3 \times H_V^{0.038}$
k_3	Model constant	-	0.19
V'_P	Reference velocity of particle	m/s	104
D'_p	Reference Diameter of particle	$microns$	326
n_1	Model constant	-	$0.71 \times H_V^{-.59}$
n_2	Model constant	-	$2.4 \times H_V^{-0.94}$

Using the derived model constants erosion rate predicted by Oka's erosion model is plotted in figure 6.7.

Figure 6.7 shows predicted erosion rate by using modified constants and exponents for Oka's erosion models. It is found that the depicted erosion rate

predicted by the Oka's erosion model shows good agreement with the experimental data. These obtained model constants and exponents have been used for Oka's erosion model for predicting erosion in 90° elbow test case.

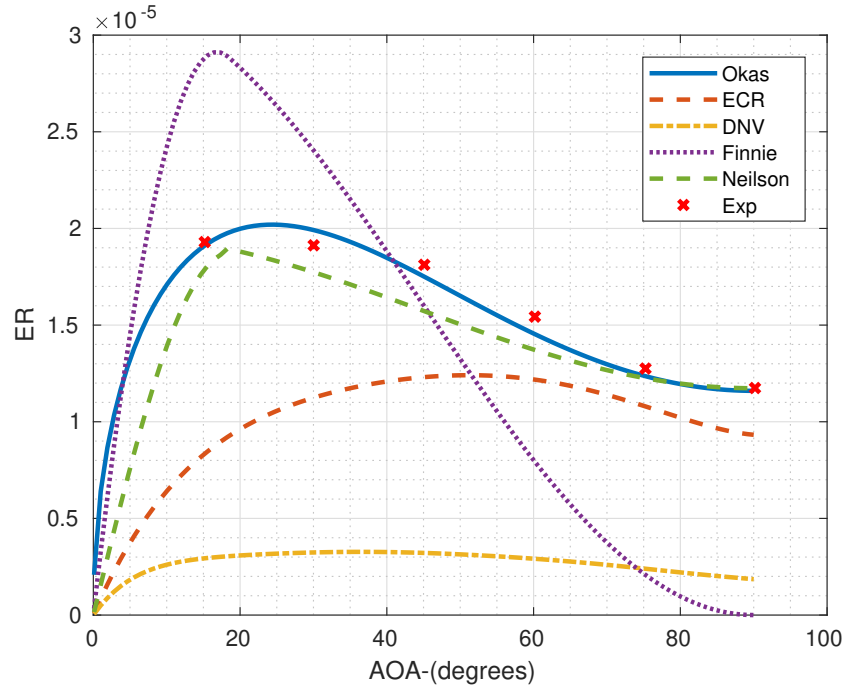


Figure 6.7: Erosion rate predicted by the other erosion models implemented in the CFD based erosion solver vs Angle (SS316 Steel) (Using modified constant and exponents for Oka's erosion model)

6.2 Elbow Test Case

A 90° elbow test case is analysed using developed erosion model in CFD based erosion solver. The numerically predicted erosion rate using CFD based erosion solver for the 90° SS316 elbow case is validated with the experimental data reported by Vieira et al. [112]. In the first part of current section, geometry and meshes created for simulations have been discussed, followed by the mesh independence study and influence of turbulence models on erosion rate. Simulation and solver parameters used for CFD based erosion prediction are discussed briefly. In the later part, number of test cases with different particle velocity, size, feed rate, rebound models etc. and erosion solvers capability to predict erosion rate in these test cases are discussed.

Erosion rate predicted by the erosion models implemented in the CFD based erosion solver is given by mass loss (in kg) by the target material upon unit mass (kg) impact of the particles (i.e. kg/kg). Erosion rate reported by Vieira et al. [112] in experimental data is the thickness lost by the target material (mm) for unit mass (kg) impacting particles (i.e. mm/kg). To predicted erosion rate by the CFD based erosion solver is converted into mm/kg by dividing the predicted erosion rate (kg/kg) by the density of the target material and face area of the computational cell where the erosion is calculated. This gives erosion rate in the form of material lost in mm at the target material per kg impact of the particle, as shown in equation 6.4.

$$\mathcal{E}_{rate} = \frac{\left(\begin{array}{c} \text{Erosion Rate} \\ \text{(kg/kg)} \end{array} \right)}{\left(\begin{array}{c} \text{Density of the} \\ \text{target material (kg/mm}^3\text{)} \end{array} \right) \times \left(\begin{array}{c} \text{Face area of the cell on} \\ \text{the target material (mm}^2\text{)} \end{array} \right)} \quad (6.4)$$

$$\mathcal{E}_{rate} \frac{mm}{kg} = \frac{\begin{array}{c} \text{Thickness lost of} \\ \text{the target material (mm)} \end{array}}{\begin{array}{c} \text{Mass of the} \\ \text{impacting particles (kg)} \end{array}} \quad (6.5)$$

6.2.1 Geometry and Mesh

In the geometry as illustrated in figure 6.8, inner diameter of 90° elbow is 76.2mm and ratio of radius to diameter (r/D) is 1.5. The elbow is connected to the pipe of same inner diameter of 76.2 and 1000mm length upstream and 600mm length in downstream. The reason for choosing the length of the pipe in upstream and downstream is to limit cell count and hence computational cost. The similar inference has been reported by Vieira et al. [112].

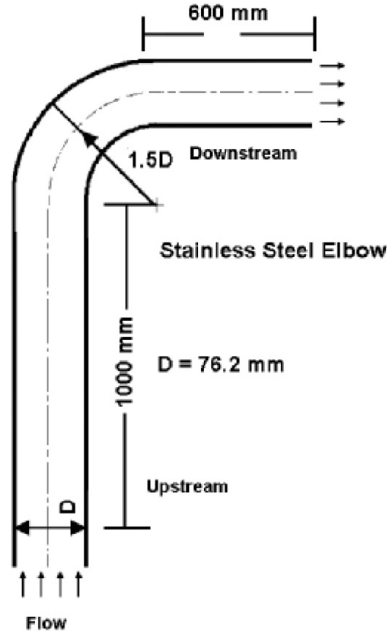


Figure 6.8: Schematic of 90°elbow geometry used for analysis [112]

Geometry and mesh are created using the *blockMesh* utility in OpenFOAM framework. Structured mesh with hexahedral cells is generated to achieve better control of nodes and cells at near-wall vicinity to achieve better alignment of cells and hence better convergence [159]. Mesh is refined near the vicinity of the wall of pipe and elbow to capture the large gradients in the viscous boundary layer. Figure 6.9 and 6.10 show refined mesh regions at the pipe and elbow wall created in *blockMesh* utility.

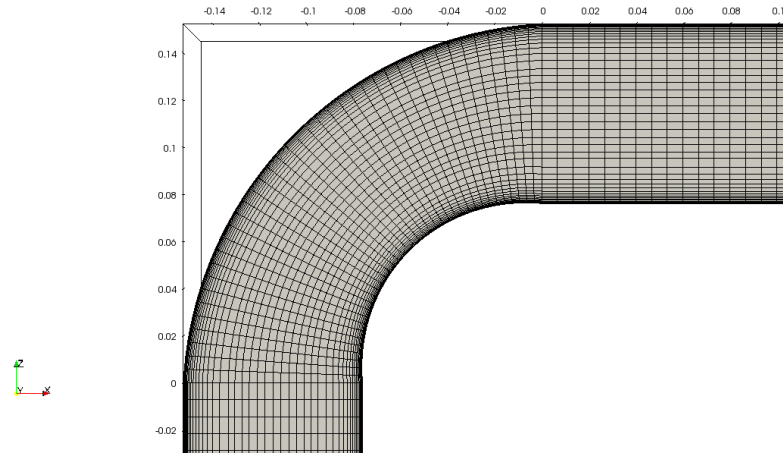


Figure 6.9: Mesh generated for 90°elbow Geometry

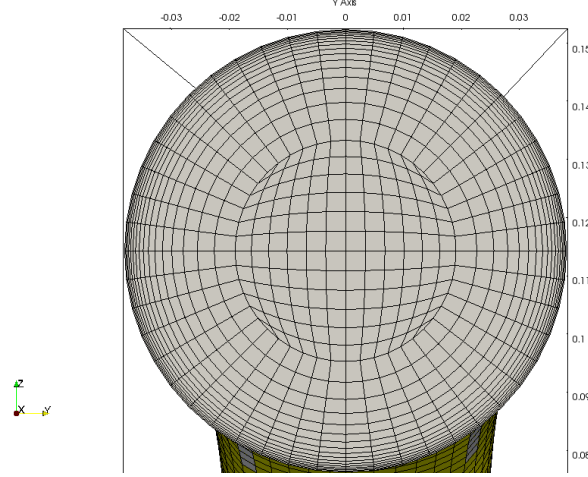


Figure 6.10: Mesh refinement near the wall region of 90°elbow geometry

6.2.2 Simulation and Solver parameters

As shown in schematic 6.8, the flow enters the domain from the inlet at upstream and exits the domain from the outlet at downstream. At the inlet of the domain, the velocity inlet boundary condition is applied. As the wall of pipe and elbow is impenetrable, no-slip boundary condition at the wall is applied. Fixed value pressure boundary condition is applied at the outlet of the domain. In the simulations, air is used as fluid and the value of density and viscosity used are $\rho = 1.2 \text{ kg/m}^3$ and $\mu = 1.8 \times 10^{-5} \text{ kg/m} \cdot \text{s}$. As the average velocity of the fluid at the inlet is ranging from 11 m/s to 27 m/s , flow is expected to be fully turbulent as Reynolds number is above 7×10^5 in all test cases. To evaluate turbulent quantities values of turbulent intensity and hydraulic diameter used at the inlet are 5% and 76.2 mm . In all simulations, the effect of gravitational force is considered with a value of $\mathbf{g} = 9.81 \text{ m/s}^2$, and the direction of gravitational force is applied against upstream part of the elbow (see figure 6.8). For pressure velocity coupling, pimple algorithm is used, and for the non-linear convective term in the momentum equation, second-order accurate linearUpwind scheme is used for discretization.

Particles are tracked here numerically using the Lagrangian approach, and the particles gain momentum from the fluid field. As the feed rate of the particles is low because of which the presence of Lagrangian particles has minimal effect on fluid flow hence one-way coupling of particles and fluid is considered here. Drag force exerted by the fluid on the Lagrangian particles, gravitational force, buoyancy force, pressure gradient force and the added mass force is taken into account. Lagrangian particles are released in the domain through the inlet with the same velocity as fluid as no particle velocity was available in the experimental conditions at this inlet section. As the no-slip condition is assumed between Lagrangian particles and fluid medium, this might be a potential source of error

if any in CFD prediction results.

As lagrangian particles impact wall surface, particles may lose some energy in the form of heat or surface material deformation. This particles energy dissipation is taken into account using the coefficient of restitution. Along with the default particle rebound model in OpenFOAM coefficient of restitution model by Grant and Tabakoff [160] is implemented in current erosion solver. The coefficient of restitution model given by Grant and Tabakoff [160] is written as,

$$e_n = 0.998 - 1.660\theta + 2.11\theta^2 - 0.67\theta^3 \quad (6.6)$$

$$e_t = 0.993 - 1.76\theta + 1.56\theta^2 - 0.49\theta^3 \quad (6.7)$$

where, θ is impact angle of the particle. Coefficient of restitution for normal particle velocity is given by equation 6.6 and equation 6.7 for the tangential particle velocity.

The shape of the particles used as erodent reported in the experimental condition [112] is non-spherical. Hence, in the simulations, drag law given by Haider and Levenspiel [104] is used. This drag law is suitable for non-spherical particle and Haider and Levenspiel [104] gave the coefficient of drag as

$$C_D = \frac{24}{Re} (1 + ARe^B) + \frac{C}{1 + D/Re} \quad (6.8)$$

where, 'Re' is Reynolds number and A, B, C, D are empirical constants. Where these empirical constants are given in polynomial form by Haider and Levenspiel [104] as,

$$A = \exp(2.3288 - 6.4581\phi_s + 2.4486\phi_s^2) \quad (6.9)$$

$$B = 0.0964 + 0.5565\phi_s \quad (6.10)$$

$$C = \exp(4.905 - 13.8944\phi_s + 18.422\phi_s^2 - 10.2599\phi_s^3) \quad (6.11)$$

$$D = \exp(1.4681 - 12.2584\phi_s + 20.7322\phi_s^2 - 15.8855\phi_s^3) \quad (6.12)$$

where, ϕ_s is a spherical coefficient of the particle and is given by $\phi_s = s/S$. The term s is the surface area of a sphere of having the same volume as of particle and S is the actual surface area of the particle. Value of ϕ_s used here is 0.8 assuming particle shape is cubical for the sharp-edged particle [7].

To avoid the influence of the number of particles being simulated on the average impact data of particles, a sufficient number of particles needs to be simulated. Chen et al. [99] and Zhang [35] showed that if the number of particles simulated is above 20,000, erosion predicted in 90° elbow becomes independent of the number of particles simulated. Here, in all the simulation test cases, at least

100,000 particles are simulated. This is to ensure particle impingement data is statistically representative.

Target surface material (90° elbow) is SS316 steel with density of 7879 kg/m^3 and sand particle of $300 \mu\text{m}$ is used same as discussed in section 6.1. Sharp angular sand particles are used with a density of 2650 kg/m^3 . Six different erosion models are implemented in the CFD based erosion solver, including the proposed erosion model in chapter 5. The procedure to obtain constants and exponents required for the erosion models is as explained in section 6.1. Constants and exponents used for the erosion models in the CFD based erosion solver are summarised in table 6.3.

6.2.3 Parameters for Erosion Models

Table 6.3: Erosion Model constants and parameters used for AISI 1018 test case

Erosion Models	Symbols	Parameters	Units	Values
Finnie's Model	P	Plastic flow stress*	kgf/m^2	2.76×10^6
	ψ	Ratio of depth to cut	-	2
	κ	Ratio of vertical to horizontal force	-	2
Neilson's Model	y	Elastic Load Limit*	kgf/m^2	2.06×10^8
	ϕ	Deformation wear factor*	kgf/m^2	1.26×10^7
	χ	Cutting wear factor*	kgf/m^2	7.49×10^6
	q_p	Poisson's ratio of particle*	-	0.19
	q_t	Poisson's ratio of target material*	-	0.26
	E_p	Young's Modulus of particle*	kgf/m^2	1.55×10^{10}
	E_t	Young's Modulus of wall*	kgf/m^2	2.05×10^{10}
	ρ_p	Density of particle*	kg/m^3	2650
	n	Neilson's model constant*	-	4.5
Oka's Model	K_P	Model Constant	-	110
	H_V	Vicker's Hardness*	GPa	1.83
	k_1	Model constant*	-	-0.12
	k_2	Model constant*	-	$2.3 \times H_V^{0.038}$
	k_3	Model constant*	-	0.19
	V'_p	Reference velocity	m/s	104
	d'_p	Reference Diameter	microns	326
	n_1	Model constant*	-	$0.71 \times H_V^{-.59}$
	n_2	Model constant*	-	$2.4 \times H_V^{-0.94}$

E/CRC Model	C	E/CRC model constant	-	2.17×10^{-7}
	BH	Brinelle's Hardness*	BNH	127
	A_1	E/CRC Model constant	-	5.40
	A_2	E/CRC Model constant	-	-10.11
	A_3	E/CRC Model constant	-	10.93
	A_4	E/CRC Model constant	-	-6.33
	A_5	E/CRC Model constant	-	1.42
	n	E/CRC velocity exponent	-	2.41
DNV Model	C	DNV model constant	-	2.9×10^{-9}
	A_1	DNV Model constant	-	9.37
	A_2	DNV Model constant	-	42.30
	A_3	DNV Model constant	-	110.86
	A_4	DNV Model constant	-	175.80
	A_5	DNV Model constant	-	170.14
	A_6	DNV Model constant	-	98.40
	A_7	DNV Model constant	-	31.21
	A_8	DNV Model constant	-	4.17
	n	DNV velocity exponent	-	2.6

Most of these erosion models constants and parameters are default and are as recommended by the respective authors [13–17, 19, 20, 34]. Some of these simulation parameters (marked with \star) are estimated from experimental data with the guideline recommended by the respective authors [13–17, 19, 20, 34] and from experimental conditions.

6.2.4 Mesh Independence Study

To avoid the influence of mesh on fluid flow and subsequently on erosion prediction results, mesh independence study is carried out. For mesh independence study, 90° elbow test case was simulated with fluid and particle inlet velocity of 11 m/s. Five different meshes are generated with an increasing number of cell counts in each mesh for mesh independence study. The number of cells in five different meshes used is outlined in table 6.4. In all the meshes created, $y+ \approx 30$ is maintained, and the κ - ϵ model with standard wall function is used. Similar numerical study on the near-wall modelling approaches on erosion rate prediction using two different sizes of particles (of 25 μm and 300 μm) is carried out by Zhang et al. [139]. They reported that near-wall wall grid spacing approach differs in erosion rate prediction for small and large particles. They suggested small near-wall grid spacing for small particles and large grid spacing for relatively larger particles.

Table 6.4 shows cell counts used in a number of meshes generated along with maximum thickness loss predicted for each mesh. Erosion rate (mm/kg)

is calculated in 90 ° elbow using developed erosion model and the CFD based erosion solver. For mesh Independence study maximum erosion rate predicted by the CFD based erosion solver is tracked. Figure 6.11 shows maximum erosion rate predicted by the developed erosion model and erosion solver on each mesh. Erosion rate shows that increasing resolution of mesh certainly increases the magnitude of maximum erosion rate. Increase in cell count in mesh 4 to mesh 5 did not change the magnitude of predicted erosion rate sufficiently. Hence, mesh 4 with a cell count of around 1 million is used for further analysis as it is less computationally expensive than mesh 5.

Table 6.4: Maximum erosion rate predicted by the developed erosion model and CFD based erosion solver at inlet velocity of $11m/s$ for meshes with different cell count

Mesh	Cell Count	First layer thickness (μm)	Erosion(mm/kg)
1	0.2 million	350	0.001220
2	0.5 million	350	0.001358
3	0.8 million	300	0.001394
4	1.0 million	300	0.001423
5	1.2 million	300	0.001431

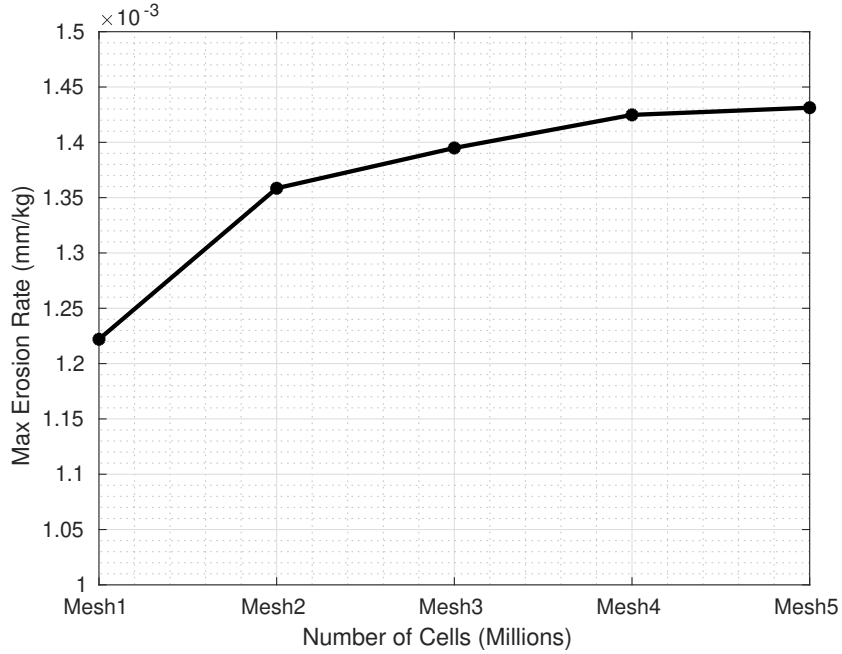


Figure 6.11: Maximum erosion rate predicted by the developed erosion model and the CFD based erosion solver at inlet velocity of $11m/s$ for different mesh sizes

The developed erosion model is analysed for the application test case to investigate the influence of turbulence models, particle rebound models, particle

size distribution function, particle velocities, particle feed rates, particle sizes and elbow orientations on erosion rate. The following subsections describe the details of the mentioned parameters.

6.2.5 Effects of Turbulence Models on Erosion Rate

As Reynolds number of the flow is above 7×10^5 , flow is expected to be fully turbulent. Turbulence modelling is a complicated task, and many different variants of turbulence models are available in the literature and in CFD based erosion solver. No single turbulence model is ideal for simulation test, and different authors have shown different turbulence model best suited for their test cases. Each turbulence model produces different particle eddy interaction resulting in different particle turbulent dispersion and behaviour the near-wall; this leads to predicting different erosion rates [139].

Four different turbulence models are used in the present study to understand the influence of turbulence models on erosion rate predicted by the current solver. While using mesh 4, the κ - ϵ variants of turbulence models with $y+ \approx 30$ and standard wall function is used. For κ - ω turbulence model, mesh size was kept the same as mesh 4, but the spacing of the first cell near the wall is adjusted so to achieve $y+ < 5$. For κ - ϵ variants of turbulence models, `kLowReWallFunction` and `epsilonLowReWallFunction` are used as they are suitable for low and high Reynolds number and conditions for these wall function is based on the position of $y+$ [138]. For κ - ω turbulence model `omegaWallfunction` is used as this wall function is again suitable for low and high Reynolds number and condition is based on the blending of viscous and log layer[138].

Maximum erosion rate predicted by the CFD based erosion solver in 90° elbow is along the centerline on the extrados of the elbow. Figure 6.12 shows erosion rate predicted by different turbulence models along with the centerline on the extrados of the elbow as a function of theta. Figures 6.12 shows erosion rate predicted by the different turbulence models vary insignificantly. All turbulence models predict the maximum erosion rate at around 52° angle on the extrados of the elbow. The k-omega turbulence model usually improves prediction of flow detachment point near the wall in separated flow [110]. In the current test case, as detachment in the flow is not expected, and due to larger particle size and higher Stoke's number, particles may tend to travel in a streamline with less deviation near the erosion hotspot. Hence, the erosion rates predicted by the k-epsilon and k-omega turbulence models are nearly identical. As in the current test case, erosion rate predicted by different turbulence models is nearly identical, a k-epsilon variant of turbulence model is used for further analysis. A similar trend for erosion rates was predicted by Solnordal et al. [110] in their study of erosion using CFD in 90° elbow with different turbulence models. Also, Zhang

et al. [139] observed in their numerical study that the effect of turbulence models on erosion rate is different for small and large particles. They reported that small particles tend to get captured and trapped by turbulence while larger particles are spread uniformly throughout domain because of turbulence.

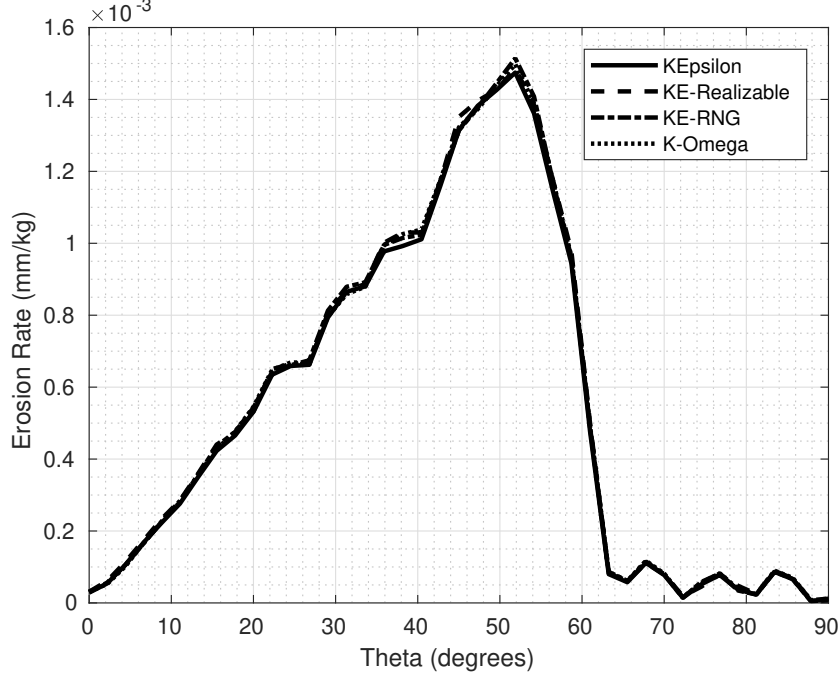


Figure 6.12: Predicted erosion rate by the developed erosion model along the centerline on the extrados of the elbow as a function of angle (θ) while using different turbulence models at inlet velocity of $11m/s$.

6.2.6 Particle Rebound Model

As particles enter the flow domain, it interacts with the fluid surrounding and gains momentum. These particles, when impact the wall surface, lose some energy in the form of heat and deformation of the wall material. The coefficient of restitution termed as amount of energy lost by a particle upon colliding wall surface. If the particle impact is perfectly elastic, i.e. no energy is lost by particle, and frictional force and spin of a particle are ignored, particle upon impact rebounds with the same angle as that of impacting angle. Hence, the coefficient of restitution affects the rebound angle of the particle.

In the current test case, Grant and Tabakoff [160] model calculates the coefficient of restitution as a function of impact angle and is not constant for all particle impact angles. Figure 6.13a and 6.13b shows erosion rate predicted by the CFD based erosion solver using Grant and Tabakoff [160] rebound model and standard rebound model respectively. Maximum erosion rate is predicted for particle and fluid inlet velocity of $15 m/s$. Maximum erosion rate predicted by the CFD based erosion solver using Grant and Tabakoff [160] model is 0.00045

mm/kg, and by using standard rebound model is 0.00122 mm/kg. In comparison, the experimentally [112] reported maximum erosion rate is 0.00026 mm/kg. The magnitude of erosion rate predicted by using the standard rebound model is of order higher than the erosion rate predicted by Grant and Tabakoff [160] model. This difference is because in the standard rebound model coefficient of restitution is constant (i.e. $e = 0.97$) for all the impacting particles and at all the impacting velocities and angles. Due to which particles impacting are concentrated at the hot spot of erosion hence higher magnitude of erosion rate is predicted by the standard rebound model. Moreover, vee-shape erosion scar shape is observed while using the standard rebound model. The similar shape of erosion scar has also been reported by Solnordal et al. [110], suggesting it to be non-physical. Solnordal et al. [110] showed from their numerical and experimental work that observation of such vee-shape erosion scar in 90° elbow was an artefact of the modelling approach and that attributed to particle rebound and the roughness of the wall. Erosion rate predicted using Grant and Tabakoff [160] is in better agreement with experimental data [112] compare to standard rebound model. Erosion scar shape, observed using Grant and Tabakoff [160] is similar to the scar observed experimentally by Solnordal et al. [110] for similar configuration of geometry. As by using Grant and Tabakoff [160] rebound model in present study erosion magnitude and scar shape of erosion is predicted close to experimental data [112] and Solnordal et al. [110] erosion scar shape, Grant and Tabakoff [160] model is used for further analysis.

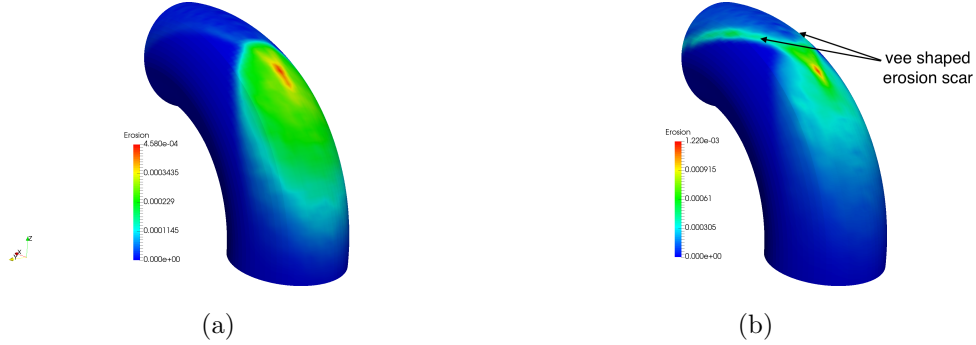


Figure 6.13: Erosion rate predicted by the CFD based erosion solver in 90° elbow at inlet velocity of 15m/s, a) using Grant and Tabakoff [160] rebound model, b) using the standard rebound model

6.2.7 Particle Size Distribution

Predicted erosion rate by the CFD based erosion solver using Grant and Tabakoff [160] model is slightly higher than the experimental data. To analyse the reason behind over prediction of erosion rate by the current solver particle size distribution was studied.

The exact particle size distribution for the current test case was not available

in experimental conditions. Hence, the size distribution function, as discussed in section 4.1.3, is used to analyse the effect of size distribution. Particle size used in size distribution function varies from $25\text{ }\mu\text{m}$ to $700\text{ }\mu\text{m}$ where majority of particle size is around $300\text{ }\mu\text{m}$. Different particle size will have different kinetic energy as well as stokes number. Stoke number defines the degree at which particles are coupled to the fluid flow. As discussed earlier in section 4.1.3 smaller particles tend to bound tightly with surrounding fluid and deviate from the original trajectories. Figure 6.14a shows erosion rate predicted by the CFD based erosion solver with uniform particle size and figure 6.14b shows erosion rate predicted using Rosin-Rammmler particle size distribution function. Figure 6.14b shows that the shape of erosion hot spot changes slightly with using particle size distribution. However, the magnitude of maximum erosion rate predicted did not change much than the erosion rate predicted by the constant size of particles (figure 6.14a).

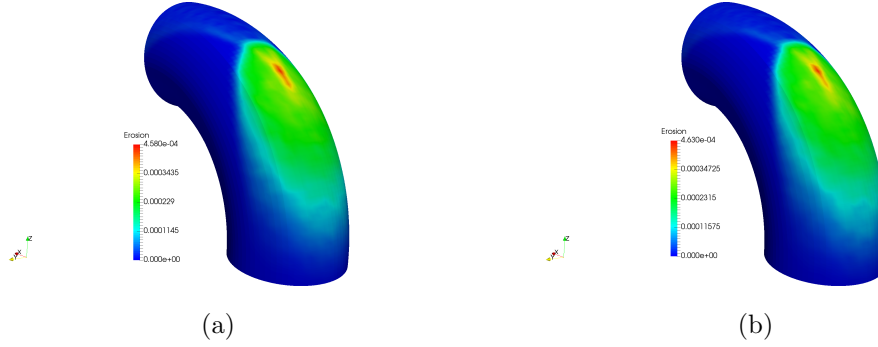


Figure 6.14: Erosion rate predicted by the CFD based erosion solver in 90° elbow at inlet velocity of 15 m/s , a) using constant particle size, b) using Rosin-Rammmler particle size distribution

Another reason for the slight change in predicted erosion rate with particle size distribution is in the current test case, the viscosity of the fluid (air) is lower compare to slurry flow hence relaxation time of particle is much higher. As in the current test case, the viscosity of the fluid (air) is low, and due to high Stokes number, particle inertia dominates the fluid flow path. This particle inertia may be the reason for the observed similarity in predicted erosion rate using particle size distribution function. In figure 6.14b slight over-prediction in the magnitude of erosion rate using particle size distribution is also observed. This is because, while using particle size distribution function, the maximum particle size is around $700\text{ }\mu\text{m}$. The bigger particle possesses more significant kinetic energy and will erode target material more.

6.2.8 Particle Impact Velocity

For four different air velocities, the erosion rate is predicted by the developed erosion model and the CFD based erosion solver. The particle size used in all

the simulations is 300 μm and particle feed rate is changed as according to the experimental conditions. Erosion rate predicted by the developed erosion model for different velocity and feed rate along with experimental erosion rate is outlined in table 6.5.

Table 6.5, shows maximum erosion rate predicted by the developed erosion model, over predicts erosion rate for all test cases. Percentage error calculation of predicted erosion rate and experimental data shows that the developed erosion model over predicts maximum erosion rate than experimental data between 4% to 40%. In all the simulation test cases, particle velocity at the inlet was kept the same as air velocity, as the particle velocity at the inlet of the domain was not available from experimental conditions. In reality, there can be some slip velocity between particle velocity and air velocity. This might be one of the possible sources of error for the developed erosion model for overprediction of maximum erosion rate at high velocities. Also, in section 6.1 when constants and exponents for wear energy were obtained from experimental data, all experimental erosion data was available at constant feed rate. Hence, the last term in equation 5.12, which is related to the feed rate, is not considered here. Changing the particle feed rate can change the number of impacting particles on the target surface. In all simulated test cases with different velocity, the different particle feed rate is used. This varying feed rate might change wear energy, and this can be another possible source of error for the erosion model to overpredict erosion rate.

Table 6.5: Maximum erosion rate predicted by the developed erosion model for different particle velocities and feed rates

V_{air} (m/s)	Feed rate (kg/day)	CFD data (mm/kg)	Exp. data (mm/kg)	Error (%)
11	288	1.68E -04	1.61E -04	4.16
15	192	4.58E -04	2.76E -04	39.73
23	227	1.43E -03	9.71E -04	32.09
27	256	2.02E -03	1.39E -03	31.18

Maximum erosion rate for different velocities is predicted by the developed erosion model as well as other implemented erosion models and are plotted in figure 6.15 along with experimental data. Particle information such as impact angle and velocity used by all implemented erosion models here is the same for the individual test cases. Hence, the difference in predicted erosion rate by different erosion models for the particular test case is associated with the capability of the erosion models.

Figure 6.15 shows maximum erosion rate predicted by different erosion models implemented in the CFD based erosion solver. Most erosion models over-predicts the erosion rate for all particle velocities and Finnie's erosion model over predicts

erosion rate the most among all. DNV and E/CRC erosion models under-predicted erosion rates for all the particle velocities.

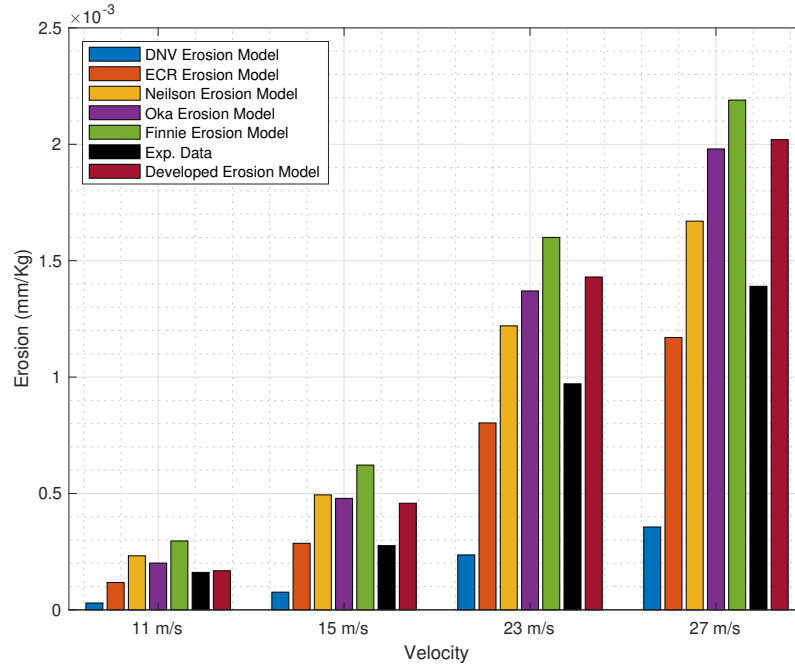


Figure 6.15: Maximum erosion rate predicted by the erosion models at different inlet velocities compared with experimental data reported by Vieira et al. [112]

Figure 6.16 shows percentage relative error calculated for maximum erosion rate predicted against experimental erosion rate for respective velocities. Since the DNV erosion model under predicts erosion for all velocities massively it shows maximum relative error among all. The calculated percentage relative error between most of the erosion models and experimental data varies between 5% to 50%.

Since developed erosion model has the capability to adjust model constants and exponents according to particle velocities, the relative error is expected to be constant for all velocities. The relative error of the erosion rate predicted by the proposed erosion model varied between 4% to 40% for most velocities. Erosion model constants for Oka's and Neilson's erosion model were obtained from the experimental data set at the particle velocity of 17.23 m/s . The erosion rate predicted by these two erosion models should have been under-predicted for higher velocity if the erosion model constants and exponents are dependent on velocity. Figure 6.16 shows that Oka's erosion model exhibits a similar trend in relative error (between 20% to 42%) for a higher particle velocity. For Neilson's erosion model decrease in relative error is observed with increase in particle velocity.

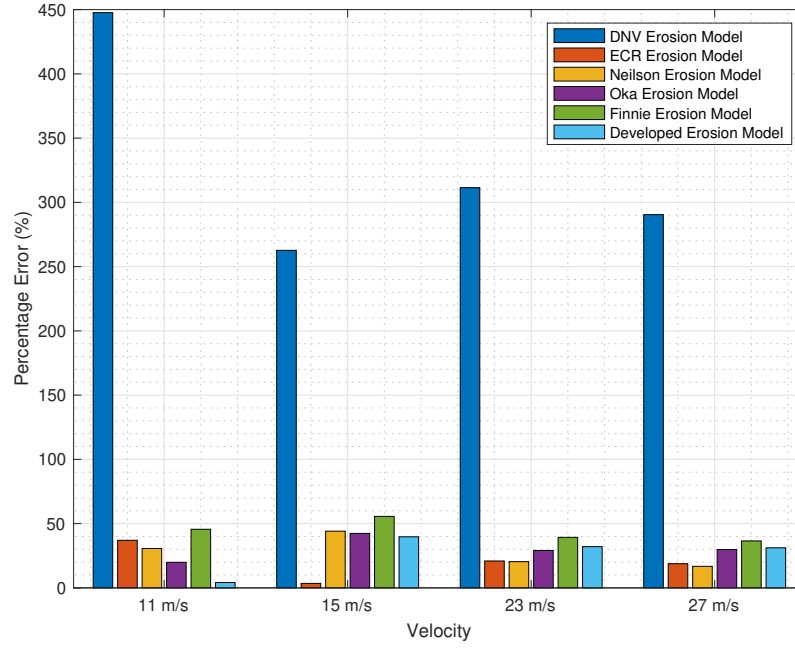


Figure 6.16: Percentage error between predicted erosion and experimental data

To analyse the behaviour of erosion models particle information such as average particle impact velocity and impact angle on the elbow surface is shown in contour plot (figure 6.17a and 6.17b) for the test case with particle velocity of 15m/s . Figure 6.17a shows as particles enter the domain with 15m/s it gains momentum from the surrounding fluid and attains maximum average impact velocity of around 26m/s . Most of the impacts with maximum impact velocity are observed in the downstream part of the elbow. This behaviour because, as particle impacts downstream part of the elbow; it will lose energy which will decrease particle velocity for further impact. Figure 6.17b shows the average particle impact angles on the elbow surface. It can be noted that the average particle impact angle on the elbow surface varies between 0° to 50° .

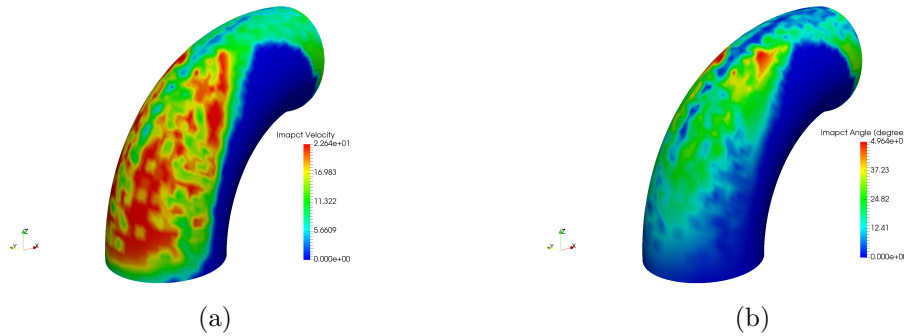


Figure 6.17: Particle information predicted by the CFD based erosion solver in 90° elbow at inlet velocity of 15m/s , a) average particle impact velocity, b) average particle impact angle

Erosion model constants and exponents used for Oka's and Neilson's erosion model are obtained at a particle velocity of $17m/s$. For a dry impact test case, these model constants are kept constant, and erosion rate is predicted at all impact angle at a velocity of $25.22m/s$ and $32.56m/s$. As model constants are derived at $17m/s$, for higher velocities it is expected for these erosion models to over or under predict erosion rate if the erosion model constants are velocity dependent. For the dry impact test case at particle velocity of $25.22m/s$ and $32.56m/s$, the erosion rate is predicted by the erosion models using constants derived at $17m/s$.

Figure 6.18a and 6.18b show as particle velocity is increased, Neilson's erosion model under predicts erosion. Figure 6.15 shows, erosion rate predicted by Neilson's erosion model is similar to that predicted by Oka's and proposed erosion model. As velocity increase, Neilson's erosion model under predicts erosion rate; hence relative error decreases for Neilson's erosion model in figure 6.16.

Figure 6.18a and 6.18b show Oka's erosion model under predicts erosion rate for higher particle velocities. This is expected as Oka's erosion models constants are obtained at $17m/s$. Oka's erosion model under predicts erosion at higher impact angle. For low impact angle (up to 45°) erosion rate predicted by Oka's erosion model is in good agreement with experimental data. However, for elbow test cases, as seen in figure 6.17b, average impact angle on the elbow surface varies between 0° to 50° . This is the reason why the relative error in figure 6.16 for Oka's model did not change much with an increase in velocity.

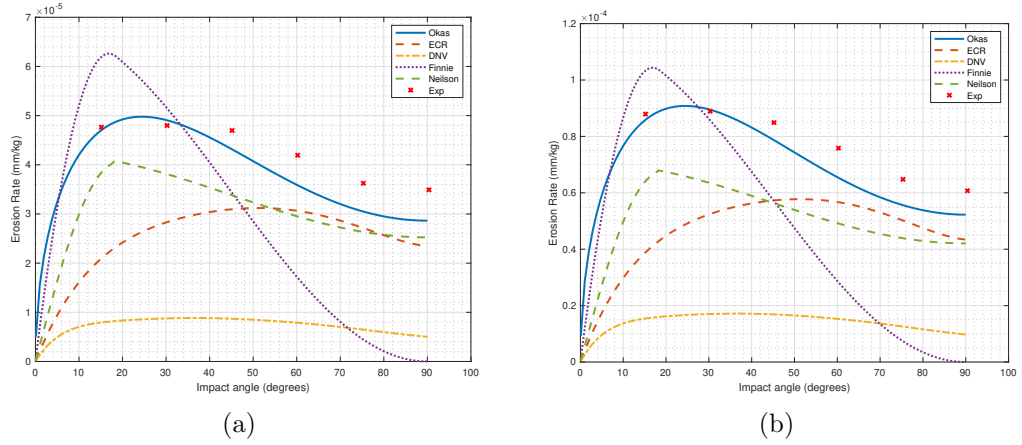


Figure 6.18: Erosion rate predicted vs particle impact angle, a) at particle inlet velocity of $25.22m/s$, b) at particle inlet velocity of $32.56m/s$

6.2.9 Particle Feed Rate

To study capability of erosion model under different particle feed rate, test case with feed rate of 192kg/day and 452kg/day at 15m/s are simulated. Particle size used in simulation is $300\mu\text{m}$. Erosion rate predicted by developed erosion model and the CFD based erosion solver is as shown in contour plots (figure 6.19a and 6.19b).

Figure 6.19a and 6.19b shows for same particle velocity of 15m/s but changing particle feed rate shows no change in the shape of erosion scar. The magnitude of erosion rate predicted at particle feed rate 452kg/day is slightly lower than that predicted feed rate 192kg/day as shown in table 6.6.

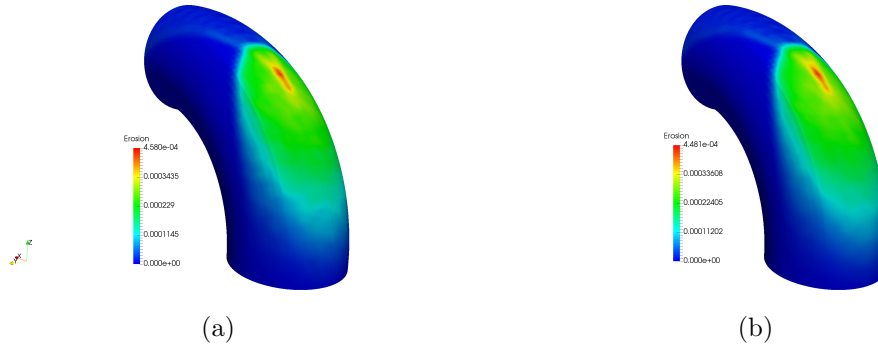


Figure 6.19: Erosion rate predicted by the CFD based erosion solver in 90° elbow at inlet velocity of 15m/s , a) using feed rate of 192 kg/day , b) using feed rate of 452 kg/day

Table 6.6: Maximum erosion rate predicted by the developed erosion model for different particle feed rates using particle of $300\mu\text{m}$ size

V_{air} (m/s)	Feed rate (kg/day)	CFD data (mm/kg)	Exp. data (mm/kg)	Error (%)
15	192	4.58E -04	2.76E -04	39.73
15	452	4.48E -04	3.55E -04	26.19

An increasing feed rate of the particles undoubtedly changes the frequency of impact of particles on the target surface. As discussed in section 5.2 impacting particle on the target surface may change target surface material properties. This change in the target material properties depends on many parameters such as particle velocity, material etc. Among such parameters, the particle feed rate is one of them. To accommodate the effect of change in particle feed rate on the erosion (i.e last term in equation 5.12) is essential. In section 6.1, when constants and developed erosion are derived from experimental data, available experimental data was at constant particle feed rate. Hence in the current test case, the second term from equation 5.12 is associated with the particle feed rate is neglected.

Increasing feed rate changed the magnitude of erosion rate predicted in the

current test case slightly. However, the second term in equation 5.12 is associated with particle feed rate is essential as in order to accommodate the effect of feed rate while predicting erosion rate.

6.2.10 Particle Size

To analyse effect of the particle size on erosion rate prediction two different particle size 300 μm and 150 μm were simulated at particle velocity of 15m/s. Erosion rate predicted by the developed erosion model and erosion scar for 300 μm and 150 μm particle size are depicted in figure 6.20a and 6.20b. Table 6.7 shows erosion rate predicted by different particle size indicates erosion rate predicted by the smaller particle is bigger than that predicted by, the larger particles. Smaller particles contain small kinetic energy compared to larger particles at the same velocity. The magnitude of erosion rate predicted by the smaller particles (150 μm) should have been smaller than that of larger particles because of low kinetic energy. Maybe because as smaller particles are tightly coupled with surrounding fluid due to low Stokes number, smaller particles follow with the fluid flow more tightly than larger particles. Figure 6.20a and 6.20b shows erosion scar for different particle size is different. Smaller particle tends to impact more on the upstream part of elbow than downstream. This may have created more number of particle impact near erosion hot spot region on elbow subsequently over predicting erosion rate.

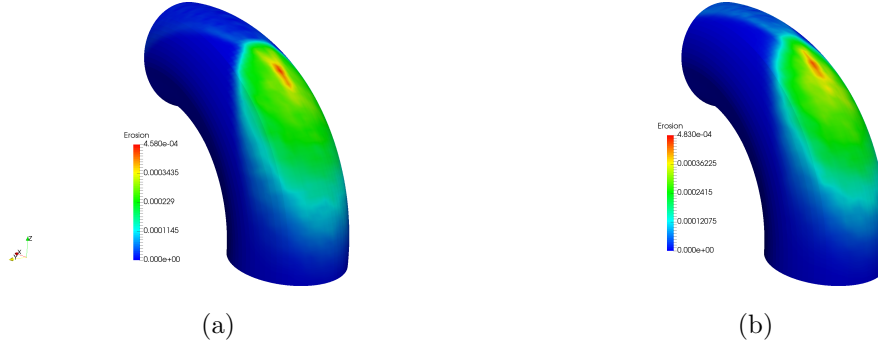


Figure 6.20: Erosion rate predicted by the CFD based erosion solver in 90° elbow at inlet velocity of 15m/s, a) using particle size of 300 μm , b) using particle size of 150 μm

Table 6.7: Maximum erosion rate predicted by the developed erosion model for different particle size

V_{air} (m/s)	Feed rate (kg/day)	Particle size μm	CFD data (mm/kg)	Exp. data (mm/kg)	Error (%)
15	192	300	4.58E -04	2.76E -04	39.73
15	237	150	4.83E -04	1.53E -04	215

Also compare to the particle with the larger size, the smaller particle has less

contact area on the target surface. Developed erosion model does not take the size of the particle into account explicitly. Moreover, constants and exponents required for the developed erosion model is derived from experimental data where the particle size used was $300\mu\text{m}$. Additionally, the second term in equation 5.12 associated with particle feed rate is neglected here. This may be another source of error because of which developed erosion model over predicts erosion for smaller size particles.

6.2.11 Elbow Orientation

To study the capability of the CFD based erosion solver for different orientation elbow test case is simulated for vertical horizontal and horizontal-horizontal orientations. Simulation parameters for both test case are kept same at particle velocity of 15m/s , but the direction of the gravitational force is changed.

Figure 6.21a shows erosion rate predicted by vertical-horizontal (V-H) configuration and figure 6.21b shows erosion rate predicted in horizontal-horizontal (H-H) elbow configuration. It is to be noted that in V-H configuration gravitational force is acting along the negative Z-axis and in H-H configuration gravitational force is acting along the negative Y-axis. Figure 6.21a and 6.21b depicts that for $300\mu\text{m}$ the erosion rate predicted at the different configuration of the elbow is completely different in terms of scar shape and magnitude of the erosion rate. Erosion hot spot in horizontal configuration moved from the centerline on extrados of the elbow towards the side of the elbow. It is interesting to note that the erosion rate predicted in (H-H) configuration is half the magnitude of erosion rate in (V-H) configuration for the same flow conditions. Similar observations were also reported by Parsi et al. [44] from the experimental study of erosion in slurry flow with (V-H) and (H-H) orientation of the elbow. They reported the magnitude of erosion rate in (V-H) configuration was of order higher than (H-H) configuration of the elbow. Parsi et al. [44] has attributed the reason behind the difference in erosion rate in different elbow orientation towards the size of liquid film formation on the elbow wall and the dry out phenomenon on the elbow wall. However, in the current test case, as air is the fluid medium, we can not claim that difference in erosion rate is due to liquid film thickness on the elbow wall. Particles in V-H configurations are uniformly distributed than in H-H configuration of the elbow. Moreover, impacting particles in V-H configuration are concentrated near the erosion hot spot area. While in H-H configuration particle impacts are distributed on the sidewall of the elbow as seen from erosion scar shape in figure 6.21b. This may be the reason that predicted erosion rate in H-H configuration is found much lower than that is predicted by V-H configuration.

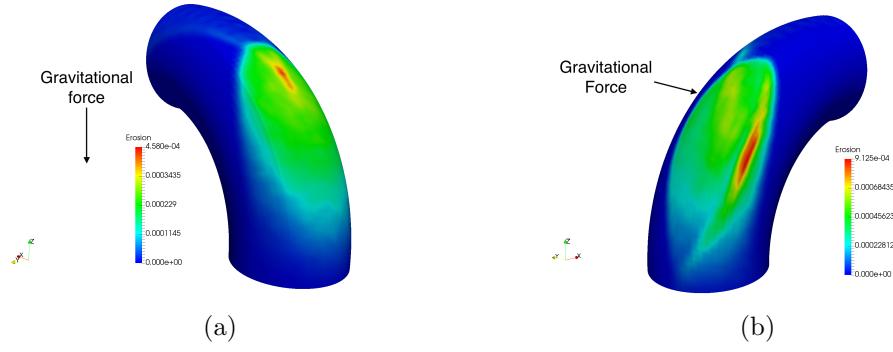


Figure 6.21: Erosion rate predicted by the CFD based erosion solver in 90° elbow at inlet velocity of 15m/s , a) using V-H configuration of elbow, b) using H-H configuration of elbow

6.3 Summary

In this chapter, the developed erosion model and the CFD based erosion solver have been analysed for the application test case. For the application test, erosion in 90° elbow of SS316 steel is analysed, and results are compared with the experimental data reported by Vieira et al. [112]. In the first part of this chapter, a detailed procedure to extract erosion models constants and exponents from experimental data of dry impact test is explained. Later, using extracted erosion models constants and exponents erosion in 90° elbow is analysed. A number of different test cases have been simulated for 90° elbow to analyse the effect of different particle sizes, feed rates, orientations, rebound models and size distribution models on the erosion rate. The erosion rate in 90° elbow is analysed for varying particle velocities, and the predicted erosion rate by the developed erosion model is compared with the experimental data [112] and other implemented erosion models. It is observed from the simulation results that the developed erosion model and solver predicts the erosion rate in good agreement with the experimental data. While analysing 90° elbow test cases, advantages and limitation of the developed erosion model as well as other implemented erosion models from the literature [13, 16–20] are critically investigated.

Chapter 7

Conclusion and Future Work

Erosion wear of the mechanical equipment due to solid particles is a common problem faced by many industries, including the oil and gas industry. The accurate prediction of erosion rate in such equipment will help engineers and designers locate erosion susceptible regions and to optimise the design of the equipment to reduce the erosion damage. Many different mathematical formulations are proposed by researchers to predict erosion. Some of these mathematical formulations are used along with CFD to predict erosion damage in complex geometries. This chapter presents the summary and conclusion of the present study. Recommendations for future work is also described in this chapter.

7.1 Summary

CFD is a powerful tool which can simulate fluid field and track particles in complex geometries and predict erosion rate accurately. CFD based erosion modelling consists of two main steps, modelling of solid particle and fluid (two-phase) flows and predicting the erosion using erosion models. A new CFD based erosion solver is constructed using a set of open-source C++ libraries called OpenFOAM.

In order to predict erosion accurately using CFD based erosion solver, it is essential for the solver to model fluid field and track particles accurately. To validated particle information predicted by the constructed CFD based erosion solver, dry impact test case and slurry impact test case are simulated. Particle information predicted by the CFD based erosion solver in the slurry and dry impact test near the target wall agrees well with the experimental data. It is demonstrated from the CFD analysis of dry and slurry impact tests that the constructed CFD based erosion solver is capable of predicting accurate particle information near the target wall.

To analyse the constructed CFD based erosion solver, dry impact test case on AISI 1018 target material is simulated by implementing a few widely used erosion models. While analysing erosion rate prediction at different impact velocities and

impacting angles for AISI 1018 test case, few limitations in implemented erosion models were observed. These observed limitations were verified by simulating dry impact test case for API X70 and API X100 steel as a target material. In order to explore the observed limitation in the implemented erosion models, a parametric study of experimental data from literature is carried out. In a parametric study, detailed analysis is executed for the mechanical properties of the target materials, and erosion rate predicted by the erosion models at different particle velocities and impacting angles. Based on this analysis, a new erosion model is proposed, which is capable of predicting erosion at a wide range of impacting velocities and impacting angles and at various feed rates. Newly proposed erosion model and other implemented erosion models in the erosion solver are then validated against three dry impact test cases of AISI 1018, API X70 and API X100 steel as a target material.

Further, 90° elbow of SS 316 material is deliberated using the constructed CFD based erosion solver and erosion rate predicted is compared with experimental data. The effect of different particle velocities, sizes, feed rates, orientations, rebound models and size distribution models on the erosion rate is also investigated. The predicted erosion rate by the developed erosion model is compared with the experimental data. The erosion rate predicted by the newly developed erosion model and solver agrees well with experimental data.

7.2 Conclusion

It is found from the CFD analysis that the behaviour of particles in gas-solid and liquid-solid flow is different. In dry (gas-solid) impact test, particles impact the flat target material surface with nearly the same velocity and impact angle at which it exits from the jet. While in the slurry (liquid-solid) impact test, particles impact the flat target material surface with a wide range of impacting angle and the high-velocity ring is observed on the target surface away from the jet core. Due to the high viscosity of water compared to gas, particle relaxation time decreases by order of magnitude in the slurry flow. Hence, due to low Stokes number fluid flow effect dominates particle inertia and its trajectories. This makes particles to follow the fluid flow path and causes curvature in particle trajectories near the target surface. Particles hit the target wall as that of fluid flow in slurry jets with a wide range of impact angles. This is the reason for high-velocity ring away from the jet core. In gas-solid flow due to high Stokes number, particle inertia dominates the flow trajectories, and particles can cross fluid streamlines. Hence, particles impact the target surface in a small circular area of a diameter similar to the nozzle. This is the reason for U shaped scar, which is commonly observed in dry impact erosion tests, while W shaped scar is observed in case of slurry jet impact erosion tests.

In the slurry jet impact case, the particle size distribution function plays a vital role in the accurate prediction of particle impact angle on the target surface. Particles with different size possess different Stokes number. In the analysis of particle size distribution in the slurry impact test, it is observed that using constant particle size predicts impact angle accurately within the jet core, but it underpredicts impact angle away from the jet core. While using particle size distribution function, particles with low Stokes number flow along with fluid streamlines more closely and impacts the target surface with a wide range of impact angles away from the jet core.

In the CFD based erosion solver, few widely used erosion models (Finnie, Neilson, Oka, E/CRC and DNV) have been implemented. These implemented erosion models are validated and analysed with experimental data of dry impact test cases for AISI 1018 steel as a target material. It is found that E/CRC erosion models, consistently overpredicted erosion rate at all the particle impact velocities and impacting angle. DNV erosion model underpredicted erosion rate at low velocities and over predicted erosion rate at high velocities. Finnie's model overpredicted the erosion rate at low impact angles and underpredicted erosion rate at high impact angles at all the particle velocities. Oka's erosion model used with constants and exponents reported by the Oka et al. [19][20] and Neilson's erosion models found to be overpredicting the erosion rate for high particle velocities. Oka's and Neilson's model predicted erosion rate in good agreement with the experimental data for particle velocity of 36 m/s . This is because the constants k_2 and exponents n_1 and n_2 for Oka's model and the cutting and deformation energy for the Neilson's erosion model are obtained from the experimental data at particle velocity of 36 m/s . For particle velocity higher than 36 m/s Oka's and Neilson's erosion models overpredicts the erosion rate. To confirm these observed limitations, a dry impact test case on API X70 and API X100 steel is analysed. The erosion rate predicted by these models exhibited a similar trend of limitations. It was found that the deformation and cutting wear required for the Neilson's erosion model changes with change in particle velocity. Similarly, for Oka's erosion model, constant and exponent are given in terms of the material hardness and particle properties (such as size and shape). In the test cases AISI 1018, API X70 and API X100 target materials are changed, but the erodent particles used in all the test cases are of the same material, shape and size. It is also found that the particle velocity influences Oka's model constants and exponents.

In order to analyse the effect of particle impact velocity, impact angle and target material properties on the erosion rate, a parametric study is carried out based on the experimental data reported by Islam et al. [23][10, 22, 24]. Experimental data is available for AISI 1018, AISI 1080, API X70 and API X100 pipeline steel at four different particle velocities and four different impacting angles. From parametric analysis, it is observed that material properties such as

hardness and ductility both play an important role in resisting erosion wear. The relationship of erosion rate at different impacting angles is found to be non-linear with the particle impacting velocities. The reason for the non-linear relationship with velocity is attributed to the change in mechanical properties of the target material due to work hardening by particle impact. Few researchers have tried to accommodate work hardening effect in their proposed erosion models by using plastic zone size. Estimating plastic zone size is a challenging task by measuring erosion scar and microhardness tests on the eroded materials. This makes it complicated to use these erosion models in practical application cases. In order to accommodate and model the non-linear relationship of erosion rate at different impacting angles at different velocities, a new erosion model is proposed in this study.

The new proposed erosion model takes a number of particle and target material properties into account. The wear energy factor and exponents required for the new proposed erosion model are obtained from the experimental data. The new proposed erosion model adjusts models constant and exponent dynamically according to the particle velocity, and hence it accommodates the non-linear relationship of erosion rate with particle velocities. The new erosion model is validated with experimental data for AISI 1018, API X70 and API X100 materials and is found to be in better agreement compare to other implemented erosion models.

The proposed erosion model is analysed on an application test case, by simulating 90° SS316 elbow. The predicted erosion rate in the application test case is validated with the experimental data reported by Vieira et al. [112]. The erosion rate predicted by the proposed erosion model is found to be in good agreement with the experimental data. It is found for application test case different turbulence models have limited effect on the predicted erosion rate, as detachment in the flow is not expected here. The developed erosion model is analysed on application test case for different particle rebound models, particle size distribution function, particle velocities, particle feed rate, particle size and elbow orientation. In the application test case, it was found that in order to predict accurate erosion rate and physical erosion scar use of rebound model (by Grant and Tabakoff [160]) is essential. As using the standard rebound model predicted non-physical vee-shaped scar on the elbow. It is observed that the size distribution function in the application test case with the gas-solid flow have limited effect on predicted erosion rate. Using Roisn-Rammeler size distribution function changed the shape of erosion hot spot on the elbow, but a small change in erosion magnitude is observed.

The application test case is also analysed for the erosion rate predicted by the different erosion models implemented in the CFD based erosion solver for different particle velocities. It is found that the new proposed erosion model overpredicts

erosion rate within margin of 4% to 40% of the experimental data. DNV erosion model consistently underpredicts erosion rate at all particle velocities with an order of 2.5 to 4.5 times the experimental data. Other erosion models such as E/CRC, Finnie's, Neilson's and Oka's found to be overpredicting the erosion rate within range of 5% to 50% of the experimental data.

The proposed erosion model is analysed for its capability to predict the erosion rates with changing particle feed rate in the application test case. As constants and exponents for the proposed erosion model are obtained from the experimental data where feed rate was constant, not a significant difference in predicted erosion rate is found with different particle feed rate. While analysing erosion rate predicted by the CFD based erosion solver in the different orientation of elbow, it was found that the magnitude of erosion rate predicted in the vertical-horizontal configuration of the elbow was of order higher than that predicted in the horizontal-horizontal configuration of the elbow.

7.3 Future Work and Recommendations

In the proposed erosion model wear energy factor, constants and the exponents are obtained from the experimental data. Having more experimental data for a similar test case with different target material will help to express these constants and exponents in terms of material and particle properties as well.

In order to analyse the accuracy of the proposed erosion model, it can be applied to industrial applications cases where significant variations of particle impact velocities and impacting angle are expected. It is recommended to use the proposed erosion model to analyse choke valve geometry which is usually more vulnerable for erosion damage.

While developing new erosion model, experimental data used for analysis was available for different target materials, but particle material, shape and size used in all experimental data were the same. In order to add the effect of particle size and shape in the proposed erosion model, it is recommended to carry more experimental tests with different particle size, shape and material.

In constructed CFD based erosion solver, it assumed that due to erosion target wall surface does not get modified. Hence, the effect of the eroded wall on fluid flow properties and particle behaviour is not considered here. This assumption of unchanged target surface profile may be a possible source of error in predicting erosion. It is recommended in future to carry erosion analysis with considering the surface profile of eroded material.

In the proposed erosion model effect of particles feed rate is considered based on experimental data, but inter-particle interaction is not considered. Investigation

of inter-particle interaction to analyse its effect on the erosion rate can be the future prospect of this work.

Proposed erosion model is derived from experimental data from literature of dry impact tests. It will be interesting to explore the capability of the proposed erosion model and solver for slurry flows and can be done in future.

Bibliography

- [1] Mazdak Parsi, Kamyar Najmi, Fardis Najafifard, Shokrollah Hassani, Brenton S McLaury, and Siamack A Shirazi. A comprehensive review of solid particle erosion modeling for oil and gas wells and pipelines applications. *Journal of Natural Gas Science and Engineering*, 21:850–873, 2014.
- [2] Toshiya Oshita, Shoji Hirokawa, A Aziz Y Rammah, et al. Integrated approach for sand management: Field application to an offshore oil field. In *Middle East Oil Show and Conference*. Society of Petroleum Engineers, 1997.
- [3] Z Mazur, R Campos-Amezcu, G Urquiza-Beltran, and A Garcia-Gutierrez. Numerical 3d simulation of the erosion due to solid particle impact in the main stop valve of a steam turbine. *Applied Thermal Engineering*, 24(13): 1877–1891, 2004.
- [4] Guomei Li, Yueshe Wang, Renyang He, Xuewen Cao, Changzhi Lin, and Tao Meng. Numerical simulation of predicting and reducing solid particle erosion of solid-liquid two-phase flow in a choke. *Petroleum Science*, 6(1): 91–97, 2009.
- [5] JS Mason and BV Smith. The erosion of bends by pneumatically conveyed suspensions of abrasive particles. *Powder Technology*, 6(6):323–335, 1972.
- [6] Xianghui Chen, Brenton S McLaury, and Siamack A Shirazi. Numerical and experimental investigation of the relative erosion severity between plugged tees and elbows in dilute gas/solid two-phase flow. *Wear*, 261(7-8):715–729, 2006.
- [7] Amir Mansouri. *A combined CFD-experimental method for developing an erosion equation for both gas-sand and liquid-sand flows*. The University of Tulsa, 2016.
- [8] H N Raghavendra, M Shivashankar, and Prem Anand Ramalingam. Simulation of Erosion Wear in Choke Valves using CFD. *International Journal of Engineering Research & Technology*, 3(7):52–56, 2014. doi: July-2014.

- [9] U Ekpemu, S Aloba, et al. Pipeline laser imaging and metrology using laser smart pig. In *Nigeria Annual International Conference and Exhibition*. Society of Petroleum Engineers, 2010.
- [10] Md Aminul Islam and Zoheir N. Farhat. Effect of impact angle and velocity on erosion of API X42 pipeline steel under high abrasive feed rate. *Wear*, 311(1-2):180–190, 2014. ISSN 00431648.
- [11] Fazlollah Madani Sani, Srdjan Nesic, Khlefa Esaklul, Sytze Huizinga, and Sytze Corrosion Consultancy. Review of the api rp 14e erosional velocity equation: Origin, applications, misuses and limitations. 2019.
- [12] RP API. 14e: Recommended practice for design and installation of offshore production platform piping systems. *API, Washington DC*, 1991.
- [13] I Finnie. The mechanism of erosion of ductile materials. In *Proc. of the Third US National Congress of Applied Mechanics, Hagthornthwaite, RM, Ed., ASME, New York*, page 7082, 1958.
- [14] JGA Bitter. A study of erosion phenomena part i. *wear*, 6(1):5–21, 1963.
- [15] JGA Bitter. A study of erosion phenomena: Part ii. *Wear*, 6(3):169–190, 1963.
- [16] JH Neilson and A Gilchrist. Erosion by a stream of solid particles. *wear*, 11(2):111–122, 1968.
- [17] Y Zhang, EP Reuterfors, B Sf McLaury, SA Shirazi, and EF Rybicki. Comparison of computed and measured particle velocities and erosion in water and air flows. *Wear*, 263(1-6):330–338, 2007.
- [18] K Haugen, O Kvernfold, A Ronold, and R. Sandberg. Sand erosion of wear-resistant materials: Erosion in choke valves. *Wear*, 186:179–188, 1995.
- [19] Y Isomoto Oka, K Okamura, and T Yoshida. Practical estimation of erosion damage caused by solid particle impact: Part 1: Effects of impact parameters on a predictive equation. *Wear*, 259(1-6):95–101, 2005.
- [20] YI Oka and T Yoshida. Practical estimation of erosion damage caused by solid particle impact: Part 2: Mechanical properties of materials directly associated with erosion damage. *Wear*, 259(1-6):102–109, 2005.
- [21] G Sundararajan. The solid particle erosion of metallic materials: the rationalization of the influence of material variables. *Wear*, 186:129–144, 1995.

- [22] Md Aminul Islam, Tahrim Alam, Zoheir N. Farhat, Adel Mohamed, and Akram Alfantazi. Effect of microstructure on the erosion behavior of carbon steel. *Wear*, 332-333:1080–1089, 2015. ISSN 00431648.
- [23] Md Islam et al. Erosion, corrosion and erosion-corrosion of oil and gas pipeline steels. 2015.
- [24] Md Aminul Islam, Tahrim Alam, and Zoheir Farhat. Construction of erosion mechanism maps for pipeline steels. *Tribology International*, 102:161–173, 2016.
- [25] VB Nguyen, QB Nguyen, YW Zhang, CYH Lim, and BC Khoo. Effect of particle size on erosion characteristics. *Wear*, 348:126–137, 2016.
- [26] Robert Bellman and Alan Levy. Erosion mechanism in ductile metals. *Wear*, 70(LBL-10289), 1981.
- [27] Yu-Fei Wang and Zhen-Guo Yang. Finite element model of erosive wear on ductile and brittle materials. *Wear*, 265(5-6):871–878, 2008.
- [28] P. De. Haller. Erosion and kavitations-erosion. *Handbuch der Werkstoffprüfung*, 2:471–488, 1939.
- [29] K Wellinger. * sandstrahlverschleiss an metallen. *ZEITSCHRIFT FUR METALLKUNDE*, 40(10):361–364, 1949.
- [30] Iain Finnie, GR Stevick, and JR Ridgely. The influence of impingement angle on the erosion of ductile metals by angular abrasive particles. *Wear*, 152(1):91–98, 1992.
- [31] Iain Finnie. Some observations on the erosion of ductile metals. *wear*, 19(1):81–90, 1972.
- [32] GP Tilly. A two stage mechanism of ductile erosion. *Wear*, 23(1):87–96, 1973.
- [33] G Sundararajan and PG Shewmon. A new model for the erosion of metals at normal incidence. *Wear*, 84(2):237–258, 1983.
- [34] Det Norske Veritas. Recommended practice rp o501 erosive wear in piping systems. *DNV Recommended Practice*, 4, 2007.
- [35] Yongli Zhang. *Application and improvement of computational fluid dynamics (CFD) in solid particle erosion modeling*. ProQuest, 2006.
- [36] AG Evans and To R Wilshaw. Quasi-static solid particle damage in brittle solids—i. observations analysis and implications. *Acta Metallurgica*, 24(10): 939–956, 1976.

- [37] H McI Clark and Ryan B Hartwich. A re-examination of the ‘particle size effect’ in slurry erosion. *Wear*, 248(1-2):147–161, 2001.
- [38] Ambrish Misra and Iain Finnie. On the size effect in abrasive and erosive wear. *Wear*, 65(3):359–373, 1981.
- [39] IR Kramer and LJ Demer. The effect of surface removal on the plastic behavior of aluminum single crystals. *TRANSACTIONS OF THE METALLURGICAL SOCIETY OF AIME*, 221(4):780–786, 1961.
- [40] A Abouel-Kasem. Particle size effects on slurry erosion of 5117 steels. *Journal of tribology*, 133(1), 2011.
- [41] Girish R Desale, Bhupendra K Gandhi, and SC Jain. Particle size effects on the slurry erosion of aluminium alloy (aa 6063). *Wear*, 266(11-12):1066–1071, 2009.
- [42] S Malkin, KL Wiggins, M Osman, and RW Smalling. Size effects in abrasive processes. In *Proceedings of the Thirteenth International Machine Tool Design and Research Conference*, pages 291–296. Springer, 1973.
- [43] H Arabnejad, A Mansouri, SA Shirazi, and BS McLaury. Development of mechanistic erosion equation for solid particles. *Wear*, 332:1044–1050, 2015.
- [44] Mazdak Parsi, Ronald E Vieira, Netaji Kesana, Brenton S McLaury, and Siamack A Shirazi. Ultrasonic measurements of sand particle erosion in gas dominant multiphase churn flow in vertical pipes. *Wear*, 328:401–413, 2015.
- [45] Richard Brown, S Kosco, and EJ Jun. The effect of particle shape and size on erosion of aluminum alloy 1100 at 90 impact angles. *Wear*, 88(2):181–193, 1983.
- [46] Joshua Salik and Donald H Buckley. Effects of erodant particle shape and various heat treatments on erosion resistance of plain carbon steel. 1981.
- [47] Alan V Levy and Pauline Chik. The effects of erodent composition and shape on the erosion of steel. *Wear*, 89(2):151–162, 1983.
- [48] Cunkui Huang, P Minev, Jingli Luo, and K Nandakumar. A phenomenological model for erosion of material in a horizontal slurry pipeline flow. *Wear*, 269(3-4):190–196, 2010.
- [49] Shigetaka Wada and Naoyoshi Watanabe. Solid particle erosion of brittle materials (part 3), the interaction with material properties of target and that of impingement on erosive mechanism. *Journal of the Ceramic Association*, 95(1102):573–578, 1987.

- [50] PH Shipway and IM Hutchings. The role of particle properties in the erosion of brittle materials. *Wear*, 193(1):105–113, 1996.
- [51] H Uuemöis and I Kleis. A critical analysis of erosion problems which have been little studied. *Wear*, 31(2):359–371, 1975.
- [52] T Deng, AR Chaudhry, M Patel, I Hutchings, and MSA Bradley. Effect of particle concentration on erosion rate of mild steel bends in a pneumatic conveyor. *Wear*, 258(1-4):480–487, 2005.
- [53] DR Andrews and N Horsfield. Particle collisions in the vicinity of an eroding surface. *Journal of Physics D: Applied Physics*, 16(4):525, 1983.
- [54] R Macchini, MSA Bradley, and T Deng. Influence of particle size, density, particle concentration on bend erosive wear in pneumatic conveyors. *Wear*, 303(1-2):21–29, 2013.
- [55] D Mills and JS Mason. Particle concentration effects in bend erosion. *Powder Technology*, 17(1):37–53, 1977.
- [56] Min-Hua Wang, Cunkui Huang, K Nandakumar, P Minev, J Luo, and S Chiovelli. Computational fluid dynamics modelling and experimental study of erosion in slurry jet flows. *International journal of computational fluid dynamics*, 23(2):155–172, 2009.
- [57] Sylvain Turenne, Michel Fiset, and Jacques Masounave. The effect of sand concentration on the erosion of materials by a slurry jet. *Wear*, 133(1):95–106, 1989.
- [58] Alejandro Lopez. Lpt for erosion modeling in openfoam, 2014.
- [59] JA Laitone. Erosion prediction near a stagnation point resulting from aerodynamically entrained solid particles. *Journal of Aircraft*, 16(12):809–814, 1979.
- [60] JA Laitone. Aerodynamic effects in the erosion process. *Wear*, 56(1):239–246, 1979.
- [61] Iain Finnie. Some reflections on the past and future of erosion. *Wear*, 186:1–10, 1995.
- [62] CE Smeltzer, Mary Ellen Gulden, and WA Compton. Mechanisms of metal removal by impacting dust particles. 1970.
- [63] AJ Burnett, SR De Silva, and Alan R Reed. Comparisons between “sand blast” and “centripetal effect accelerator” type erosion testers. *Wear*, 186:168–178, 1995.

- [64] BA Lindsley and AR Marder. The effect of velocity on the solid particle erosion rate of alloys. *Wear*, 225:510–516, 1999.
- [65] Ian M Hutchings. Ductile-brittle transitions and wear maps for the erosion and abrasion of brittle materials. *Journal of Physics D: Applied Physics*, 25(1A):A212, 1992.
- [66] GL Sheldon and Ashok Kanhere. An investigation of impingement erosion using single particles. *Wear*, 21(1):195–209, 1972.
- [67] Y Isomoto Oka, M Matsumura, and T Kawabata. Relationship between surface hardness and erosion damage caused by solid particle impact. *Wear*, 162:688–695, 1993.
- [68] Alan V Levy. The solid particle erosion behavior of steel as a function of microstructure. *Wear*, 68(3):269–287, 1981.
- [69] L Ambrosini and Shyam Bahadur. Erosion of aisi 4140 steel. *Wear*, 117(1):37–48, 1987.
- [70] T Foley and A Levy. The erosion of heat-treated steels. *Wear*, 91(1):45–64, 1983.
- [71] A Levy and G Hickey. Surface degradation of metals in simulated synthetic fuels plant environments, 1981.
- [72] R Brown and Jeff W Edington. Occurrence of melting during the solid particle erosion of copper. *Wear*, 73(1):193–200, 1981.
- [73] IM Hutchings. Mechanisms of the erosion of metals by solid particles. In *Erosion: prevention and useful applications*. ASTM International, 1979.
- [74] B. F. Levin, K. S. Vecchio, J. N. DuPont, and A. R. Marder. Modeling solid-particle erosion of ductile alloys. *Metallurgical and Materials Transactions A*, 30(7):1763–1774, Jul 1999. ISSN 1543-1940.
- [75] RH Richman and WP McNaughton. Correlation of cavitation erosion behavior with mechanical properties of metals. *Wear*, 140(1):63–82, 1990.
- [76] A Venugopal Reddy and G Sundararajan. Erosion behaviour of ductile materials with a spherical non-friable erodent. *Wear*, 111(3):313–323, 1986.
- [77] BF Levin, JN Dupont, and AR Marder. Solid particle erosion resistance of ductile wrought superalloys and their weld overlay coatings. *Journal of materials science*, 33(8):2153–2163, 1998.

- [78] Julius Oscar Hinze. Turbulent fluid and particle interaction. In *Proceedings of the International Symposium on Two-Phase Systems*, pages 433–452. Elsevier, 1972.
- [79] JAC Humphrey. Fundamentals of fluid motion in erosion by solid particle impact. *International journal of heat and fluid flow*, 11(3):170–195, 1990.
- [80] Hector Mcl Clark. The influence of the flow field in slurry erosion. *Wear*, 152(2):223–240, 1992.
- [81] E Zorgani, H Al-Awadi, W Yan, S Al-Lababid, H Yeung, and CP Fairhurst. Viscosity effects on sand flow regimes and transport velocity in horizontal pipelines. *Experimental Thermal and Fluid Science*, 92:89–96, 2018.
- [82] RA Gore and CT Crowe. Modulation of turbulence by a dispersed phase. 1991.
- [83] S Fokeer, S Kingman, I Lowndes, and A Reynolds. Characterisation of the cross sectional particle concentration distribution in horizontal dilute flow conveying—a review. *Chemical Engineering and Processing: Process Intensification*, 43(6):677–691, 2004.
- [84] Y Ninto and Marcelo Horacio Garcia. Experiments on particle—turbulence interactions in the near-wall region of an open channel flow: implications for sediment transport. *Journal of Fluid Mechanics*, 326:285–319, 1996.
- [85] H McI Clark and LC Burmeister. The influence of the squeeze film on particle impact velocities in erosion. *International journal of impact engineering*, 12(3):415–426, 1992.
- [86] Mamdouh M Salama. An alternative to api 14e erosional velocity limits for sand-laden fluids. *J. Energy Resour. Technol.*, 122(2):71–77, 2000.
- [87] AT Bourgoyne Jr et al. Experimental study of erosion in diverter systems due to sand production. In *SPE/IADC drilling conference*. Society of Petroleum Engineers, 1989.
- [88] MM Salama, ES Venkatesh, et al. Evaluation of api rp 14e erosional velocity limitations for offshore gas wells. In *Offshore Technology Conference*. Offshore Technology Conference, 1983.
- [89] AK Coker. Understand two-phase flow in process piping. *Chemical Engineering Progress;(USA)*, 86(11), 1990.
- [90] F Gipson. ‘petroleum production engineering, pits and pieces. *Manual of Southwest Petroleum Short Course, Texas Tech University, April*, pages 17–20, 1989.

- [91] R Heidersbach et al. Velocity limits for erosion-corrosion. In *Offshore Technology Conference*. Offshore Technology Conference, 1985.
- [92] DM Deffenbaugh and JC Buckingham. A study of the erosional/corrosional velocity criterion for sizing multi-phase flow lines. *Southwest Research Institute Final Report, Project, (04-2433)*, 1989.
- [93] JS Smart. A review of erosion corrosion in oil and gas production. *J. S. Smart, III. CORROSION 90/10, NACE, Houston, TX. Per Copy*, 1990.
- [94] Ernest Rabinowicz. The wear equation for erosion of metals by abrasive particles. In *International Conference on Erosion by Liquid and Solid Impact, 5 th, Cambridge, England*, pages 38–1, 1979.
- [95] SJ Svedeman et al. Criteria for sizing multiphase flowlines for erosive/corrosive service. *SPE Production and Facilities*, 9(01):74–80, 1994.
- [96] Iain Finnie. Erosion of surface by solid particles. *wear*, 3:87–103, 1960.
- [97] MT Benchaita, P Griffith, and E Rabinowicz. Erosion of metallic plate by solid particles entrained in a liquid jet. 1983.
- [98] Brenton Scott McLaury. Predicting solid particle erosion resulting from turbulent fluctuations in oilfield geometries. 1997.
- [99] Xianghui Chen, Brenton S McLaury, and Siamack A Shirazi. Application and experimental validation of a computational fluid dynamics (cfd)-based erosion prediction model in elbows and plugged tees. *Computers & Fluids*, 33(10):1251–1272, 2004.
- [100] Jianrong Wang, Siamack A Shirazi, John R Shadley, and Edmund F Rybicki. Application of flow modeling and particle tracking to predict sand erosion rates in 90 degree elbows. *ASME, NEW YORK, NY,(USA).*, (734), 1996.
- [101] Jianrong Wang and Siamack A Shirazi. A cfd based correlation for erosion factor for long-radius elbows and bends. *J. Energy Resour. Technol.*, 125(1):26–34, 2003.
- [102] Fardis Najafifard. *Predicting near wall particle behavior with application to erosion simulation*. The University of Tulsa, 2014.
- [103] Brenton Scott McLaury. *A model to predict solid particle erosion in oilfield geometries*. PhD thesis, University of Tulsa, 1993.
- [104] A Haider and O Levenspiel. Drag coefficient and terminal velocity of spherical and nonspherical particles. *Powder technology*, 58(1):63–70, 1989.

- [105] MA Habib, R Ben-Mansour, HM Badr, and ME Kabir. Erosion and penetration rates of a pipe protruded in a sudden contraction. *Computers & Fluids*, 37(2):146–160, 2008.
- [106] Xue-Guan Song, Joon-Hong Park, Seung-Gyu Kim, and Young-Chul Park. Performance comparison and erosion prediction of jet pumps by using a numerical method. *Mathematical and Computer Modelling*, 57(1-2):245–253, 2013.
- [107] Mikilkumar B Gandhi, Rupa Vuthaluru, Hari Vuthaluru, David French, and Kalpit Shah. Cfd based prediction of erosion rate in large scale wall-fired boiler. *Applied thermal engineering*, 42:90–100, 2012.
- [108] M Atkinson, EV Stepanov, DP Goulet, SV Sherikar, and J Hunter. High pressure testing sand erosion in 3d flow channels and correlation with cfd. *Wear*, 263(1-6):270–277, 2007.
- [109] YM Ferng. Predicting local distributions of erosion–corrosion wear sites for the piping in the nuclear power plant using cfd models. *Annals of Nuclear Energy*, 35(2):304–313, 2008.
- [110] Christopher B Solnordal, Chong Y Wong, and Joan Boulanger. An experimental and numerical analysis of erosion caused by sand pneumatically conveyed through a standard pipe elbow. *Wear*, 336:43–57, 2015.
- [111] Mohammad Zamani, Sadegh Seddighi, and Hamid Reza Nazif. Erosion of natural gas elbows due to rotating particles in turbulent gas-solid flow. *Journal of Natural Gas Science and Engineering*, 40:91–113, 2017.
- [112] Ronald E Vieira, Amir Mansouri, Brenton S McLaury, and Siamack A Shirazi. Experimental and computational study of erosion in elbows due to sand particles in air flow. *Powder technology*, 288:339–353, 2016.
- [113] Wenshan Peng and Xuewen Cao. Numerical prediction of erosion distributions and solid particle trajectories in elbows for gas–solid flow. *Journal of Natural Gas Science and Engineering*, 30:455–470, 2016.
- [114] MS Wallace, WM Dempster, Thomas Scanlon, J Peters, and S McCulloch. Prediction of impact erosion in valve geometries. *Wear*, 256(9-10):927–936, 2004.
- [115] Behzad Baghapour and Pierre E Sullivan. A cfd study of the influence of turbulence on undercatch of precipitation gauges. *Atmospheric Research*, 197:265–276, 2017.

- [116] Soroor Karimi, Siamack A Shirazi, and Brenton S McLaury. Predicting fine particle erosion utilizing computational fluid dynamics. *Wear*, 376: 1130–1137, 2017.
- [117] Nicholas Jacob Clem, Martin P Coronado, Rustom Mody, et al. Utilizing computational fluid dynamics (cfd) analysis as a design tool in frac packing applications to improve erosion life. In *SPE Annual Technical Conference and Exhibition*. Society of Petroleum Engineers, 2006.
- [118] Hrvoje Jasak, Ar Jemcov, and United Kingdom. Openfoam: A c++ library for complex physics simulations. In *International Workshop on Coupled Methods in Numerical Dynamics, IUC*, pages 1–20, 2007.
- [119] Federico Flores, René Garreaud, and Ricardo C. Muñoz. Cfd simulations of turbulent buoyant atmospheric flows over complex geometry: Solver development in openfoam. *Computers & Fluids*, 82:1 – 13, 2013. ISSN 0045-7930.
- [120] Mamoru Ishii. Thermo-fluid dynamic theory of two-phase flow. *STIA*, 75: 29657, 1975.
- [121] Wikiwand. Two-phase flow, 2020. URL https://www.wikiwand.com/en/Two-phase_flow.
- [122] Thomas Nierhaus and Wolfgang Schröder. *Modeling and simulation of dispersed two-phase flow transport phenomena in electrochemical process*. Techn. Hochsch.-Bibl., 2009.
- [123] Ridwan Setiadi Oey. Gas-liquid flows in a two-fluid formalism: Modelling and validation of closure relations. 2005.
- [124] BE Lee, JY Tu, and CAJ Fletcher. On numerical modeling of particle–wall impaction in relation to erosion prediction: Eulerian versus lagrangian method. *Wear*, 252(3-4):179–188, 2002.
- [125] Kyle D Squires and John K Eaton. Particle response and turbulence modification in isotropic turbulence. *Physics of Fluids A: Fluid Dynamics*, 2(7):1191–1203, 1990.
- [126] JAM Kuipers. Multilevel modelling of dispersed multiphase flows. *Oil & gas science and technology*, 55(4):427–435, 2000.
- [127] Said Elghobashi. On predicting particle-laden turbulent flows. *Applied scientific research*, 52(4):309–329, 1994.

- [128] Martin Sommerfeld. *Modellierung und numerische Berechnung von Partikel-beladenen: turbulenten Strömungen mit Hilfe des Euler/Lagrange-Verfah.* Shaker, 1996.
- [129] Mohammadhadi Nakhaei, Bona Lu, Yujie Tian, Wei Wang, Kim Dam-Johansen, and Hao Wu. Cfd modeling of gas–solid cyclone separators at ambient and elevated temperatures. *Processes*, 8(2):228, 2020.
- [130] G Hetsroni. Particles-turbulence interaction. *International Journal of Multiphase Flow*, 15(5):735–746, 1989.
- [131] RA Gore and Clayton T Crowe. Effect of particle size on modulating turbulent intensity. *International Journal of Multiphase Flow*, 15(2):279–285, 1989.
- [132] S Elghobashi. Particle-laden turbulent flows: direct simulation and closure models. In *Computational Fluid Dynamics for the Petrochemical Process Industry*, pages 91–104. Springer, 1991.
- [133] Shinichi Yuu, Naoto Yasukouchi, Yasuo Hirosawa, and Tomosada Jotaki. Particle turbulent diffusion in a dust laden round jet. *AIChE Journal*, 24(3):509–519, 1978.
- [134] John K Dukowicz. A particle-fluid numerical model for liquid sprays. *Journal of computational Physics*, 35(2):229–253, 1980.
- [135] FC Lockwood, AP Salooja, and SA Syed. A prediction method for coal-fired furnaces. *Combustion and Flame*, 38:1–15, 1980.
- [136] AD Gosman and E Ioannides. Aspect of computer simulation of liquid fuelled combustion. In *AIAA 19th aerospace science meeting*, pages 81–0323. McGraw Hill St Louis, 1981.
- [137] Inc Ansys. Ansys fluent theory guide. *vol*, 15317:514, 2011.
- [138] Fangqing Liu. A thorough description of how wall functions are implemented in openfoam. *Proceedings of CFD with OpenSource Software*, pages 1–33, 2016.
- [139] Jun Zhang, Brenton S McLaury, and Siamack A Shirazi. Application and experimental validation of a cfd based erosion prediction procedure for jet impingement geometry. *Wear*, 394:11–19, 2018.
- [140] Amir Mansouri, Hadi Arabnejad Khanouki, Siamack A Shirazi, and Brenton S McLaury. Particle tracking velocimetry (ptv) measurement of abrasive microparticle impact speed and angle in both air-sand and slurry erosion testers. In *ASME 2016 Fluids Engineering Division Summer Meeting*

collocated with the ASME 2016 Heat Transfer Summer Conference and the ASME 2016 14th International Conference on Nanochannels, Microchannels, and Minichannels. American Society of Mechanical Engineers Digital Collection, 2016.

- [141] A Mansouri, H Arabnejad, SA Shirazi, and BS McLaury. A combined cfd/experimental methodology for erosion prediction. *Wear*, 332:1090–1097, 2015.
- [142] Gary H Ganser. A rational approach to drag prediction of spherical and nonspherical particles. *Powder technology*, 77(2):143–152, 1993.
- [143] Andreas Hölzer and Martin Sommerfeld. New simple correlation formula for the drag coefficient of non-spherical particles. *Powder Technology*, 184(3):361–365, 2008.
- [144] Gholamhossein Bagheri and Costanza Bonadonna. On the drag of freely falling non-spherical particles. *Powder Technology*, 301:526–544, 2016.
- [145] M Kandula and D Wilcox. An examination of k-omega turbulence model for boundary layers, free shear layers and separated flows. In *Fluid Dynamics Conference*, page 2317, 1995.
- [146] Carlos Antonio Ribeiro Duarte, Francisco José de Souza, and Vinicius Fagundes dos Santos. Numerical investigation of mass loading effects on elbow erosion. *Powder Technology*, 283:593–606, 2015.
- [147] Carlos Antonio Ribeiro Duarte, Francisco José de Souza, and Vinicius Fagundes dos Santos. Mitigating elbow erosion with a vortex chamber. *Powder Technology*, 288:6–25, 2016.
- [148] V. Hadavi, N.H. Arani, and M. Papini. Numerical and experimental investigations of particle embedment during the incubation period in the solid particle erosion of ductile materials. *Tribology International*, 129:38 – 45, 2019. ISSN 0301-679X.
- [149] H. Arabnejad, A. Mansouri, S.A. Shirazi, and B.S. McLaury. Development of mechanistic erosion equation for solid particles. *Wear*, 332-333:1044 – 1050, 2015. ISSN 0043-1648. 20th International Conference on Wear of Materials.
- [150] Peter Smith. Chapter 3 - metallic materials for piping components. In Peter Smith, editor, *The Fundamentals of Piping Design*, pages 115 – 136. Gulf Publishing Company, 2007. ISBN 978-1-933762-04-3.

- [151] Steven E. Hughes. Chapter 4 - materials and their weldability. In Steven E. Hughes, editor, *A Quick Guide to Welding and Weld Inspection*, Woodhead Publishing Series in Welding and Other Joining Technologies, pages 36 – 48. Woodhead Publishing, 2009. ISBN 978-1-84569-641-2.
- [152] JOHN CASE, LORD CHILVER, and CARL T.F. ROSS. 1 - tension and compression: direct stresses. In JOHN CASE, LORD CHILVER, and CARL T.F. ROSS, editors, *Strength of Materials and Structures (Fourth Edition)*, pages 12 – 54. Butterworth-Heinemann, London, fourth edition edition, 1999. ISBN 978-0-340-71920-6.
- [153] KC Goretta, RC Arroyo, C-T Wu, and JL Routbort. Erosion of work-hardened copper, nickel, and 304 stainless steel. *Wear*, 147(1):145–154, 1991.
- [154] Graham Weir and Stephen Tallon. The coefficient of restitution for normal incident, low velocity particle impacts. *Chemical Engineering Science*, 60(13):3637 – 3647, 2005. ISSN 0009-2509.
- [155] K. L. Johnson. *Contact Mechanics*. Cambridge University Press, 1985. doi: 10.1017/CBO9781139171731.
- [156] M Divakar, VK Agarwal, and SN Singh. Effect of the material surface hardness on the erosion of aisi316. *Wear*, 259(1-6):110–117, 2005.
- [157] Paul C Okonkwo, AMA Mohamed, and Essam Ahmed. Influence of particle velocities and impact angles on the erosion mechanisms of aisi 1018 steel. *Adv Mater Lett*, 6:653–659, 2015.
- [158] J. Malik, I. H. Toor, W. H. Ahmed, Z. M. Gasem, M. A. Habib, R. Ben-Mansour, and H. M. Badr. Evaluating the effect of hardness on erosion characteristics of aluminum and steels. *Journal of Materials Engineering and Performance*, 23(6):2274–2282, 2014. ISSN 15441024.
- [159] Gianluca De Santis, Peter Mortier, Matthieu De Beule, Patrick Segers, Pascal Verdonck, and Benedict Verhegghe. Patient-specific computational fluid dynamics: structured mesh generation from coronary angiography. *Medical & biological engineering & computing*, 48(4):371–380, 2010.
- [160] G Grant and Widen Tabakoff. Erosion prediction in turbomachinery resulting from environmental solid particles. *Journal of Aircraft*, 12(5):471–478, 1975.